COMPUTATIONAL STUDIES OF STRUCTURE AND SURFACE REACTIVITY IN METAL NANOCLUSTERS

by

Michael James Hartmann

B.S., University of Maryland, 2012

Submitted to the Graduate Faculty of

The Kenneth P. Dietrich School of Arts and Sciences in partial fulfillment

of the requirements for the degree of

Doctor of Philosophy

University of Pittsburgh

2018

UNIVERSITY OF PITTSBURGH

DIETRICH SCHOOL OF ARTS AND SCIENCES

This thesis/dissertation was presented

by

Michael J. Hartmann

It was defended on

November 15, 2018

and approved by

Dr. Kenneth D. Jordan, Professor, Department of Chemistry

Dr. Geoffrey R. Hutchison, Associate Professor, Department of Chemistry

Dr. Giannis Mpourmpakis, Assistant Professor, Department of Chemical Engineering

Dissertation Advisor: Dr. Jill E. Millstone, Associate Professor, Department of Chemistry

Dissertation Advisor: Dr. Daniel S. Lambrecht, Assistant Professor, Department of Chemistry

Computational Studies of Structure and Surface Reactivity in Metal Nanoclusters

Michael J. Hartmann, PhD

University of Pittsburgh, 2018

Metal nanoparticles exhibit physical and chemical properties unique to their length scale that have the potential to shape next generation technologies. The large structural and chemical space that determines nanoparticle properties requires feedback between computational and experimental studies to drive the discovery of both new architectures and target properties of these systems. This dissertation describes the application and development of theoretical methods to study metal nanoparticle electronic structure, developing new structure-property relationships and new concepts that govern nanoparticle behavior while connecting theoretical insight with laboratory observations.

In Chapter 1, the dissertation is introduced by detailing how the connection between geometry and electronic structure has shaped the way we teach and understand chemistry across length scale, and projects these concepts onto the 1-3 nm length scale where traditional descriptors of electronic structure break down. In Chapter 2, the optoelectronic impact of alloying Cu with a Au nanocluster is studied, revealing how atomic descriptors and position of the heteroatom determine optical absorption in $[Au_{25}(SR)_{18}]^-$, providing an easily accessible experimental readout of electronic structure. Building on hypotheses tested in Chapter 2, Chapter 3 explores the size dependence of Cu/Au alloying. Here, the atom concentration and composition architecture are key parameters predicted to drive the emergence of plasmonic behavior in $Au_{144-x}Cu_x(SR)_{60}$ nanocluster.

In addition to the composition dependence of nanoparticle properties, the surface chemistry is known to dominate overall nanocluster electronic structure. In Chapter 4, both the type and specific molecular descriptors of the ligand were shown to impact the total magnetic moment of Co_{13} and Co_{55} model nanoclusters. Chapter 5 extends these concepts of surface chemistry to address the size dependent evolution of the ligand mediated magnetic properties in Co_N nanoclusters, demonstrating how energy level alignment and orbital symmetry contribute to size dependent trends. Finally, Chapter 6 describes a reduced scaling computational method that improves the approximation of mean field excited state energy predictions, increasing the size and complexity of systems that can be treated with high accuracy.

Table of Contents

List of Tables

List of Figures

Acknowledgments

I would like to start by thanking my advisors, Jill Millstone and Daniel Lambrecht, who throughout my Ph. D. work have both inspired me through their unwavering enthusiasm and creativity. Your endless support has provided me with countless rewarding opportunities that have allowed me to grow as an independent scientist. In addition to my advisors, I have had the privilege to work closely with Professor Hannu Häkkinen. Prof. Häkkinen invited me to study with his group in Finland and provided essential guidance and insight throughout our collaboration. Overall, I am incredibly thankful to have each of you serve key mentoring roles during my graduate career and allow me to pursue my own realm of computational nanochemistry.

I would also like to thank my committee members, who have each supported me and provided valuable suggestions throughout my graduate studies. I want to thank the members of both the Millstone and Lambrecht groups who have passed through each lab over the years. I have been lucky to work with a diverse collection of talented scientists who have defined my experience in graduate school both in and out of the lab. I would like to thank Lauren Marbella in particular, who was influential in defining my trajectory in graduate school and who quickly became a key source of inspiration and support in my life.

Finally, I would like to thank my family, especially my parents and my brother. You have taught me how to work hard and encouraged me to pursue my dreams as a scientist while

providing unconditional support at each step along the way. I would not have made it to this point without your love and support.

1.0 Structural and Electronic Predictors of Emergent Properties in Small Metal Nanoparticles

(Portions of this work are being prepared for submission as Hartmann, M. J.; Millstone, J. E. **2018**, in preparation.)

1.1 **Introduction**

Understanding and synthetically leveraging the relationship between the structure and emergent properties of metallic nanomaterials has made them attractive for a range of applications ranging from biomedicine to catalysis.[1-7] Small metal nanoparticles with diameters (*d*) between 1 and 3 nm show distinct properties from both larger nanoparticles ($d > 5$ nm) as well as metal complexes (1–20 metal atoms). The unique behavior observed from small metal nanoparticles originates from their distinctive electronic structure that is at the intersection of discrete states found in molecular systems and continuous, band-like states observed in bulk materials. An accurate description of the electronic structure across this intersection ($d = 1–3$ nm) requires the use of principles from both molecular and bulk theories (importantly, knowing when to invoke one over the other) as well as the incorporation of entirely new concepts specific to this length scale.[8]

The electronic structure is the fundamental parameter that determines the properties of a material, and models that describe the electronic structure across length scale are understood as a function of structural parameters of the system. For example, the electronic structure of both molecular and bulk systems can be understood by the identity and arrangement of each atom composing the material, where each atom's energy level structure and electron configuration defines the basis with which we understand its contribution to the overall electronic structure. In addition, geometry is the primary synthetic handle available to access a desired electronic structure and therefore material property, creating a large incentive to build structure-property relationships for important classes of materials. While geometric and electronic structure are coupled for both molecular and bulk systems, they are each understood within distinct structural paradigms that require different considerations to build predictive models for material properties within each regime. Since small, d = 1–3 nm metal nanoparticles are at the intersection between these two paradigms, the bonding principles that apply to each length scale extreme need to be modified in order to connect the geometric and electronic structures in these systems, and importantly predict their properties that are observed in the lab.

In this perspective, we describe how the properties and performance of small (d = 1–3 nm) metal nanoparticles emerge and are directed as a function of their geometric and electronic structures. We first illustrate how classic concepts of both molecular and bulk electronic structures are driven by system geometric parameters, and consider incremental steps towards the nanometer length scale, demonstrating how these concepts are extended in order to account for new parameters induced by seemingly minor changes in length scale (e.g. including a surface termination in a bulk material). Using the language of both discrete and continuous bonding, we discuss how each structural parameter in d = 1–3 nm metal nanoparticles (i.e. size, shape,

composition, and surface chemistry) contributes to the overall nanoparticle electronic structure and highlight concepts that are unique to the 1–3 nm length scale.

1.2 **Coupling Between Geometry and Electronic Structure**

1.2.1 **Coordination Complexes**

The primary structural parameters that define the electronic structure of coordination complexes are the identity of the metal, symmetry of the ligands around the metal center, and identities of each ligand in the complex. Together, these parameters define the energy level splitting, symmetries of the metal-ligand states, and number of electrons occupying these states. Crystal field theory (CFT) describes how the symmetry of the ligand coordination environment around the metal center modulates the ordering of metal-centered orbitals in the system. The number of electrons in the system, determined by the sum of d-electrons from the metal center and the number of electrons donated by binding from the ligands, describes how to populate the states arising from metal-ligand bonds and the d-orbitals in the crystal field (Figure 1). These simple rules allow for an approximate molecular orbital-type diagram to be constructed for the coordination complex. From CFT, many properties, including optoelectronic and magnetic behaviors, can be predicted with high accuracy.

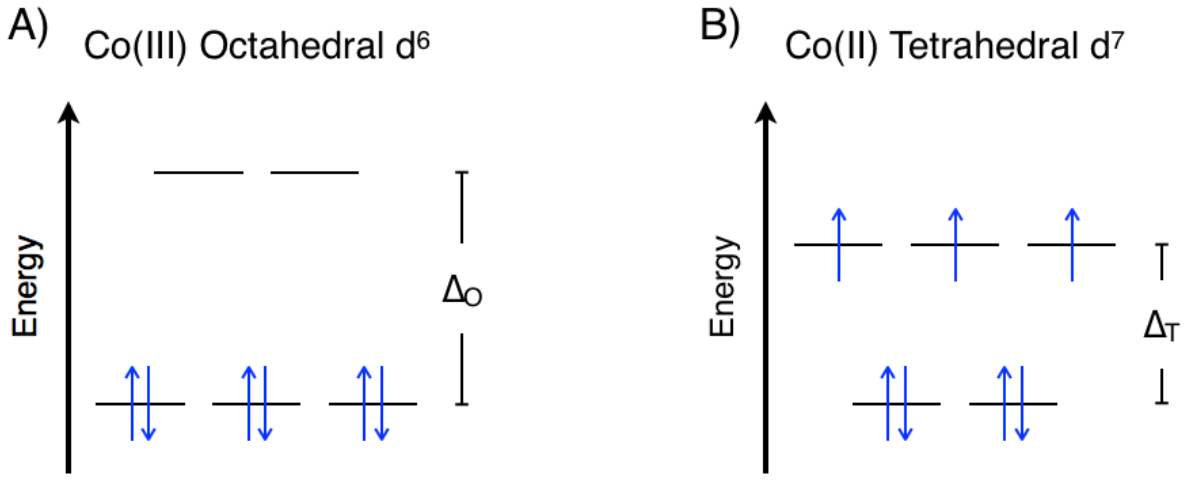

Figure 1. Crystal field diagrams for (A) octahedral and (B) tetrahedral ligand symmetries.

Ligand field theory (LFT) is a useful extension to CFT, which incorporates specific molecular descriptors of the ligands to improve the prediction of the electronic structure of the complex. The spectrochemical effect describes the strength of the field from a particular ligand, determining the energy gap between crystal field states.[9] In addition, the Nephelauxetic effect describes spin pairing energy that originates from inter-electronic repulsion in metal-ligand bonds (and therefore depends on both metal and ligand).[10] For example, a greater extent of orbital localization leads to a higher pairing energy and favors single occupation of higher energy orbitals over double occupation of a low energy state. The combination of energy level splitting and spin pairing energy determines the order in which electrons will populate a given crystal field diagram, allowing for intuitive prediction of the magnetic properties for the complex.

Single metal atom coordination complexes are the smallest metal-containing systems. As we build toward nanoparticles, increasing metal complex size to few-metal-atom clusters requires the additional understanding metal-metal interactions. Isolobal analogies are a simple way to describe how multiple, ligated metal atoms will bond, mapping principles from organic

molecular orbital theory to inorganic chemistry. For example, if the symmetry and energy of the frontier orbitals for each fragment match, the two fragments are likely to form a stable metal-metal bond. Isolobal analogies have demonstrated success in predicting the structures and bonding for many multi-metal atom complexes as well as the formation of previously unknown, and often surprising, heterometallic bonds.[11-12]

Wade and Mingos developed the polyhedral skeletal electron pair theory (PSEPT) that describes bonding in complexes with between 4 and 20 metal atoms, connecting the number of electrons in the complex to the connectivity that defines the overall polyhedral shape of the system, analogous to electron counting rules in single metal atom coordination complexes.[13-14] For example, the electronic structure of the famous butterfly cluster is described by the Wade-Mingos rules. A 60 electron, 4 metal atom system is predicted to be tetrahedral. Upon the addition of 2 electrons to the system, Wade-Mingos rules predict that the tetrahedral geometry will distort to form a butterfly geometry.[15] This example demonstrates the intimate connection between geometry and electronic structure in inorganic complexes, and the Wade-Mingos rules are a powerful framework to understand these relationships.

1.2.2 **Bulk Metals**

The structural parameters that define the electronic structure of bulk metals are metal atom identity and the arrangement of atoms in the crystal lattice. In bulk metal crystals, metallic properties such as conductivity are a result of, and are described by, the band structure of the system. Unlike coordination complexes, crystalline bulk metals contain an effectively infinite number of metal atoms arranged in a periodic lattice. Therefore, the electronic structure cannot be reasonably described by molecular orbital theory originating from specific interactions

between each component of the system. Instead, band theory describes how the symmetry of a crystal and the states within the unit cell form continuous electronic bands.

Work by Hoffmann provides an intuitive connection between molecular orbital theory and band theory.[16] Here, each electronic band is formed from each orbital in the unit cell (assuming the unit cell is isolated from the system), and by considering each permutation of phases in which those orbitals can be linked together, a description of a band can be made. The fully in-phase and out-of-phase combinations define the lower and upper energy bounds of each band respectively, and every energy level in between is filled with states containing different amounts of phase agreement between unit cells. Overall, the unit cell orbitals, the orbital overlap between adjacent unit cells, and arrangement of unit cells determine the band structure of the bulk metal. Specifically, the extent of orbital overlap between adjacent unit cells determines the dispersion of a given band and the symmetry of the orbital determines the run of the band (i.e. up or down in energy with increasing momentum). Finally, the density of states can be determined from the band diagram by considering the number of energy levels per unit energy. An illustrative example is shown in Figure 2 for a linear chain of square planar Pt complexes.

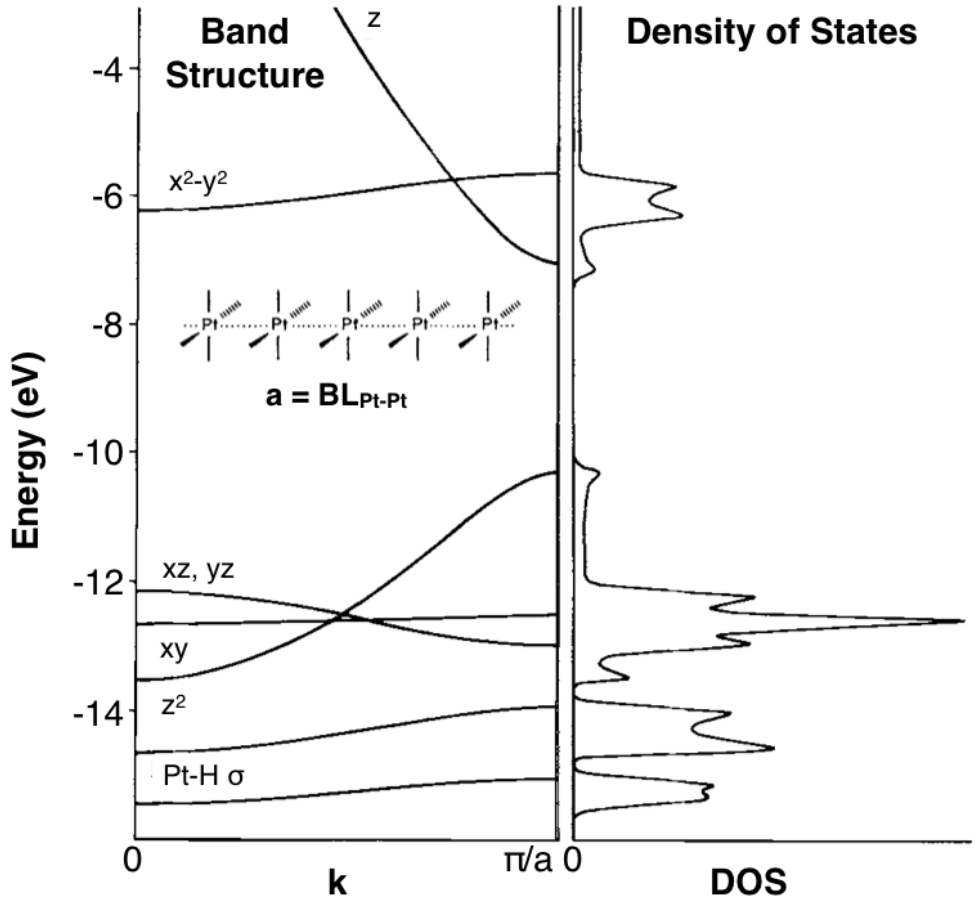

Figure 2. Band diagram and density of states for infinite chain of Pt complexes. Figure adapted with permission from reference 16.

Building towards the nanoparticle size regime from the bulk requires the formation of a surface, which is defined as an interruption of the infinite translational symmetry of a bulk crystal in one direction. The formation of a surface impacts the band structure at the surface, where undercoordination of surface atoms (i.e. dangling bonds) leads to a narrowing of the band and a shift in energy due to less orbital overlap from surrounding atoms. This often results in a compensatory compression[17] or surface reconstruction[18] between the surface and subsurface atoms. The introduction of undercoordination also induces an energy penalty associated with the formation the surface (i.e. the surface energy), defined as the amount of energy per unit area required to form surface.

The introduction of a surface can lead to a number of effects that are important for the properties of bulk metals used in thin films, electrodes, and catalysts, where the surface makes up a small percentage of the system but plays a significant role in interfacial phenomena. For example, the composition of bimetallic surfaces can deviate from the composition in the bulk due to surface segregation behavior, described by the Langmuir-McLean equation.[19-20] In addition, surface adsorbates or capping ligands (capping ligands are intrinsic to nanoparticle structure in the d = 1–3 nm size regime to arrest growth and stabilize the material) can further modify the surface composition depending on the relative interaction strength between the adsorbate and each metal at the surface.[21-22] At the nanometer length scale, the surface becomes increasingly crucial, as it can comprise more than 50% of the total metal atoms for the smallest nanoparticles. Overall, surface identity, composition, and structure are essential parameters that determine the properties of the system, in particular the catalytic activity of a surface, which is known to be correlated with center of the materials d-band.[23-24]

Molecular orbital and band theories that describe metal coordination complexes and bulk metals, respectively, have had great success predicting the connection between geometric and electronic structure that leads to the emergent properties of the system. In small metal nanoparticles (d = 1–3 nm), these two traditional pictures of electronic structure intersect, requiring a combination of these ideas to describe the connection between geometric and electronic structure. The structural parameter space in 1–3 nm nanoparticles is defined by the size, shape, surface chemistry, and composition of the system. Since each of these parameters can have a dramatic impact on the resulting properties, we discuss each in more detail in the following sections.

1.3 **Structural Parameters of 1-3 nm Nanoparticles**

1.3.1 **Size**

The number of metal atoms in the system is the primary parameter that provides a quantitative description of the size dependent properties of 1-3 nm metal nanoparticles. Nanoparticles with d = 1–3 nm typically contain between 25–300 metal atoms, depending on the element composing the metal core. The point at which the electronic structure becomes continuous is ambiguous but is generally defined as the point at which the average spacing between energy levels is less than k_BT. This parameter also depends on metal identity, in particular the atomic electron configuration of the metal in the core. For example, metals with an open d-shell contain more energy levels (5 per atom) over a smaller energy range (d-orbitals have less overlap than s-orbitals and therefore a d-band has smaller dispersion than an s-band),

therefore reaching a higher density of states at the Fermi level than a metal with an open s- or p-shell.

The most well-studied class of small metal nanoparticles are the noble metal nanoparticles, in particular Ag[25] and Au.[26] Metals with open d-shells are generally much more reactive and therefore are more difficult to synthesize and isolate. The electronic structure of noble metal nanoparticle electronic structure is well described by superatom theory, which is a concept specific to the 1-3 nm size range. Superatom theory treats the free electrons (i.e. electrons coming from atomic valence s orbitals) in a system as fully delocalized and calculates their energy levels against a constant, spherical background potential over the entire metal core of the nanoparticle. When the core shape is assumed to be spherical, the resulting solutions have the same symmetry of the atomic orbitals (S, P, D, etc.) but are centered over the entire metal nanoparticle core. The superatom model was originally used to explain the relatively high number of specific sized gas phase Na_N clusters in electron beam experiments (Figure 3A).[27] Häkkinen extended these concepts to monolayer-protected clusters in the 2008, which has been immensely useful in predicting and describing the electronic structures of Au/Ag clusters. Here, the total number of superatomic electrons is given by the number of free electrons from the metals minus the number of electrons localized by a ligand plus the overall charge on the particle.[28] Each Au or Ag atom in a nanoparticle contributes one electron from the s^1 valence electron configuration, and each X-type ligand localizes one superatomic electron into a surface-ligand bond. As the number of electrons (which is directly proportional to size) in the system increases, the HOMO-LUMO gap tends to decrease. The superatomic model of electronic structure has had great success for thiol-capped Au nanoclusters, and predicts the observed non-

linear size dependence of the HOMO-LUMO, where the gap depends primarily on the electronic shell being populated, making it not strictly a function of size (Figure 3B).[26, 29-30]

In addition to predicting optical trends observed in isolated clusters, superatom electronic structure theory has provided a means to identify the point at which thiolate-capped Au nanoparticles start to exhibit metallic behavior[31-33] Negishi et al. synthesized thiolate-capped Au nanoparticles between 38 and 520 gold atoms and separated the particles with high-performance liquid chromatography to isolate fractions with only a couple atom spread.[34] For each fraction, temperature dependent absorption spectra and X-ray diffraction were collected and complemented with DFT calculations to characterize geometric and electronic structure as a function of size. The authors determined that the transition between discrete and bulk electronic structure occurred between 144 and 187 Au atoms. Interestingly, this transition coincided with the emergence of a localized surface plasmon and a change in the crystal structure. At less than 144 Au atoms, finite packing geometries were observed including decahedral and icosahedral cores. Conversely, for sizes containing 187 or more Au atoms, the particles all exhibited face-centered cubic (fcc) packing in the core, which is representative of the atomic packing in bulk crystalline Au.

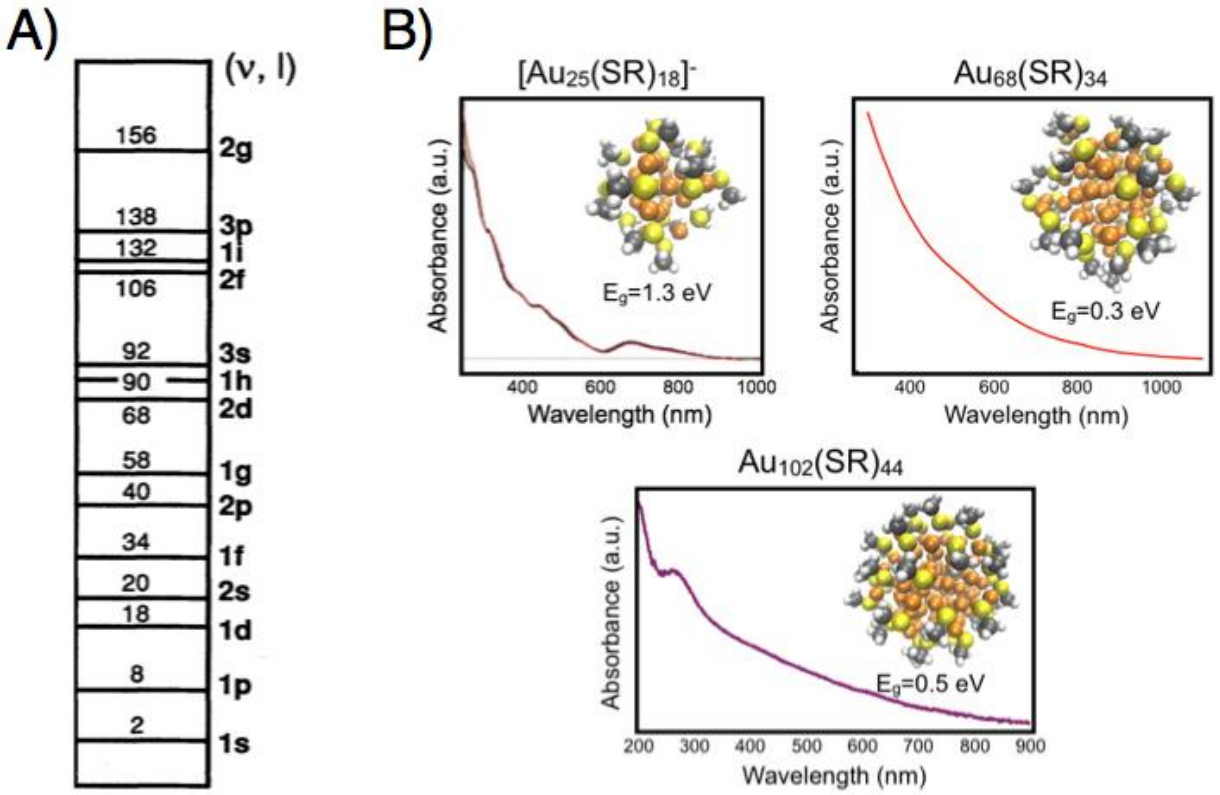

Figure 3. (A) Energy level diagram and magic number electron counts predicted by superatom theory assuming a spherical, square-well potential. (B) Absorption spectra of 3 closed-shell, thiol-capped gold nanoparticles.

1.3.2 **Shape**

The emergence of metallicity occurring simultaneously with a change in size and atom packing illustrates a distinct coupling between size and shape for 1-3 nm metal nanoparticles. Recent work had explored the connection between size and shape further, where the superatom model was extended to account for differences in shape by including the point group of the metal core instead of assuming sphericalicity.[35] Interestingly, this point group analysis was applied to many known thiol-capped gold crystal structures and it was found that lower symmetry cores promote continuous electronic structure at smaller core sizes than for spherical particles.[36] Removing the spherical constraint both improves the prediction of optical properties for these systems and results in superatomic orbital degeneracies to be lifted, effectively increasing the density of states.

The role of symmetry in a nanoparticle core is an essential component in determining final nanoparticle electronic structure. Due to the high percentage of surface atoms in small nanoparticles, optimal orbital overlap between atoms leads to the observation of crystallographic architectures that differ, or do not exist, in the bulk in order to reduce the number of low coordinated surface atoms and minimize the surface energy of the particle. For example, minimization of surface energy leads to the formation of polyhedral shapes that exhibit finite atom packing such as icosahedral or decahedral core symmetries that are not present in bulk systems. These finite size effects directly modify the formation of electronic bands because band formation relies on infinite translational symmetry (*vide supra*). If a system has atoms arranged in a formation without complete translational symmetry, the bands that form will be distorted due to variable atomic orbital overlap at different points within the core. Consider a 55 atom Mackay icosahedron (M_{55}); the ‘d-band’ will exhibit atoms where the phase of the d-orbitals

composing the bands are permuted. However, the longest linear string on atoms in M_{55} is 5 atoms. These 5 atoms can form good orbital overlap, but other atoms nearby will not be ideally packed to participate in similar overlap. Instead, atoms peripheral to this linear string will contribute in positions dictated by specific interactions, mirroring bonding on the molecular scale. This will have an energy penalty that is compensated by a decrease in surface energy associated with the finite packing. In general, each different shape and local atomic packing will lead to a different width and energy level distribution within the d-band.[37] Modifications to d-band distribution can have important consequences for the catalytic behavior of the system by modifying the distribution of d-states or leading to unique surface states, ultimately causing many reactions to exhibit a strong size/shape dependent catalytic activity.[38]

In addition to the core symmetry having a significant impact on the energy level structure of the cluster, many nanoparticle sizes have a range of low-lying isomers of similar energies that emerge because the surface energy and atom packing energy are in competition. This means that a solution of colloidal nanoparticles can exhibit a distribution of particle core shapes, each with slightly different electronic structures. Wales and coworkers demonstrated the structural diversity present in small nanoparticles by modeling the potential energy surface for representative gold nanoclusters containing 55, 85, and 147 atoms.[39] While these model particles did not contain ligands and may not represent realistic particle products in colloidal samples, they show how local stability and specific interactions can play a significant role in determining nanoparticle structure on this length scale. The authors found that at each size, an additional distribution of local coordination environments was found across the most thermodynamically stable isomers. For example, in 85 atom gold nanoparticles, fcc, twinned, decahedral, and ambiguous local coordination environments are expected to be present in isomers within 0.2 eV

of the global minimum structure. In addition, the distribution of local coordination environments in low lying isomers changes as a function of size, where the number of locally icosahedral and ambiguous coordination geometries are expected to decrease with increasing nanoparticle size in favor of locally decahedral, FCC, and twinned coordination environments. These results suggest that not only is nanoparticle shape complicated in 1-3 nm system but size and shape are strongly coupled. Overall, the size and shape of a nanoparticle determine the energy level ordering of the metal core and provide the foundation to understand the impact of composition and surface chemistry on the electronic structure and properties of 1-3 nm metal nanoparticles.

1.3.3 **Composition**

Metal mixing has been used as a strategy to tailor and optimize material properties for millennia, and has defined entire eras by the technology metal mixing has enabled. In the bulk, Hume-Rothery rules describe the likelihood of two metals forming random homogeneous alloys. The three primary Hume-Rothery rules that predict the extent to which two metal atoms will form random substitutional alloys are: 1) the two metals should have a similar valence, 2) the two metals should have similar electronegativity, and 3) the atomic size mismatch between the two metals should be within 15% of each other.[40] While these rules are not strictly quantitative, each outlines the limit in which a local perturbation to the existing structure can limit mixing. If the introduction of a heteroatom introduces too much of a deviation from the desired orbital overlap or distribution of electron density of the host metal defined by the band structure, random mixing becomes unfavorable and leads to phase segregation, intermetallic atomic ordering, or immiscibility. In contrast, molecular heterometallic bonding originates from matching the energy and symmetry of the two metal atoms frontier orbitals, as described by

isolobal analogies (*vide supra*). In 1-3 nm nanoparticles, mixing can be favored by considering both ideas of bonding. Minimizing the perturbation resulting from introduction of a heteroatom often leads to position specific metal mixing, while specific interactions at a surface can drive the formation of novel mixed metal architectures that are otherwise not found.

An example of mixing behavior favored by minimizing heteroatom perturbation of an existing lattice has been explained using the position-dependent local pressure inside a nanoparticle core. Position-dependent pressure is predicted to provide a driving force for heterometallic substitution into specific locations in the nanoclusters. For example, high pressure can be relieved by mixing at particular positions in the nanoparticle with solute atoms that have smaller atomic radii than the solvent metal. Anisotropy in the local pressure provides an additional handle that can result in favorable substitution of a secondary metal as well as dictate the final nanoparticle spatial composition architecture. Here, the local compression around substitution positions accumulates as the number of secondary metal atoms increases, leading to symmetry breaking and nanoscale phase segregation to produce core-shell nanoparticles, a mixing behavior governed by the accumulation of strain that is analogous to Stranski-Krastanov thin-film growth. Importantly, the emergence of unique coordination site sand strain fields within a nanoparticle core is essential in allowing mixing between metal combinations immiscible in the bulk, such as Au/Co.[41-42]

The prevalence of specific nanoparticle architectures driving positional doping is best known from doped analogues of the $[Au_{25}(RS)_{18}]^-$ nanocluster. $[Au_{25}(RS)_{18}]^-$ is an 8 electron, spherical superatom with an icosahedral core and 6 octahedrally arranged $Au_2(SR)_3$ 'staples' surrounding the core. The stability of $[Au_{25}(RS)_{18}]^-$ originates from a combination of electronic and geometric shell closings, making it the most accessible and well-studied nanocluster. A

number of heteroatoms have been doped into $[Au_{25}(RS)_{18}]^-$, including metals from groups X, XI, and XII. Due to equal valence and thus, contribution to the superatom electron configuration, a range in the number of Cu and Ag atoms can be introduced to the structure.[43-44] In addition to group XI metals, group X metals Pd and Pt can be added to the $[Au_{25}(RS)_{18}]^-$ framework. In this case, instead of the anionic cluster, the neutral cluster is formed, leading to a superatomic electron configuration of $1S^2\ 1P^4$ and a corresponding Jahn-Teller distortion to account for the degeneracy of the HOMO orbitals.[45] Likewise, group XII metals such as Cd and Hg can be doped into the Au_{25} framework to form the neutral version of the system that preserves the 8 electron superatom.[46] Because of the stability of 8 electron systems, only a single dopant atom from groups X and XII have been observed. Additionally, the position of the substitution plays a key role in determining how a given substitution modifies final particle properties. $[Au_{25}(SR)_{18}]^-$ has three unique substitution positions, each of which impacts the electronic structure and predicted optoelectronic properties differently. The overall symmetry after heteroatom substitution and specific features of the heteroatom both play an important roles for controlling energy level structure of the system.[47]

Many studies have explored position-dependent doping in $[Au_{25}(SR)_{18}]^-$, however compositional architecture of small bimetallic nanoparticles is an important feature across the 1–3 nm regime. For example, Substituting both Cu and Ag into $Au_{144}(SR)_{60}$ also results in position-dependent optoelectronic properties (Figure 4). Introducing Cu to the core of the $Au_{144}(SR)_{60}$ nanoparticle results in the emergence of plasmonic behavior at particle sizes smaller than the pure gold, while Cu substitution in the surface staple layer is not predicted to induce a plasmonic response.[48-49]

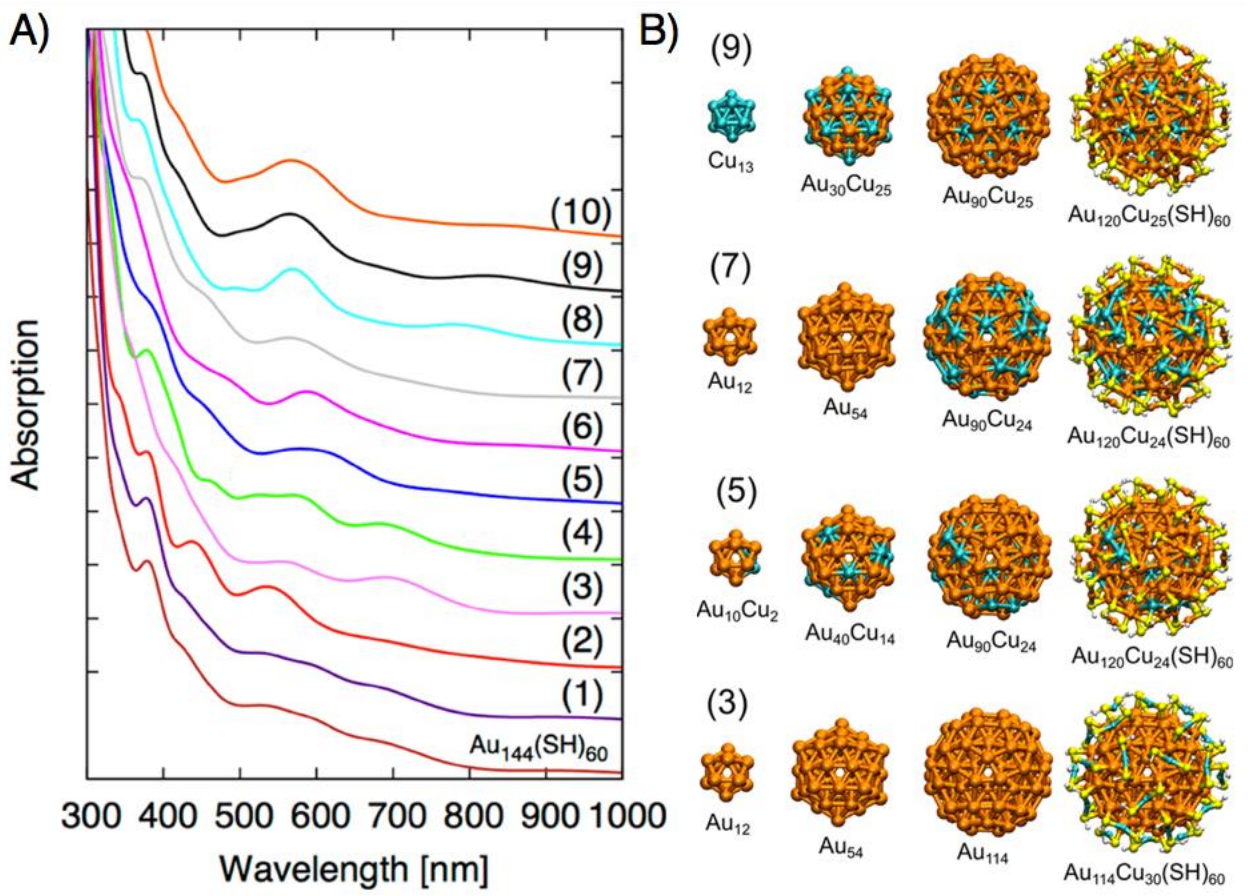

Figure 4. Calculated absorption spectra for different composition architectures of $Au_{(144,145)-x}Cu_x(SH)_{60}$ nanoclusters. Numbers indicate the isomer used in calculation. (B) Shell-by-shell $Au_{(144,145)-x}Cu_x(SH)_{60}$ structures with Cu substitution in staple layer (3), randomly positioned (5), outer core (7), and inner core (9). Figure adapted with permission from ref 49.

For copper substitution into a gold nanocluster, the surface staple layer is the thermodynamically preferred location, yet the kinetically stable architecture with Cu in the core is necessary to induce a plasmonic response. In general, the balance between thermodynamic and kinetic factors is essential for controlling nanoparticle composition architecture and resulting properties. Another example is magnetic $Fe_{50}Pt_{50}$ nanoparticles, which can be synthesized with diameters down to 3 nm. Initially these particles form disordered, face centered cubic crystal structures. Upon thermal annealing, the core structures rearrange to form the well known, thermodynamically favored $L1_0$ intermetallic phase seen in bulk PtFe.[50] The phase transition is essential to allow these magnetic nanoparticles to self organize into ferromagnetic thin films of particles, which show promise for high density magnetic recording applications.

While many density functional theory studies have demonstrated that the relative position/arrangement of atoms in bimetallic nanoparticles are important for particle properties, gaining synthetic control of composition architecture remains difficult. In order to gain a continuously tunable handle on the final particle atom concentration and composition architecture, the particle product must be kinetically controlled, and small metal nanoparticles provide the unique opportunity to leverage kinetic factors during synthesis to direct the formation of target architectures. Millstone and coworkers leveraged the surface chemistry intrinsic to colloidal nanoparticle stability to mimic the diffusion-quench approach used in bulk alloy formation to kinetically trap controlled spatial composition architectures in bimetallic AuCu nanoparticles. Precursor chemistry was shown to control the kinetics of formation and therefore heteroatom arrangement within the nanoparticle. Here, it was found that bimetallic Au and Cu precursors lead to the formation of randomly mixed AuCu alloy nanoparticles, and separation of the metals into different precursors lead to phase segregation, with Cu being found

exclusively on the surface of the particle. Overall, this work demonstrates that strong metal-ligand surface bonding raises the barrier to surface driven metal segregation to stabilize the randomly mixed alloy (kinetically trapped).[51]

This approach was successfully employed to make 2 nm bimetallic nanoparticles of AuCu and AuCo with full composition tunability. Not only did this method avoid the formation of well known intermetallic architectures with AuCu, but Au and Co are not miscible at any length scale, indicating the power and generality of using the ligand shell to gain kinetic control of final particle architecture. Due to the colocalization of two metals into a single nanoparticle, new properties not accessible in the other system were realized. Upon the introduction of Cu, the emission wavelength seen in d ~2.0 nm Au nanoclusters was shifted as a function of percent Cu across the NIR by up to 100 nm, providing a compositional handle to tune emission properties.[4] Likewise, the presence of Co in the Au host lattice introduced an additional superparamagnetic property to the particles without losing the emissive behavior of Au, making the particles interesting as dual NIR-MRI contrast agents.[5]

1.3.4 **Surface Chemistry**

Nanoparticle surface chemistry not only provides an essential kinetic handle on particle formation and composition control, but also is key component of the overall nanoparticle electronic structure. In fact, the large percentage of surface in small nanoparticles makes the surface chemistry an inseparable, and often primary, determinant of nanoparticle properties.

The primary bulk variable that describes ligand adsorption to a surface is the surface chemical potential, which is a measure of the free energy change upon the addition of a ligand to the surface. While most descriptions of small nanoparticle surface chemistry pertain to specific

interactions, it has been shown that the surface chemical potential is a vital parameter for nanoparticle isolation, even in systems with complex surface structures. Taylor and Mpourmpakis sampled nanoclusters with known crystal structures, and showed that formation and crystallization is favored when the cohesive energy of the core and the core-to-ligand binding energy were approximately equal (Figure 5A). The authors demonstrated that these interfacial interactions were at a point that balances the chemical potential at the interface. This result has two important consequences; 1) even though nanoparticles are kinetically trapped products, thermodynamic driving forces for formation are important. 2) Even though these clusters have atomic level texture and curvature on the surface, bulk descriptions of ligand bonding still apply for predicting which architectures are stable. This work introduces an important constraint for rational design strategies of new nanoparticles, where bulk thermodynamic principles are the driving force for formation and isolation of desired particle products.[52]

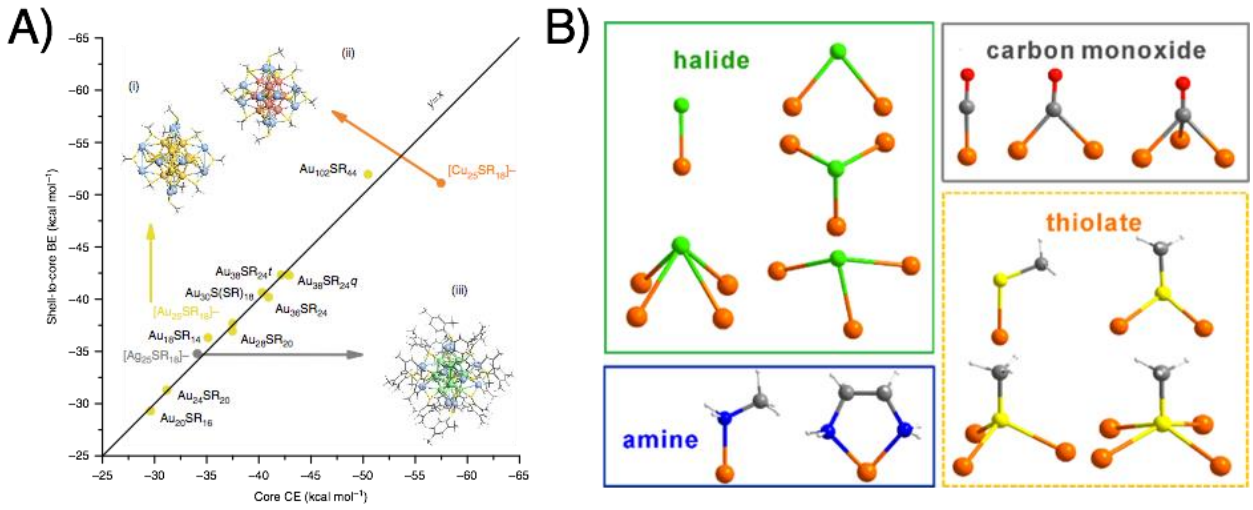

Figure 5. (A) Correlation between surface-staple binding energy and cohesive energy in the core. (Adapted with permission from ref 52) (B) Diversity of surface binding motifs for a number of common nanocluster surface ligands. (Adapted with permission from ref 53)

Despite success using bulk thermodynamic descriptions of nanoparticle surface chemistry to describe structure and binding, molecular coordination chemistry drives many of the observed properties originating from the surface chemistry of 1-3 nm nanoparticles. The most well-studied metal-ligand combination are gold-thiolates, which are known to form a number different surface structures, including standard binding modes (on top, bridge, or hollow) as well as 'staple' geometries.[53] Other small molecule ligands, such as halides, carbon monoxide, and phosphines form a variety of stabilizing surface chemistries (Figure 5B) and impact the catalytic properties and optical features.[54] Since 40% - 90% of atoms in 1-3 nm NPs are at the surface, metal-ligand surface construction has a dramatic, and often deterministic, impact on final particle properties. While controlling the distribution of metal-ligand structure presents a synthetic challenge, there is also great opportunity for discovery and optimization of new nanoparticle properties.

An example of the profound impact the nature of the metal-ligand bond has on the properties of the system was demonstrated computationally by considering the calculated magnetic properties of cobalt nanoclusters for a suite of ligands.[55] Using density functional theory (DFT), we showed that the nature of the bond with the surface (i.e. X-type vs. L-type) introduced two fundamentally different electronic effects on the nanocluster. X-type ligands are those that contribute one electron to the bond with the surface, and were predicted to lightly quench the magnetic moment of the cluster relative to the bare system. Alternatively, L-type ligands that bind datively to the surface were predicted to quench the magnetic moment of the cluster more than X-type. Overall, a correlation between the charge on the cluster and total magnetic moment of the cluster was observed, analogous to oxidation state dependent magnetic behavior in coordination complexes (Figure 6A).

The evolution of X- and L-type ligand impact when bound to nanoparticle surfaces were studied as a function of size by considering a range of Co_N nanoparticles ($13 \leq N \leq 55$) capped with Cl and PH_3 model ligands. It was found that the ligand binding motif impacted the magnetic properties of each Co_N core across the size range studied, demonstrating that the difference in binding motif was the main driver of magnetism in these systems. The major difference between the two bond types was shown to be the relative alignment between ligand binding orbitals and the edges of Co electronic bands. Briefly, the X-type ligand considered (Cl) exhibited agreement with both the energy of the hybridizing states and symmetry between the states. This allows for Cl to seamlessly hybridize with the entirety of the d-band and effectively extend these states across the surface, and therefore have little impact on the original magnetism. The L-type ligand considered (PH_3) does not have energy alignment with the electronic states of Co, and therefore forms a more traditional bonding-anti bonding pair of states. The magnetic moment quenching

behavior observed with L-type ligands is from occupation of previously unoccupied states by the lone pair of PH_3. The ligand-dependent magnetic moments were also shown to mediate the size dependence of Co_NL_M magnetism. In bare clusters, local coordination environment is known to dictate local magnetic moment, where lower coordinated metal atoms tend to have higher magnetic moments.[56-57] Upon the addition of a ligand shell, size dependent trends persist, but are mediated by the identity of the ligand shell itself (Figure 6B).[58]

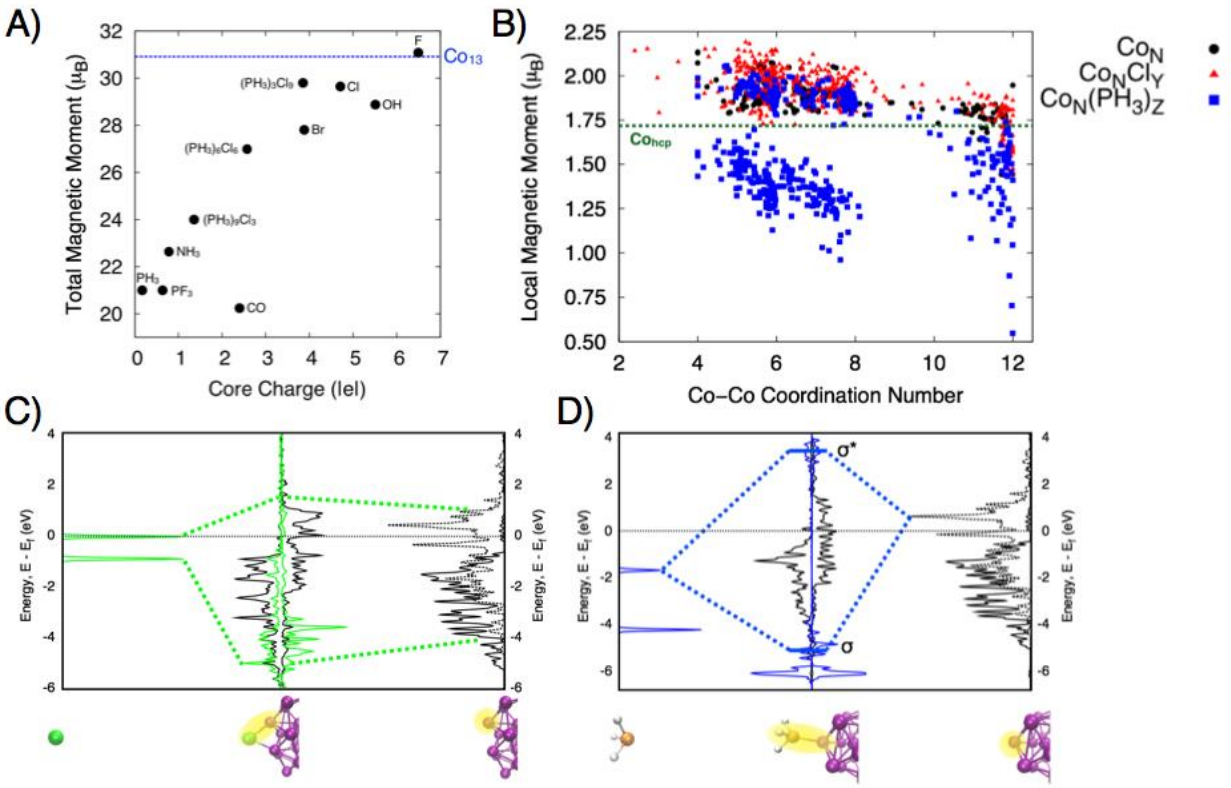

Figure 6. (A) Total magnetic moment as a function of core charge for $Co_{13}L_{12}$ clusters. (Adapted with permission from ref 55) (B) Local magnetic moment of each coordination environment in bare, Cl-passivated and PH_3-passivated Co_N nanoclusters ($15 \leq N \leq 55$). (C) Density of states for hybridization of Cl with Co surface atom. (D) Density of states for hybridization of PH3 with Co surface atom. (Adapted with permission from ref 58)

In addition to the nature of the Co-ligand bond being the dominant driver of overall nanocluster magnetism, specific molecular descriptors within each ligand class that are important in coordination chemistry were seen to impact the overall electronic structure and resulting magnetism of the clusters. First, π-backbonding was shown to cause a deviation from the standard charge vs. total magnetic moment correlation demonstrated across the clusters. Additionally, the Nephelauxetic effect was a key parameter in determining trends in within the X-type ligand group. In coordination complexes, the Nephelauxetic effect is secondary and can often be neglected in determining spin state and optical properties such as the spectrochemical effect. Interestingly, while both effects still exist in principle, their relative importance in nanoclusters is reversed relative to in coordination complexes. At a nanocluster surface, only a few ligands can participate in the local coordination environment of a single surface metal atom, the remainder will be from the surrounding particle. The combination of not being the full coordination sphere, lower symmetry around a surface atom, and hybridization of the d-orbitals with the other metal atom d-states means there is no discernible splitting for the spectrochemical effect to modulate. In other words, the local density of states of an atom in a nanoparticle will always lead to high spin electron configuration. The impact of the Nephelauxetic effect is similar in nanoparticles as in coordination complexes and is seen to modulate the overall spin state of the cluster. This is an example of how the principles from coordination chemistry need to be modified in order to apply to nanoparticle surfaces.

The different behavior between X-type and L-type ligands has been shown to be important experimentally for the optoelectronic response of small Au nanoparticles. Here, we synthesized 1.7 ± 0.3 nm Au nanoparticles capped with an L-type phosphine ligand (4-(diphenylphosphino) benzoic acid (DPPBA)). The DPPBA capped particles did not initially

show any photoluminescence. Upon the introduction of an X-type, thiolated ligand via ligand exchange, near infrared emission emerges. In addition to the difference in head group, this work demonstrated and secondary yet significant impact of ligand chain length on the measured photoluminescence figures of merit (i.e. quantum yield).[59]

1.4 **Summary and Outlook**

Small metal nanoparticles ($1 \leq d \leq 3$ nm) are at a unique size range where every atom contributes a non-negligible amount to the overall particle electronic structure and resulting properties. A deep connection between geometric parameters and electronic structures exists for both molecular and bulk systems and provides the foundation in which we understand their respective properties. At both length scales, the identity of each atom comprising the system and interactions between them provides the basis for this understanding. In 1-3 nm nanoparticles, which are at the intersection between discrete and continuous electronic structures, the atom remains the basis for describing material properties, however the length scale dictates the available geometric parameters that define the electronic structure. Here, we discuss each structural parameter available to the 1-3 nm nanoparticles, and describe how each impacts their electronic structure and resulting properties. We do this by pulling from classic concepts of metal electronic structure, including both coordination chemistry as well as bulk metals. Overall, concepts from each length scale extreme describe aspects of bonding in small metal nanoparticles, however specific interactions present in a given nanoparticle dictate the relative importance of these concepts. In addition, new concepts specific to the 1-3 nm length scale emerge (e.g. superatom theory) that are important to understand the behavior of the system.

The structural complexity present in small metal nanoparticles makes the atom-by-atom decomposition of geometry into electronic structure difficult due to distributions in particle size, isomers, and surface bonding that are intrinsic to colloidal samples. However, the development of new models that both are specific to the nanometer length scale as well as translate across length scales presents great potential for significant payoff. Both molecular orbital theory and band theory have not only shaped the way we think about molecular and bulk systems, but also have paved the way for development in their respective fields. Predictive models that connect the geometric and electronic structures of small metal nanoparticles will shape how we teach nanochemistry to young scientists and direct the evolution of the field over the coming decades.

2.0 Impacts of Copper Position on the Electronic Structure of $[Au_{25-x}Cu_x(SH)_{18}]^-$ Nanoclusters

(Portions of this work were published previously and are reprinted with permission from Hartmann, M. J.; Häkkinen, H.; Millstone, J. E.; Lambrecht, D. S. *J. Phys. Chem. C* **2015**, 8290-8298. Copyright 2015 American Chemical Society.)

2.1 **Introduction**

Noble metal nanoparticles (NMNPs) show unique, size-dependent optical properties, in large part due to effects that specifically arise in spatially confined materials.[60-63] For example, pseudospherical nanoparticles with core diameters between approximately 3 - 100 nm exhibit a localized surface plasmon resonance (LSPR) as their dominant optical feature.[64-67] However at smaller sizes, the LSPR is no longer spectroscopically discernable due to phenomena such as surface dampening[68] and the increasing dominance of bound electronic transitions from energy level discretization.[69] Instead, new absorption and photoluminescent behaviors arise.[70] Understanding nanoparticle optical properties as a function of size is not only an opportunity to study the emergence of fundamental optical phenomena, but also to predict and leverage key aspects of nanoparticle electronic behaviors already used in applications such as heterogeneous catalysis[71-73] and bioimaging.[74-75]

In recent years, studies of the electronic properties of small NMNPs (13 - 300 atoms, 1.0 - 3.0 nm) have focused on atomically precise nanoclusters.[26, 30, 76] Atomically precise materials allow one to directly probe how atomic structure impacts electronic properties. These well-defined architectures also provide targets that are experimentally accessible yet small enough to be handled practically *in silico*. These systems are typically on the low end of the 1.0-3.0 nm size range and are electronically unique because they lie at the interface between discrete molecular orbital levels and the band structure observed in bulk metal materials.[72]

Yet, the transition from molecular orbital structure to the band structure observed in metals is not a well-defined pathway in itself. The prevailing model to explain the electronic structure of these small NMNPs describes their stability as closed, superatomic electron shells.[77-79] Due to a high number of symmetry elements present in these clusters, groups of nearly degenerate orbitals are often observed, each exhibiting global symmetries that are reminiscent of the canonical atomic orbitals. This model is exceptionally effective for describing the stability of many cluster systems,[78, 80] although variations in cluster geometry[29, 81] and ligand shell architectures[82-83] can produce deviations from superatom predictions.

Whether guided by the superatom model or another description of electronic structure, interpretation and design of metal cluster electronic properties must incorporate the impact of cluster composition. Introduction of new metals into an existing and well-defined monometallic architecture can induce a variety of effects on both the structure and properties of the resulting particle including shifts in the ground state electron distribution,[84-85] changes in local bonding patterns,[86] and disruption of existing symmetries.[87] However, it is currently impossible to synthetically tune the position of specific metal atom insertions with geometric precision,[88] and therefore the empirical correlation of heteroatom position with NMNP electronic structure is

limited, although it is already known that significant effects may be induced.[89] Here, simulation provides an ideal method to achieve the essential, atomic resolution required to correlate metal atom substitutions with NMNP electronic structure, and produce key insights into the optoelectronic impact of not only cluster composition, but also cluster compositional architectures.

Herein, we present a computational study of the structural, electronic, and optical properties of $[Au_{25-x}Cu_x(SH)_{18}]^-$ clusters ($x \leq 2$) comprehensively considering heteroatom position in addition to overall cluster composition. Previously, Au-Cu mixing has been shown to induce systematic changes in the optical behavior of NMNPs,[4] where increasing Cu content leads to progressively red-shifted photoluminescence emission in the near-infrared. For this study, $[Au_{25}(SH)_{18}]^-$ provides a robust starting size to establish a bottom-up understanding of electronic structure while still remaining experimentally relevant.[30] Specifically, $[Au_{25}(SH)_{18}]^-$ provides two crucial elements to the study: 1) it has a well-defined electronic structure and 2) the system has a known crystal structure with 3 symmetrically unique substitution sites, namely the middle (M), edge (E), and staple (S) positions. Having only 3 unique sites allows complete and systematic sampling of conformational space for up to 2 Cu atoms. We use simulated absorption spectra and other supporting electronic structure descriptors, such as electron density radial distribution functions (RDFs), Bader charge analysis,[90] and energy level diagrams to distinguish and elucidate the impacts of heteroatom concentrations and geometric positions within NMNP electronic structure.

2.2 **Computational Methods**

Calculations were performed using density functional theory (DFT) as implemented in GPAW (grid-based projector augmented wave method).[91-92] Structural optimizations were performed using the local density approximation[93] (LDA) exchange correlation functional, with a grid spacing of 0.2 Å, a convergence criterion of 0.05 eV/Å for the residual force, and were performed without a symmetry constraint. The LDA exchange correlation (XC) functional is known to reproduce Au-Au bond distances better than higher-level functionals.[78] The GPAW setup for Au and Cu includes scalar relativistic corrections. The optical absorption calculations were completed using the relaxed structures with Casida's formulation of linear response time dependent density functional theory (LR-TDDFT),[94] using the Perdew-Burke-Ernzerhof[95] (PBE) exchange correlation functional. PBE has been shown to provide good HOMO-LUMO gap estimates for similar Au nanoclusters at low costs compared to other XC functionals.[96] Casida's formulation of LR-TDDFT expands the transition in an electron-hole basis, resulting in a set of discrete transitions each with a given energy and oscillator strength. These discrete transitions were folded with Gaussian broadening of 0.05 eV into smooth curves for presenting. The formation energy (ΔE_{form}) is calculated from the following stoichiometrically balanced equation.

$$\Delta E_{form} = E\left[Au_x Cu_y (SH)_{18}^-\right] + 9 * E[H_2] - x * E\left[Au_{fcc}\right] - y * E\left[Cu_{fcc}\right] - 18 * [SH_2]$$

Crown ether systems were optimized with the PBE XC functional, a grid spacing of 0.2 Å, and a convergence criterion of 0.05 eV/ Å.

Radial distribution functions of the change in electron density from the HOMO-LUMO excitation were calculated from in-house python code. The script uses the Kohn-Sham (KS) occupied and virtual orbital pairs participating in the transition, weighted with the calculated oscillator strength as shown in the following equation:

$$\Delta\rho(r_k) = \sum_{i,a} f_{i\to a}[\psi_a(r_k)\psi_a^*(r_k) - \psi_i(r_k)\psi_i^*(r_k)]$$

Here, $\Delta\rho$ is the difference density, ψ_i (ψ_a) is an occupied (virtual) orbital, and $f_{i\to a}$ is the corresponding oscillator strength. These RDFs are evaluated on a real-space grid, where r_k is the distance from the center atom to the k^{th} grid point.

2.3 **Results**

2.3.1 **The $[Au_{25}(SR)_{18}]^-$ System**

In this study we use the experimentally solved crystal structure of the $[Au_{25}(SCH_2CH_2Ph)_{18}]^-$ nanocluster[30] as a model system, replacing the phenylethane thiol ligand with a simple SH group. The structure of the $[Au_{25}(SH)_{18}]^-$ cluster is shown in the inset of Figure 7 and has a central Au atom enclosed by an icosahedron consisting of 12 Au atoms. This 13 atom metal core is then stabilized by an octahedral arrangement of 6 staples, each consisting of alternating Au atoms and thiol ligands with the formula of $Au_2(SH)_3$.[30, 97] The calculated bond lengths of each region of the cluster are in good agreement (<1%) with the crystal structure[30] (Table 1).

Table 1. Calculated and experimental bond lengths for each region of the $[Au_{25}(SR)_{18}]^-$ cluster. R=H for calculations, and R=2-phenylethane thiol in crystal structure (standard deviations in parentheses).

Section	Average Bond Length (Å)	Crystal Structure Bond Lengths (Å)
Middle-Edge	2.77 (0.01)	0.01 (0.01)
Edge-Edge	2.92 (0.09)	2.93 (0.06)
Edge-Sulfur	2.38 (0.01)	2.38 (0.01)
Au-S in Staple	2.30 (0.01)	2.32 (0.01)

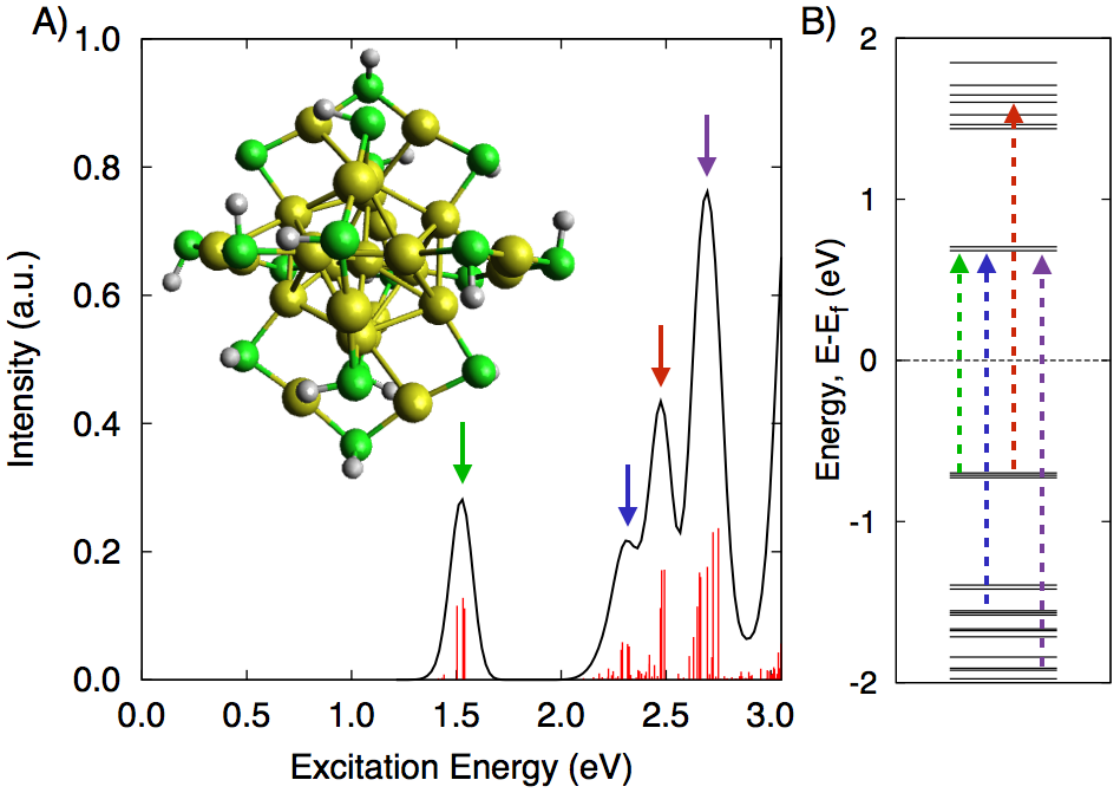

Figure 7. Calculated absorption behavior of $[Au_{25}(SR)_{18}]^-$ cluster (A) absorption spectrum and (B) energy level diagram showing peak assignment. (Inset) $[Au_{25}(SR)_{18}]^-$ structure: yellow, gold; green, sulfur; gray, hydrogen.

The discrete (red) and Gaussian folded (black) optical absorption spectrum of the $[Au_{25}(SH)_{18}]^-$ cluster are shown in Figure 7A along with the corresponding orbital diagram interpretation in Figure 7B. The electronic structure of this cluster is commonly described as an 8 electron superatom.[98] In an analysis by Aikens,[99] the first peak centered at approximately 1.5 eV is assigned to the HOMO-LUMO transition between a triply degenerate set of orbitals with P symmetry (HOMO, HOMO-1, and HOMO-2) and doubly degenerate orbitals with overall D symmetry (LUMO and LUMO+1). Throughout this study we will refer to this entire first absorption feature centered around 1.5 eV as the "superatomic HOMO-LUMO transition." Note that the superatomic HOMO-LUMO description is different than the usual description of the HOMO-LUMO transition, which is calculated here as the difference between HOMO and LUMO orbital energies and can be seen experimentally as the onset of optical absorption. Due to the near degeneracies of the HOMO, HOMO-1, and HOMO-2 and the LUMO and LUMO+1 orbitals, the superatomic HOMO-LUMO transition has 5 total orbitals participating. Both transitions will be discussed in the text and standard HOMO-LUMO gap is reported in Table 2.

Table 2. Formation energies and HOMO-LUMO gaps for the pure Au cluster and each monosubstituted system.

System	Formation Energy (meV)	HOMO-LUMO Gap (eV)
$[Au_{25}(SH)_{18}]^-$	877	1.38
$Au_{24}Cu_1$ (M)	821	1.17
$Au_{24}Cu_1$ (E)	723	1.37
$Au_{24}Cu_1$ (S)	715	1.33

2.3.2 **Substitution Position**

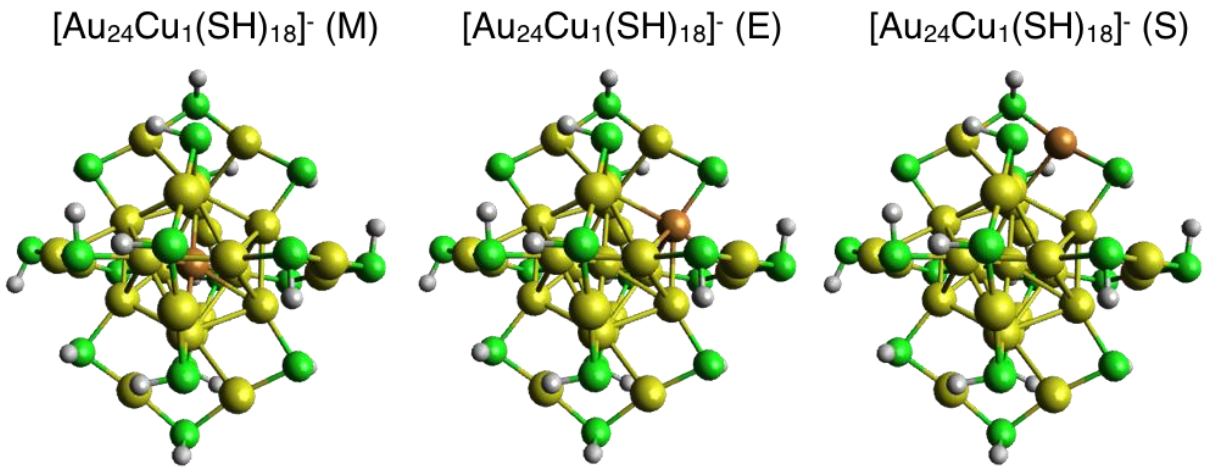

Figure 8. Structures associated with each single position substitution of Cu in a $[Au_{25}(SH)_{18}]^-$ cluster: yellow, gold; orange, copper; green, sulfur; gray, hydrogen.

Figure 8 shows possible single copper substitution sites in $[Au_{25}(SH)_{18}]^-$. As shown in Table 1, substitution of a Au atom by Cu in $[Au_{25}(SH)_{18}]^-$ leads to formation energies that are smaller, and therefore more stable. There is also a position dependence on the energy of formation, with the staple being the most stable substitution site, followed by the edge, and finally the middle position. The thermodynamic prediction of Cu in the staple is consistent with previous XAS measurements.[100] However, because of the narrow range in formation energies, we can expect each position to coexist in relative ratios of approximately 1:45:60 at room temperature for the middle, edge, and staple positions respectively, based on a Boltzmann weighting procedure, where the relative amount of each isomer is determined using the following formula, where E is the energy of an isomer, k_B is Boltzmann's constant, and T is the absolute temperature.

$$\frac{[Isomer\ j]}{[Isomer\ i]} = \frac{n_j}{n_i} e^{\frac{E_i - E_j}{k_B T}}$$

The added stability is likely due to the presence of Au-Cu bonds, which have been shown to be more stable than either Au-Au or Cu-Cu bonds.[101]

As shown in Table 2 the calculated HOMO-LUMO gap of the pure Au cluster is 1.38 eV, consistent with the experimentally measured onset of absorption.[102] The substitution of Cu in the center of the cluster induces a closing of the HOMO-LUMO gap by 0.21 eV, to 1.17 eV, consistent with previous reports.[103-104] The asymmetric substitutions in the edge or staple do not induce a large change in the HOMO-LUMO gap, which remain at 1.37 and 1.33 eV, respectively. These HOMO-LUMO gaps calculated are in qualitative agreement with a report by Negishi et al., where they use a hybrid DFT functional, to model the substitution of Cu into $[Au_{25}(SH)_{18}]^-$.[104]

Table 3. Bader charges for $[Au_{25}(SH)_{18}]^-$ and corresponding monosubstituted clusters.[a]

Metal Position	Au_{25}	$Au_{24}Cu_1$ (M)		$Au_{24}Cu_1$ (E)		$Au_{24}Cu_1$ (S)	
	Au	Au	Cu	Au	Cu	Au	Cu
Middle	-0.10	-	0.35	-0.15	-	-0.10	-
Edge	0.03 (0.01)	0.00 (0.01)	-	0.04 (0.10)	0.37	0.02 (0.02)	-
Staple	0.08 (0.02)	0.08 (0.01)	-	0.08 (0.02)	-	0.10 (0.09)	0.38

[a]Shows net charge on each metal atom (in e) as a function of position in the cluster (when there is more than one atom at a given position in the cluster, averaged values are reported with standard deviation in parentheses).

Table 3 shows the atoms-in-molecules Bader charge analysis,[90] listed by each metal atom type and sorted by position within the cluster. In the pure Au cluster, the center atom assumes a slightly negative charge of -0.10 |e|. All other Au atoms in the cluster are slightly positive, scaling with increasing proximity to electronegative sulfur atoms. Each of the 18 sulfur atoms accumulates an average charge of -0.13 |e|, which together with the metal atoms comprise the overall cluster charge of -1. When Cu is substituted at any position, the effect of the electronegativity difference between Au (2.54) and Cu (1.90) becomes apparent. When Cu is in the center of the cluster, the charge at the middle atom changes by almost half on an electron to +0.35. The same trend is also true for the edge and staple substitutions. Copper assumes a partial positive charge of 0.37 and 0.38 respectively. The presence of Cu also has a slight impact on the

partial charges on the nearby Au atoms. For example, when Cu is on the edge, the middle Au atom assumes a slightly more negative charge of -0.15 |e|. The overall distribution of electron density is a function of both the local and global arrangement of the electronegative atom impurity in the cluster, comparable to the ground state partial charges of traditional organic molecules containing heteroatoms. The complete Bader charge analysis for each doubly-substituted system is summarized in Table 4.

Table 4. Summary of the atomic Bader charges (in e) of each $[Au_{23}Cu_2(SH)_{18}]^-$ system (standard deviation is indicated in parentheses)

System	Metal Type	Position in Cluster		
		Middle	Edge	Staple
ME	Au	-	-0.02 (0.02)	0.08 (0.01)
	Cu	0.33	0.33	-
MS	Au	-	-0.01 (0.01)	0.08 (0.01)
	Cu	0.33	-	0.42
ES	Au	-0.15	0.01 (0.03)	0.07 (0.01)
	Cu	-	0.34	0.35
SS non	Au	-0.09	0.01 (0.02)	0.08 (0.01)
	Cu	-	-	0.39
SS adj	Au	-0.09	0.01 (0.02)	0.08 (0.01)
	Cu	-	-	0.39
EE adj	Au	-0.19	0.00 (0.03)	0.07 (0.02)
	Cu	-	0.36	-
EE non	Au	-0.18	0.00 (0.02)	0.07 (0.01)
	Cu	-	0.37	-
EE opp	Au	-0.20	0.00 (0.01)	0.07 (0.01)
	Cu	-	0.37	-

The absorption spectra for $[Au_{25}(SH)_{18}]^-$ and each monosubstituted system are shown in Figure 9A, and are in good agreement with those reported by Negishi et al.[104] The presence of a single Cu at any position does not change the overall shape of the absorption spectrum from the pure Au cluster, however Cu induces position dependent variations in each simulated spectrum. For example, when Cu is in the center of the cluster, the HOMO-LUMO gap shrinks and produces an overall red-shift in each absorption feature. A Cu atom at the edge position results in a slight blue-shift of the absorption maximum of the HOMO-LUMO transition and a broadening in the HOMO-LUMO peak. Finally, Cu in the staple position produces a new absorption feature just below 2.0 eV, that is not observed either in $[Au_{25}(SH)_{18}]^-$ or in the spectra of clusters substituted at middle and edge positions. Taken together, these data suggest that there is a general absorption motif (e.g. number and relative intensity of electronic transitions) for the $[Au_{24}Cu_1(SH)_{18}]^-$ clusters, but also that the energy (and possibly splitting) of these transitions varies significantly with compositional *architecture* (i.e. not stoichiometry alone). We consider below the impact of substitution at each geometric position.

It should be noted that heteroatom substitution may change the geometry of the cluster and that these distortions, not the presence of the heteroatom itself, may result in the electronic structure changes observed. For example, a possible explanation for the closing of the HOMO-LUMO gap when Cu is in the middle could be due to a contraction of the crystal structure: the shorter Au-Cu bond distance could produce a destabilization, causing the HOMO-LUMO gap to close. To test this, we performed single point calculations for $[Au_{25}(SH)_{18}]^-$ with the $[Au_{24}Cu_1(SH)_{18}]^-$ (M) geometry, and $[Au_{24}Cu_1(SH)_{18}]^-$ (M) at the $[Au_{25}(SH)_{18}]^-$ geometry. In each case the HOMO-LUMO gap was independent of the structure, implying that the HOMO-LUMO gap, and therefore the red-shift in absorption, was a function of the identity of the atom

in the center and not geometric deformation induced by the substitution. This effect dominates all other Cu-induced effects for systems with 2 or fewer Cu atoms.

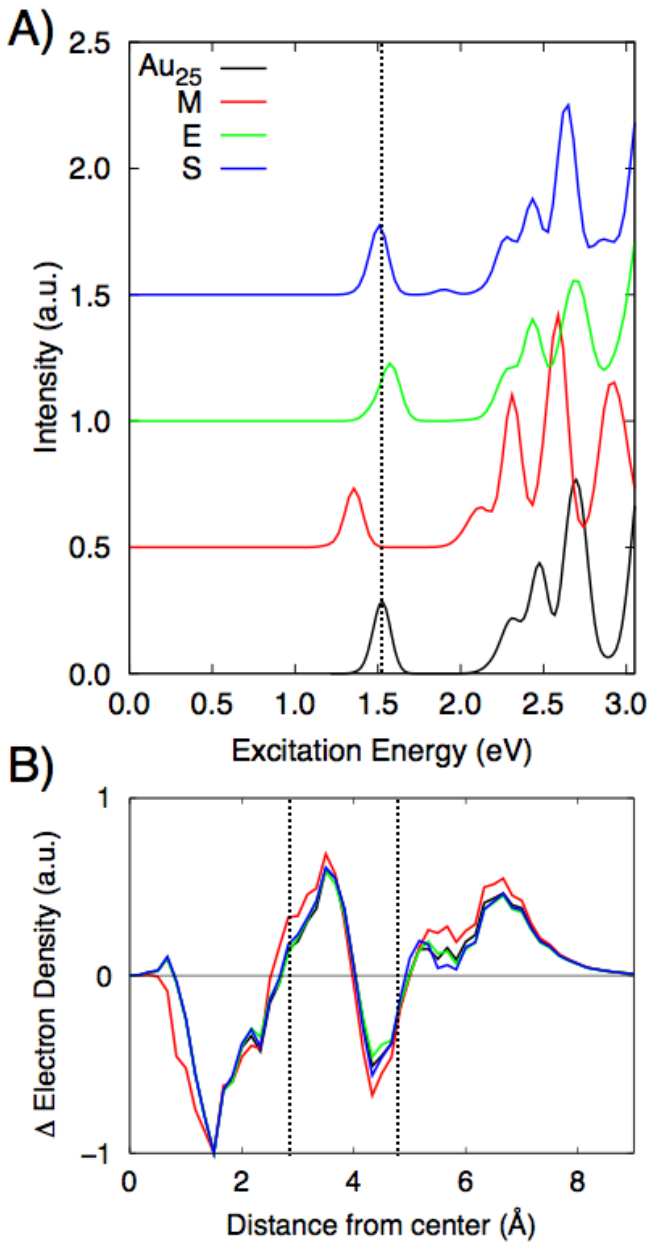

Figure 9. (A) Absorption spectrum of $[Au_{25}(SH)_{18}]^-$ and each singly substituted cluster (dashed line at HOMO-LUMO maximum absorption for visual aid). (B) Radial charge redistribution of HOMO-LUMO transition for each system (dashed lines indicated radial positions of metal atoms on the edge and staple).

2.3.3 **Middle**

When Cu is substituted for the central atom in the cluster, a significant red shift (0.2 eV for HOMO-LUMO transition) in each absorption feature is observed. Figure 9B shows the RDF of the change in electron density induced from the HOMO-LUMO transition for each monosubstituted system and the pure Au cluster, and shows the difference in transition between the $[Au_{25}(SH)_{18}]^-$ and $[Au_{24}Cu_1(SH)_{18}]^-$ (M) clusters. For the pure Au cluster, the HOMO-LUMO transition shows a well-defined shell-like structure that involves a depletion of electron density inside the Au_{13} core and near the Au atoms in the staples, and slight accumulation at the center atom, just outside the edge of the core, and at the tip of the staple. Overall, the presence of Cu on the edge or in the staple has little impact on the induced density of the HOMO-LUMO transition, however the presence of Cu in the middle qualitatively changes the behavior near the center atom. Instead of accumulation of electron density near the center atom, only depletion is observed inside the core of the cluster, and an increase of density near the edge and staple is observed.

To test whether Cu in the center is the primary factor in determining the HOMO-LUMO gap, we studied systems containing a middle Cu atom with a second Cu atom also placed in one of two positions, either the edge or staple site. Figure 10A shows the absorption spectra for each of these systems along with $[Au_{25}(SH)_{18}]^-$ for comparison. In all cases with Cu in the middle position, the reduction in HOMO-LUMO gap and induced red-shift in absorption spectrum is observed. The RDFs of induced density for the HOMO-LUMO transition are shown for each of these systems, revealing the same behavior as the system with only Cu in the middle (Figure 10B). In each case, only depletion is observed inside the core of the cluster. Isosurfaces of the LUMO orbitals elucidate the origin of the difference in electron density redistribution and are

shown in Figure 10C for the $[Au_{25}(SH)_{18}]^-$ and each system with Cu in the middle. When Cu is in the middle position, the amplitude of the LUMO near the center atom position is diminished by 64% (difference in maximum orbital amplitude near atom center), inhibiting electron density accumulation at the center during the transition.

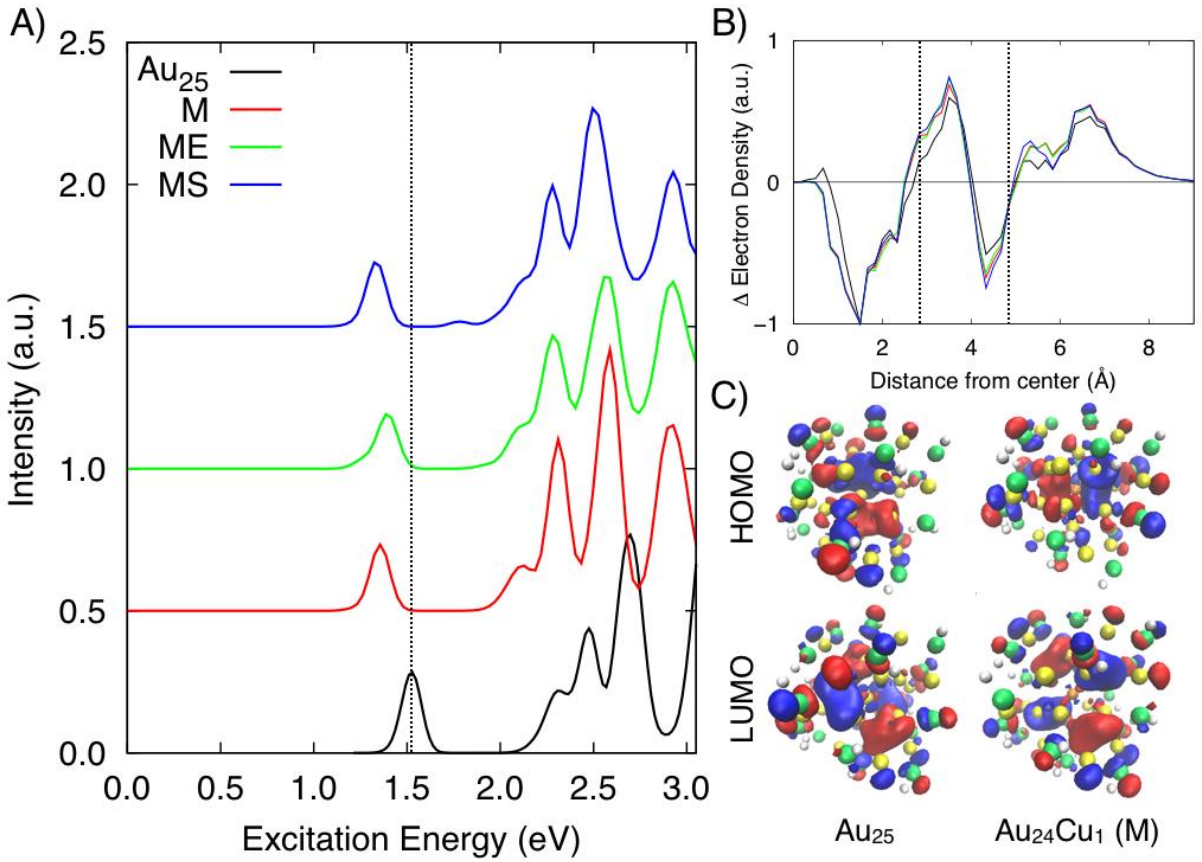

Figure 10. (A) Absorption spectrum for each system with a middle Cu atom (dashed lines indicate max absorption of HOMO-LUMO transition) (B) Radial charge redistribution induced from HOMO-LUMO transition (dashed lines indicate radial positions of metal atoms on the edge and staple) (C) Isosurface of HOMO and LUMO orbital for $[Au_{25}(SH)_{18}]^-$ and $[Au_{24}Cu_1(SH)_{18}]^-$ (M).

2.3.4 **Edge**

In addition to the monosubstituted system, three different systems with Cu on the edge were considered. Each system has a second Cu atom on the edge in one of three symmetrically unique positions relative to the first Cu atom: adjacent (adj), non-adjacent (non), and opposite (opp), as shown in the insets of Figure 11A. Together, these three systems provide a window into the correlation between relative heteroatom position and the final cluster electronic structure.

The absorption spectra of each system with Cu on the edge are compared to the pure Au cluster in Figure 11A. As the number of Cu atoms on the edge is increased from 0 to 2, the maximum absorption of the HOMO-LUMO peak is systematically blue-shifted (from 1.52 eV to 1.63 eV). While the onset of absorption also varies with Cu atom position, the magnitude is much smaller. These trends may be explained by examining the superatomic HOMO and LUMO orbital energies. Here, the HOMO and LUMO energy levels remain relatively constant, leading to only small changes in the onset of absorption. However, there is significant variation in the relative energies of the HOMO, HOMO-1 and HOMO-2 (as well as the LUMO and LUMO+1) for each of the doubly-substituted systems (as a function of both absolute Cu position as well as Cu positions with respect to one another). These variations lead to the blue-shift of the absorption maxima in the first electronic transition.

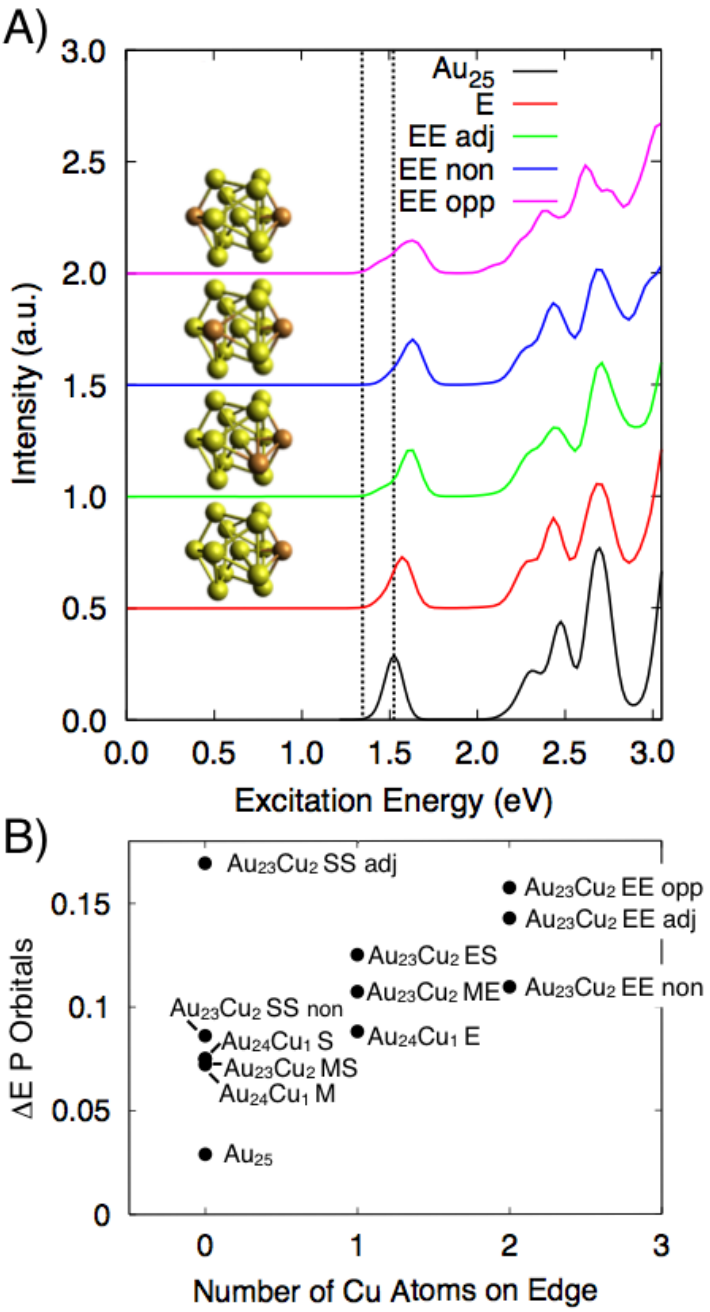

Figure 11. (A) Absorption spectra of the pure Au cluster and each system with Cu on the edge (dashed lines indicate absorption onset and max HOMO-LUMO absorption) (Inset) core structures of each edge system (B) Energy difference between 3 degenerate orbitals with P symmetry that make up the HOMO and near HOMO orbitals.

For the systems considered, ΔE (difference in energy between HOMO and HOMO-2) is a function of both the number and arrangement of Cu atoms on the edge. In the pure Au cluster, these orbitals are nearly degenerate (ΔE = 0.029 eV). However, the average energy difference between these three orbitals for systems with two Cu atoms on the edge is 0.137 eV. Not only is the degeneracy of these three orbitals dependent on the number of Cu atoms at an edge site, but also the relative positions of those Cu atoms with respect to one another (Figure 11B). For example, the energy spread for systems with two Cu atoms on the edge differ by 0.047 eV, almost double the original ΔE of these orbitals.

These calculations also highlight how the relative position of the copper atoms can change the absorption behavior, and which orbitals from the pure Au cluster respond to the presence of a heteroatom at a given position. Together, these observations provide a physical basis for how the original $[Au_{25}(SH)_{18}]^-$ degeneracy is lifted. The difference in energy for the system with a single Cu on the edge is primarily from the increase in energy of only one orbital. Specifically, this orbital has the Cu atom residing directly on the lobe of one superatom HOMO P orbital, and at the node of the other two superatom HOMO P orbitals. The position of copper relative to the HOMO P orbital lobes is responsible for determining which orbitals are affected by the presence of copper, and therefore the spread in HOMO orbital energies (Figure 12).

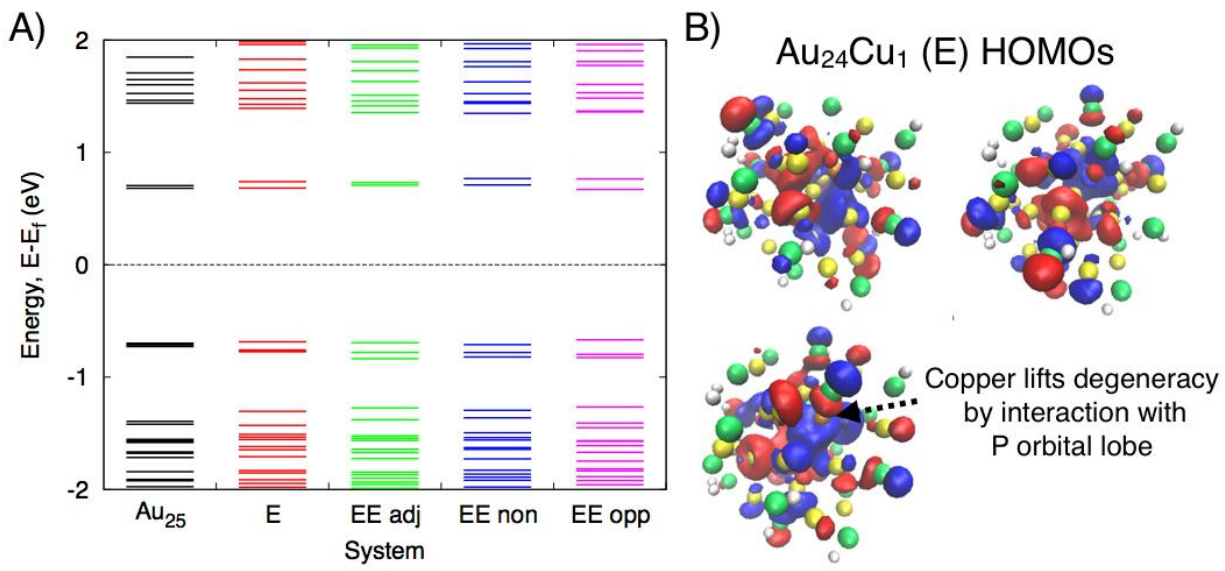

Figure 12. (A) Energy level diagram for $[Au_{25}(SR)_{18}]^-$ and each system with Cu at edge positions. (B) HOMO, HOMO-1, and HOMO-2 orbitals for $[Au_{24}Cu_1(SR)_{18}]^-$ edge system demonstrating orientation of superatomic P orbitals with respect to Cu heteroatom.

This composition and position dependent symmetry-breaking phenomenon discussed for the HOMO-LUMO transition is also observed for the higher energy peaks in the absorption spectra of these edge systems. Each transition arises from collections of near-degenerate orbitals whose degeneracies are lifted by Cu breaking various symmetries responsible for the degeneracies. This is manifested in the absorption spectra by the relative intensity and width of each absorption feature. If fewer symmetry elements exist, more individual transitions will be present, but each will be less intense, causing the absorption profile to appear broadened and have a smaller relative maximum oscillator strength than that of a system with higher symmetry.

2.3.5 **Staple**

Three systems with Cu in the staple were considered; a single substitution (each Cu is symmetrically equivalent), a double substitution in the same staple, and a double substitution in different staples, providing a probe of the effect of substitution on the relative Cu position within the staples. The absorption spectra of each staple system along with $[Au_{25}(SH)_{18}]^-$ are shown in Figure 13A. There is a small red-shift (0.015 eV per Cu atom) in the maximum absorption wavelength of the HOMO-LUMO transition. This red-shift is due to a slight lowering of the LUMO energy that can be seen in Figure 13B. The degeneracy in the superatom HOMO orbitals is also affected by each arrangement of Cu atoms in the staple, this effect seems to be unique for each system considered.

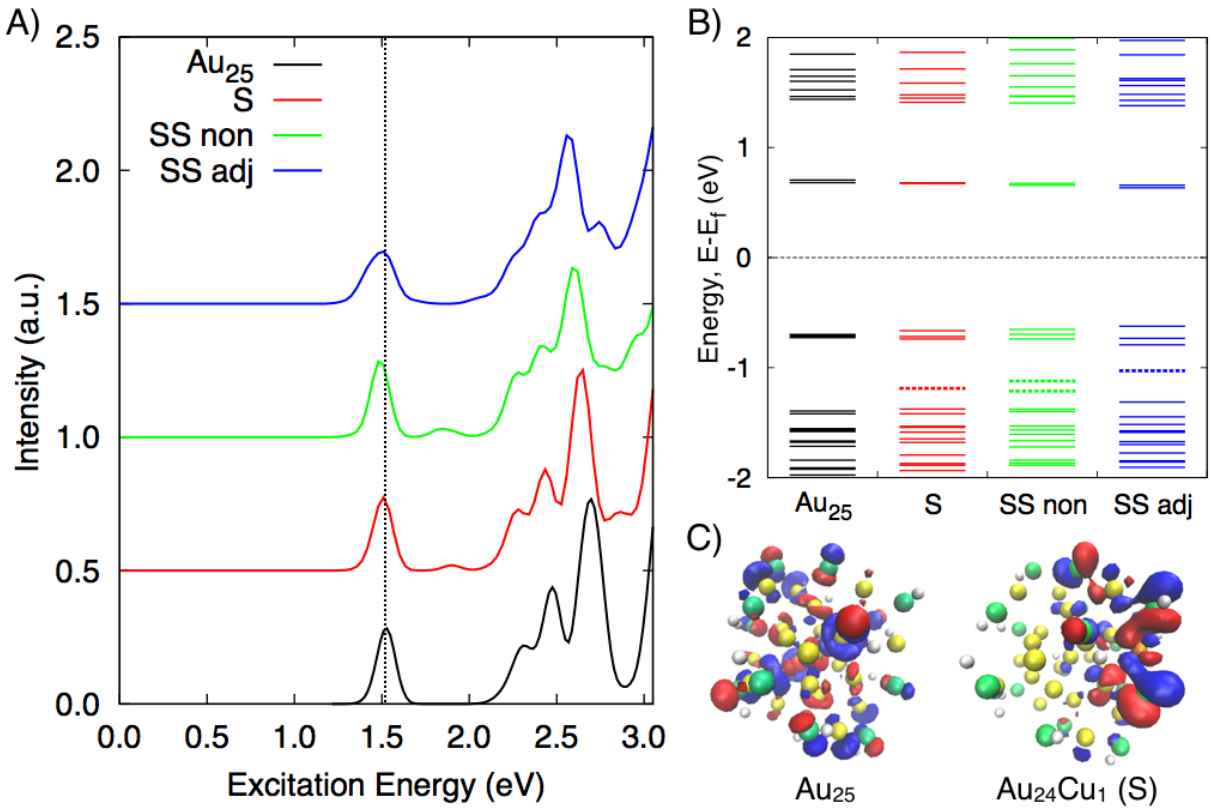

Figure 13. (A) Absorption spectra of the pure Au cluster and each system with Cu in the staple (dashed lines indicate HOMO-LUMO max absorption (B) Energy level diagram for each staple system showing the emergence of new energy levels (dashed lines) (C) Orbital isosurface of the HOMO-3 for $[Au_{25}(SH)_{18}]^-$ and $[Au_{24}Cu(SH)_{18}]^-$ (S) clusters.

Apart from a relatively small impact on the HOMO-LUMO transition, Cu in the staple also has an impact on a set of nearly degenerate orbitals below the HOMO orbital energy, namely the HOMO-3 and HOMO-4. The isosurface of the HOMO-3 for the pure Au cluster and the $[Au_{24}Cu_1(SH)_{18}]^-$ (S) cluster are shown in Figure 13C. The HOMO-3 orbital in the pure gold cluster is delocalized across a number of staples in a regular bonding/antibonding pattern, and consists of atomic Au d and sulfur p orbitals. Each of these degenerate orbitals in the $[Au_{25}(SH)_{18}]^-$ cluster has a similar character, the difference resulting from which staples are participating.

The inclusion of Cu in one of the staples completely changes the spatial arrangement of the aforementioned orbital by localizing it near the Cu atom, while maintaining the same underlying atomic orbital character. The most striking impact of the new orbital arrangement is the 0.2 eV destabilization in orbital energy that lifts the original degeneracy. In this case, lifting the degeneracy results in moving the orbital energy into a gap in the electronic structure, similar to a defect state in doped semiconductors.[105] This new state causes a new feature to arise in the absorption spectrum (Figure 13A), that is not present in $[Au_{25}(SH)_{18}]^-$. This peak involves absorption from the new, destabilized orbital to the degenerate LUMO set of orbitals.

Adding a second Cu to the same staple further increases the energy of this newly destabilized orbital. Therefore, the new peak is red-shifted and appears on the high-energy edge of the HOMO-LUMO transition feature, resulting in an apparent broadening of this peak. When a second Cu atom is spatially isolated in a different staple, it has the same effect as the first substituent atom, but this time on a different orbital. These two new orbitals effectively create a new degeneracy that is closer to the Fermi level, making the Cu induced absorption feature more intense due to a second contributing resonance. In summary, adding each Cu atom to a staple has

some well-defined effect. This impact is either additive when the Cu atoms are contained in the same staple motif, or two individual effects when the Cu atoms are spatially isolated in different staples.

2.4 **Discussion**

One of the most striking atomic property differences between Au and Cu is the difference in electronegativity. Due to relativistic effects,[106] Au has the highest Pauling electronegativity of all transitions metals, with a value of 2.54. The electronegativity of Cu is 1.90 on the same scale, leading to polar Au-Cu bonds, and therefore partial charges, in the systems containing both elements. This situation can be compared to the ground state electron distribution in classic organic systems containing heteroatoms. For example, in a 1971 paper, Roald Hoffmann describes how electronegativity can be used to modulate the energy level structure in organic molecules, specifically the frontier orbitals.[107] Using the HOMO and LUMO orbitals of an azulene molecule, Hoffmann describes that adding a more electronegative atom, like nitrogen, to a region of high electron density will have a stabilizing effect for a given orbital. This general principle is often used in designing molecules in the fields of organic and molecular electronics.[108,109] Our current data suggest that the stabilizing effect of electronegative elements in electron dense regions of a molecule, may have an analogy in the electronic structure of mixed metal cluster systems such as those considered here.

For example, we can consider the HOMO and LUMO electron distribution induced by Cu substitution in the $[Au_{25}(SH)_{18}]^-$ clusters. Here, the HOMO exhibits a large amplitude near the center of the cluster, while the LUMO is more centered on the edge of the cluster.

Substituting the less electronegative Cu atom in the center will therefore destabilize orbitals with density primarily at the center, such as the HOMO, and stabilize other orbitals, like the LUMO. These changes in orbital energies would result in a decrease in the overall HOMO-LUMO gap, as is observed when Cu is substituted in the middle of the cluster. The same effect can be seen when Cu is on the edge, but here, symmetry begins to play a dominant role in the observed properties. The frontier orbital isosurfaces for Cu atom substitutions on the edge or staple is in a region with a non-zero amplitude for only one of the three HOMO orbitals. In two of the HOMO orbitals, the Cu atom is positioned at a node, but since the P orbitals together are spherically symmetric; the third P orbital must have Cu at the tip of its lobe. This orbital is higher energy due to electronegativity (*vide supra*), and therefore the orbital is responsible for the lifting of degeneracy. This same symmetry induced splitting can be seen in the LUMO orbitals as well, forcing the HOMO-LUMO peak to broaden, further increasing the symmetry-breaking induced broadening. Finally, the influence of Cu atom geometric position on the HOMO and LUMO orbital splitting patterns explains how the various arrangements of Cu on the edge result in several different peak widths and peak shapes, while maintaining a similar onset of absorption. In other words, each symmetry will produce a different orbital pattern, causing each of their HOMO-LUMO peaks to have a distinct shape.

A previous report, using Ag as a heteroatom, also studied the impact of substitution on the electronic structure of $[Au_{25}(SH)_{18}]^-$ as a function of position.[89] Here, the authors considered substitution at the middle, edge, and staple. Because silver's electronegativity (1.93) is very close to that of copper (1.90), it provides a good test for our hypothesis that electronegativity is the driving force for these electronic structure changes. In the work by Guidez et al., single Ag substitution showed a similar 0.20 eV closing of the HOMO-LUMO gap when Ag is in the

middle. They found the most stable position for Ag substitution was on the edge of the cluster, and demonstrated that various Ag arrangements on the edge produced a variety of HOMO-LUMO transition peak shapes. Each of these observations is consistent with our hypothesis that electronegativity and symmetry are driving the observed electronic features.

The orbital localization observed when Cu is placed in the staple is different from the previously discussed behaviors largely due to the staple being removed from the high electron density regions of the HOMO and LUMO that primarily exist in the core. If electronegativity is driving the differences in optical behavior at other Cu positions, we hypothesized that it would also control the electronic structure when a Cu atom was substituted in a staple site. In order to test how electronegativity impacts the electronic structure in a structurally analogous small molecule system, we modeled a crown ether molecule, 12-crown-4 (structures in Figure 14). The ring geometry of the crown ether may be used to mimic a geometry similar to the one formed by the staples in $[Au_{25}(SH)_{18}]^-$. The oxygen positions in 12-crown-4 provide a place to substitute a less electronegative heteroatom, such as sulfur, conserving a geometry and chemistry that can be observed experimentally.[110]

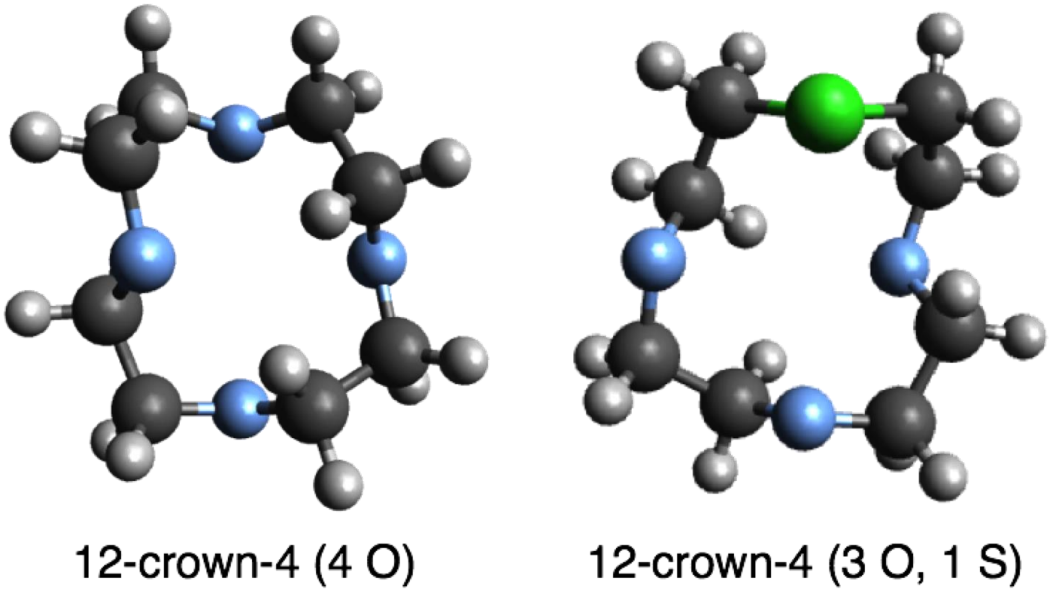

Figure 14. Structures of two crown ether molecules considered, 12-crown-4 with 4 oxygen atoms and a structure with a sulfur substitution at one of the original oxygen positions. Cyan, oxygen; green, sulfur; gray, carbon; white, hydrogen.

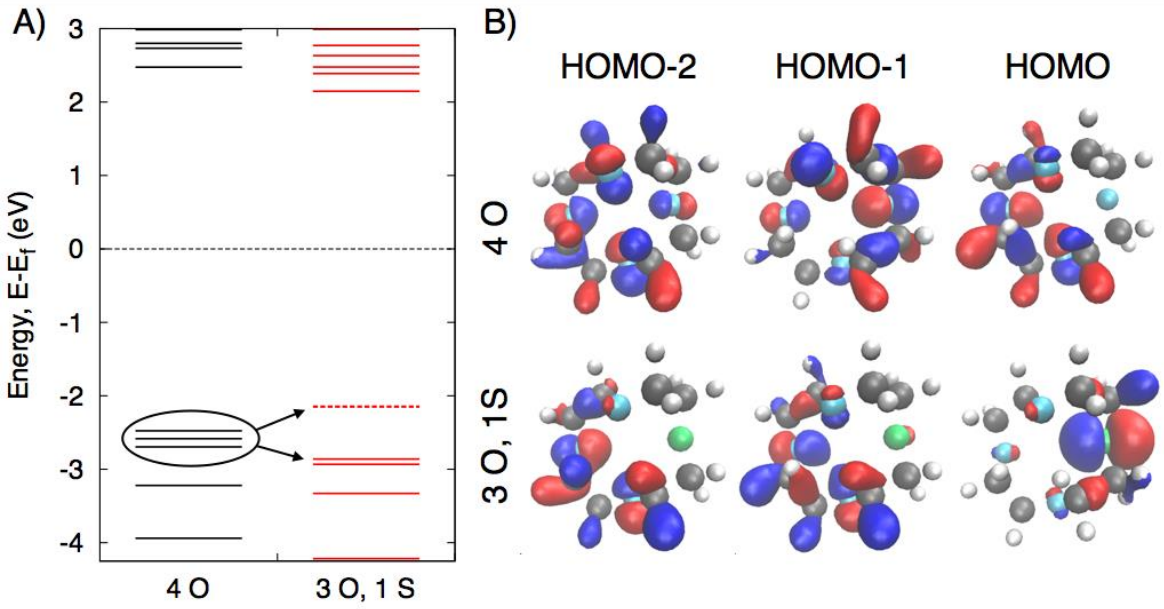

Figure 15. (A) Energy level diagram and (B) HOMO-HOMO-2 orbital isosurface for 12-crown-4 with 4 oxygen atoms and 3 oxygen and one sulfur atom. Cyan, oxygen; green, sulfur; gray, carbon; white, hydrogen.

The three highest energy occupied orbitals in 12-crown-4 are nearly degenerate, have the same bonding character, and are delocalized over a portion of the structure. This is similar to the HOMO-3 and HOMO-4 orbitals in $[Au_{25}(SH)_{18}]^-$, which are the orbitals Cu influences when placed in the staple of the cluster. When sulfur replaces one of the oxygen atoms in 12-crown-4, the degeneracy of these orbitals is lifted and the resulting orbital is localized at the electronegative substitution site, as shown in Figure 15B. In both the 12-crown-4 and $[Au_{25}(SH)_{18}]^-$ systems the impurity changes the ground state electron distribution and destabilizes a single, specific orbital that is localized at the impurity. These perturbations create a new energy level structure, and in the case of the $[Au_{25}(SH)_{18}]^-$ cluster, they result in the creation of energy levels between the HOMO-2 and HOMO-3 of the original cluster. The introduction of these states results in an entirely new absorption feature in the cluster absorption spectrum – a potentially important spectroscopic signature.

2.5 **Conclusion**

The changes in electronic properties induced by introducing Cu to a Au nanocluster can be summarized within two main descriptors, namely symmetry and electronegativity. When Cu is placed in the middle of the cluster, no symmetry elements are broken and therefore no symmetry-induced effects are observed. However, there is a large effect on the HOMO-LUMO gap as a result of electronegativity. With Cu on the edge or in the staple, the effect of symmetry becomes important. Breaking symmetries can have a dramatic impact, including changing the energy spacing of a group of initially degenerate orbitals, as seen when Cu is on the edge, to a redistribution of the systems energy levels. Both of these effects can introduce defect states in

previously empty regions of energy space. However, the impact of electronegativity remains important in determining the nature of each induced effect. Taken together, symmetry and electronegativity can be used as design principles to tailor the electronic structure of a metal nanocluster, and provide incentive to gain better structural control in mixed-metal nanoparticle synthesis.

3.0 Copper Induces a Core Plasmon in Intermetallic $Au_{(144,145)-x}Cu_x(SR)_{60}$ Nanoclusters

(Portions of this work were published previously and are reprinted with permission from Malola, S.; Hartmann, M. J.; Häkkinen, H. *J. Phys. Chem. Lett.* **2015**, 515-520. Copyright 2015 American Chemical Society.)

3.1 **Introduction**

Nanometer-scale, ligand-stabilized gold nanoclusters have emerged as a novel form of nanoscale matter with potential applications in molecular electronics, optics, sensing, drug delivery, and biolabeling.[111-115] Tremendous advances have been achieved in understanding their stability and structure due to contributions from synthetic work, X-ray crystallography, and density functional theory computations.[28, 53, 116-121] Aside from pure gold nanoclusters stabilized by metal-ligand surface chemistry, recent work has started to explore the properties of intermetallic clusters, where gold is the host material doped by silver, copper, palladium, or platinum.[4, 43-44, 48, 122-135] The use of gold and thiols is not only beneficial to protect the easier-oxidized metals in intermetallic compounds, but the presence of even small amounts of the other metals has been shown to modify the electronic structure of the particle as a whole, demonstrated by clear chances in the catalytic activity, optical absorption and photoluminescence. Understanding how inclusion of other metal in gold clusters affects the electronic structure and

optical properties is crucial to better engineer these novel nanomaterials. Considering these bimetallic systems in the presence of a stabilizing ligand layer is particularly important because ligands are known to modify the cluster electronic structure with respect to their ligand-less bimetallic nanocluster counterparts, opening up potential for new properties from the synergistic combination of surface chemistry and metal composition.[136]

Recently, the Dass group has reported a strong enhancement of optical absorption of copper-doped $Au_{144-x}Cu_x(SR)_{60}$ clusters, which differs dramatically from the behavior of corresponding silver-doped clusters.[48] With $8 \leq x \leq 25$, a strong, plasmonic-like absorption develops around 520 nm, while mixing of silver into $Au_{144}(SR)_{60}$ creates multiple peaks in the visible range.[127] We have previously[128-129] studied the electronic structure and optical properties of $Au_{144-x}Au_x(SR)_{60}$ ($X \leq 60$) nanoclusters and will concentrate here on a detailed study of how copper doping in $Au_{144}(SR)_{60}$ changes the electronic structure and optical absorption. We find that copper behaves drastically different from silver and will show that the enhancement of absorption in the range of 500-600 nm is dominantly caused by interband effects due to alignment of Cu(3d) and Au(5d) band edges. To the best of our knowledge, this is the first detailed computational study of intermetallic thiol-stabilized gold-copper clusters in the size range where the clusters' properties are at the border between "molecular" and "metallic" regimes.

We considered several plausible cluster models for $Au_{(144,145)-x}Cu_x(SR)_{60}$ with the same overall geometry, based on the structure proposed first for $Au_{144}(SR)_{60}$ by Lopez-Acevedo et al. in 2009.[137] Although the precise structures of these compounds are still not known from experiments, our precious work has shown that the computed X-ray powder diffraction function, optical absorption, and electrochemical properties of the model cluster $Au_{144}(SR)_{60}$ are in very

good agreement with experimental data for organo-soluble clusters $Au_{144-146}(SR)_{59-60}$.[34, 138-145] Our model has an icosahedral-based 114/115-atom metal core built out of two Mackay shells (M1, 12 sites and M2, 42 sites) and one anti-Mackay (AM, 60 sites) shell. Depending on whether the atom site at the origin is filled or not, the core has 115 or 114 atoms, respectively. Additionally, the core is protected by 30 RS-Au-SR units. This "divide and protect" geometrical motif[146] is frequently found in the structurally defined thiolate-protected gold nanoclusters as well as in thiolate monolayers on gold surface.[53] Placement of the 30 RS-Au-SR units on the core is chiral, which also induces a slight chiral distortion to the 60-atom AM surface layer of the core. Since we focus the analysis on the metal core, the chemical groups (SR) of the ligand layer were modeled by simple SH groups. Others[147] have recently studied variants of this geometry, which differ from the original model[137] only by organization of the relative orientations of the RS groups in the RS-Au-SR motifs with respect to the approximately linear S-Au-S axis (this creates conformers similar to the anti/syn conformers in alkane stereochemistry).

3.2 **Computational Methods**

We used density functional theory (DFT) with projector augmented waves (PAW) as implemented in the real-space grid code, the grid projector augmented wave (GPAW) program package[148-149] to study the ground state electronic structure and optical absorption of clusters 1-10 and the all-gold $Au_{144}(SH)_{60}$ as reference. A simple SH ligand was used in place for the thiolates (SR = SH). For the PAW setup, the atomic valence was defined as $Au(4d^{10}6s^1)$, $Cu(3d^{10}4s^1)$, $S(3s^23p^2)$, and $H(1s^1)$, with scalar-relativistic effects included for Au and Cu. Optimization of the clusters were preformed without a symmetry constraint, with grid spacing of

0.2 Å, and until the residual forces were below 0.05 eV/Å. The local density approximation (LDA)[78] was used for the structural optimizations, based on the previous experience that LDA reproduces the experimental metal-metal distances better than the GGA-based functionals. Angular momentum resolved projected density of states analysis of the ground state "superatom orbitals" was performed by projection of the Kohn-Sham orbitals to the center of mass of the structures in a sphere with radius of 7.7 Å.[28] A similar atom-centered analysis in spheres of 1.4 A radius was done in order to locate the metal d and sp bands. Distribution of charge in the metal core was analyzed by using the Bader method.[150] Optical spectra were calculated with linear response time-dependent density functional theory (LR-TDDFT), as implemented in the GPAW package,[151] and the PBE-GGA functional for the exchange-correlation kernel[152] and a grid spacing of 0.25 Å were used. The nature of the optical transitions was analyzed at selected excitation energies by examining contributions of particle-hole excitations to a given peak (the transition contribution map, TCM) and visualizing induced densities using our recently published method based on time-dependent density functional perturbation theory (TD-DFPT).[31] Formation energy (E_{form}) of the clusters 1 – 10 was evaluated from the stoichiometric formula:

$$E_{form} = \frac{E\left[Au_x Cu_y (SH)_{60}\right] + 30E[H_2] - xE_{Au,fcc} - yE_{Cu,fcc} - 60E[SH_2]}{x + y}$$

Where $E_{Au,fcc}$ and $E_{Cu,fcc}$ are the energies per metal atom in the respective optimized fcc bulk structure and all energies are calculated from the LDA approximation.

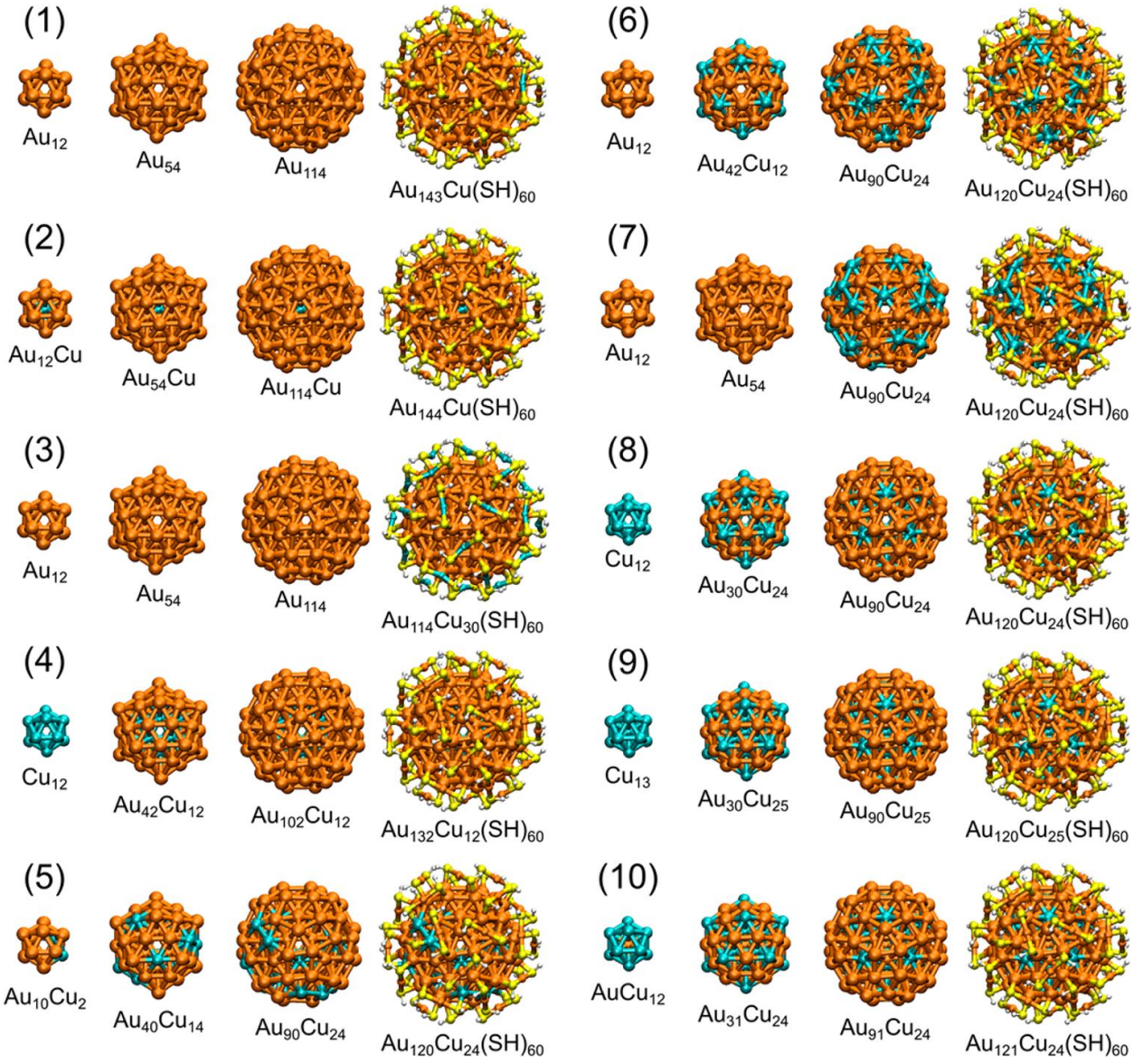

Figure 16. Model structures 1-10 used in the calculations. Orange, gold; blue, copper; yellow, sulfur; white, hydrogen.

Table 5. Occupation of the Mackay (M1, 12 sites and M2, 42 sites) and Anti-Mackay (AM, 60 sites) shells of the 114/115-atom metal core in clusters 1 to 10.[a]

Cluster	Origin	M1/12	M2/42	AM/60	Composition	# Metal
1	0	Au_{12}	Au_{42}	Au_{60}	$Au_{143}Cu(SH)_{60}$	144
2	Cu	Au_{12}	Au_{42}	Au_{60}	$Au_{144}Cu(SH)_{60}$	145
3	0	Au_{12}	Au_{42}	Au_{60}	$Au_{114}Cu_{30}(SH)_{60}$	144
4	0	Cu_{12}	Au_{42}	Au_{60}	$Au_{132}Cu_{12}(SH)_{60}$	144
5	0	$Au_{10}Cu_2$	$Au_{30}Cu_{12}$	$Au_{50}Cu_{10}$	$Au_{120}Cu_{24}(SH)_{60}$	144
6	0	Au_{12}	$Au_{30}Cu_{12}$	$Au_{50}Cu_{10}$	$Au_{120}Cu_{24}(SH)_{60}$	144
7	0	Au_{12}	Au_{42}	$Au_{36}Cu_{24}$	$Au_{120}Cu_{24}(SH)_{60}$	144
8	0	Cu_{12}	$Au_{30}Cu_{12}$	Au_{60}	$Au_{120}Cu_{24}(SH)_{60}$	144
9	Cu	Cu_{12}	$Au_{30}Cu_{12}$	Au_{60}	$Au_{120}Cu_{25}(SH)_{60}$	145
10	Au	Cu_{12}	$Au_{30}Cu_{12}$	Au_{60}	$Au_{121}Cu_{24}(SH)_{60}$	145

[a]The center position is denoted by "origin." All cores are protected by the same (HS-metal-SH)60 ligand shell, giving the total count of the metal atoms 144 or 145.

Ten structures were considered (structures shown in Figure 16 and described in Table 5, labeled 1-10), where the number of metal atoms is either 144 (clusters 1, 3-8) or 145 (clusters 2, 9, 10) and the number of copper atoms is between 1 and 30. We created structures where the dopants are placed symmetrically (2, 4, 8-10) or asymmetrically/"randomly" (5-7) over the various shells in the metal core as well as two cases where Cu is in the ligand shell (1, 3). All clusters were relaxed to a local energy minimum and their electronic structure and optical absorption was computed and analyzed using linear response time dependent density functional theory (LR-TDDFT) and time dependent density functional perturbation theory (TD-DFPT) (see details in the Computational Methods section).

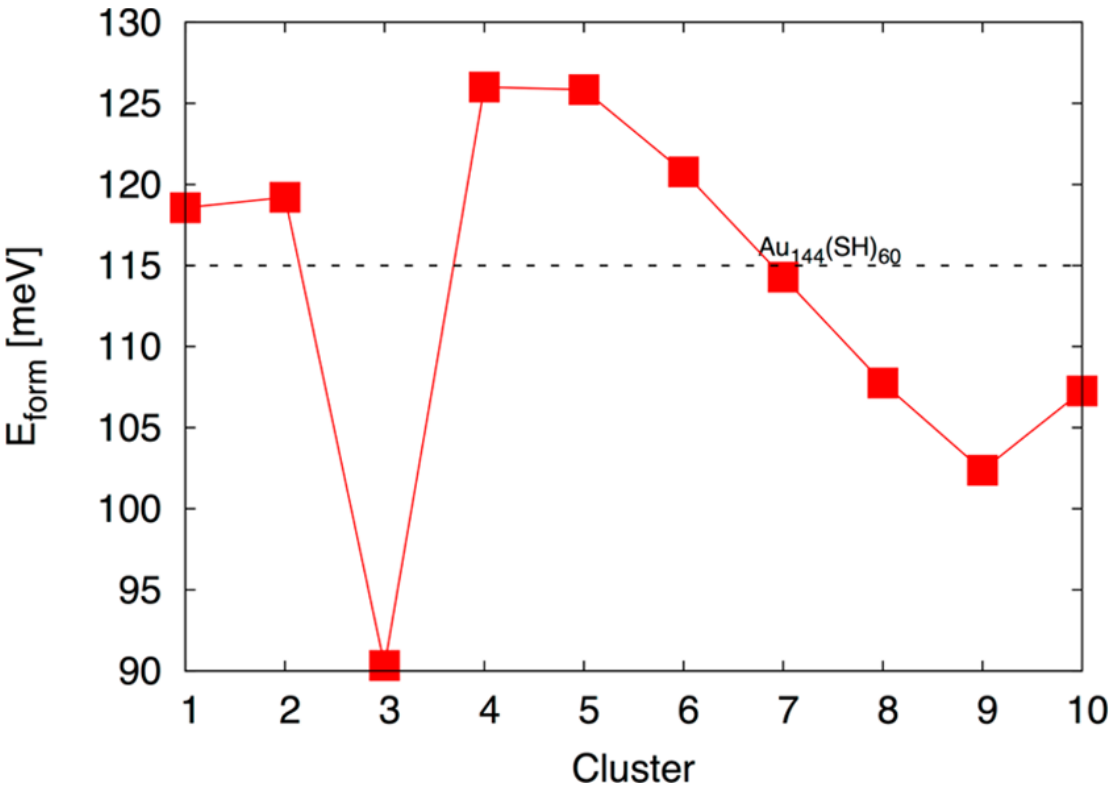

Figure 17. Formation energies per metal atom (Eform) of 1-10. For reference, the formation energy of all-gold $Au_{144}(SH)_{60}$ is 115 meV/metal atom (dotted horizontal line).

Table 6. Local Bader charges in (in e) of atomic shells for clusters: $Au_{144}(SH)_{60}$, (2) $Au_{144}Cu(SH)_{60}$, (3) $Au_{114}Cu_{30}(SH)_{60}$, and (9) $Au_{120}Cu_{25}(SH)_{60}$. O denotes the site at the origin, M1 and M2 are the Mackay shells, AM is the anti-Mackay shell, and L is the $(HS\text{-}metal\text{-}SH)_{30}$ ligand shell.

		ref	ref	ref	2	2	2	3	3	3	9	9	9
		Tot Q	Q/N	N	Tot Q	Q/N	N	Tot Q	Q/N	N	Tot Q	Q/N	N
Cu	O	-	-	-	0.336	0.336	1	-	-	-	-0.029	-0.029	1
Au	M1	-0.442	-0.037	12	-0.671	-0.056	12	-0.470	-0.039	12	-	-	-
Cu	M1	-	-	-	-	-	-	-	-	-	1.993	0.166	12
Au	M2	-0.271	-0.0065	42	-0.601	-0.014	42	-0.830	-0.020	42	-4.317	-0.144	30
Cu	M2	-	-	-	-	-	-	-	-	-	4.118	0.343	12
Au	M3	4.136	0.069	60	3.816	0.064	60	1.0731	0.018	60	1.482	0.025	60
Au	L	3.195	0.11	30	3.052	0.102	30	-	-	-	3.029	0.101	30
Cu	L	-	-	-	-	-	-	12.842	0.428	30	-	-	-
SH	L	-6.699	-0.11	60	-5.974	-0.100	60	-12.651	-0.211	60	-6.312	-0.105	60

Figure 17 shows the calculated formation energies (E_{form}) for each structure. All formation energies are positive meaning that there is an energy penalty to form the clusters with respect to the bulk reservoirs (SH_2 and the fcc bulk phase of the metals; see the formula for E_{form} in the Computational Methods section). The reference value for E_{form} is 115 meV per metal atom for the all-gold $Au_{144}(SH)_{60}$. Two interesting minima of E_{form} are observed, for clusters 3 and 9, corresponding to 30 Cu atoms in the ligand shell (3) and 25 Cu atoms at the center of the core (9). We defer the discussion of the including of Cu in the ligand shell to the end of the paper and discuss the other systems first. Cluster 9 has the composition $Au_{120}Cu_{25}(SH)_{60}$, comprising a Cu atom at the origin, 12 Cu atoms in the M1 shell, and 12 Cu atoms in the M2 shell in symmetric positions with respect to M1 (formatting the 12 icosahedral vertices of M2). In all the cases, the bonding between copper and gold involves a clear transfer of electron charge to the more

electronegative gold atoms (see Table 6 of atomic Bader charges for clusters 2, 3, and 9). It is very interesting to note that a simple change, trading a copper atom to a gold atom at the origin in cluster 10 of composition $Au_{121}Cu_{24}(SH)_{60}$ affects the energetics appreciably, i.e., making 10 less favorable that 9 by about 5 meV per metal atom or 0.725 eV per cluster. Our results clearly predict that (i) since the formation energy of 7-10 is smaller than the referece (115 meV per metal atom), it is possible for gold-copper metal mixing to be formed by a thermodynamic driving force in $Au_{144}(SH)_{60}$ clusters (ii) the preferable doping positions for copper are symmetric within the inner core. This is contrary to our earlier theoretical finding for similar intermetallic gold-silver $Au_{144-x}Ag_x(SH)_{60}$ (x = 30, 60) where the optimal positions for silver were found to be in the 60-atom AM shell at the surface of the metal core.[129]

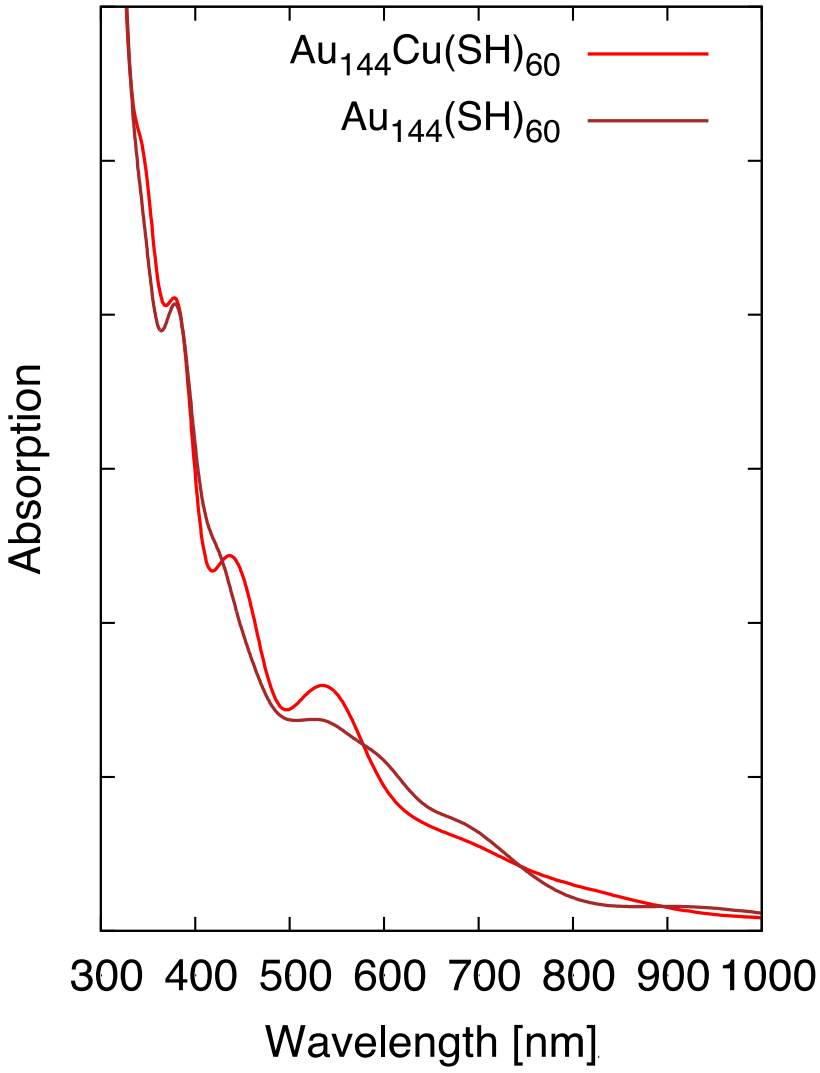

Figure 18. Optical absorption spectra of $Au_{144}(SH)_{60}$ and (2) $Au_{144}Cu(SH)_{60}$.

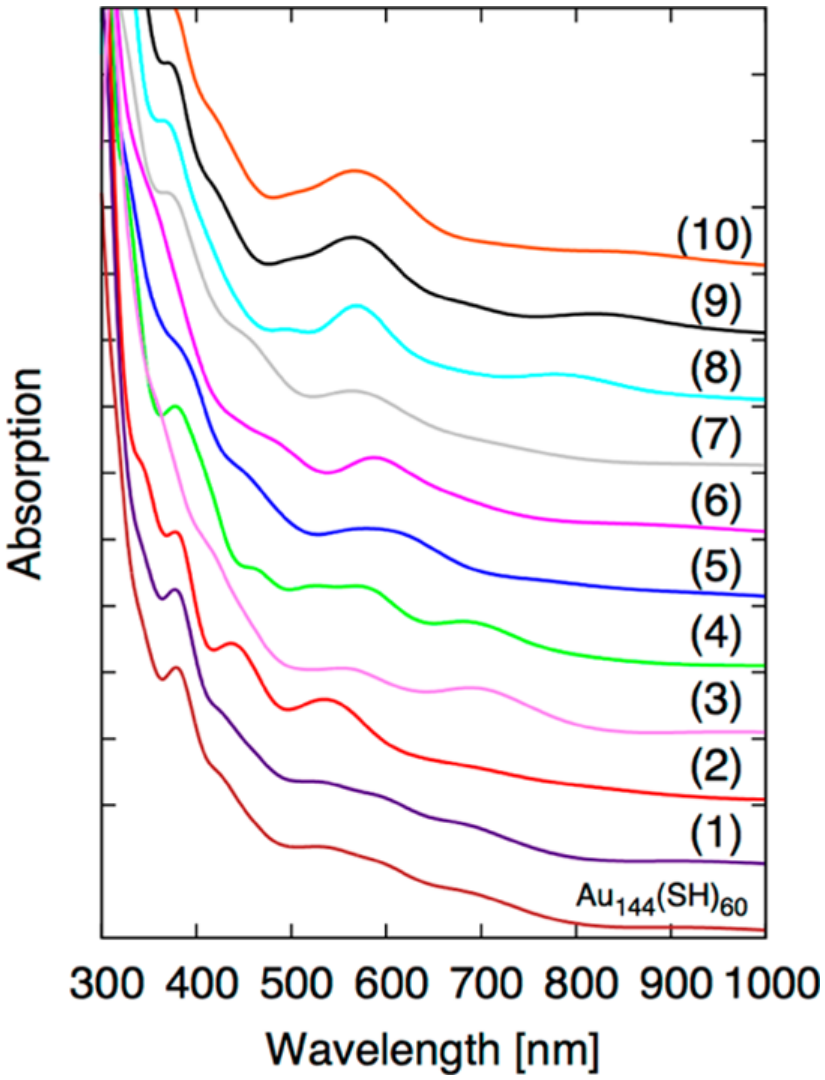

Figure 19. Computed optical absorption spectra of 1-10 as compared to the all-gold $Au_{144}(SR)_{60}$ cluster. The individual transitions are broadened by a Gaussian of 0.1 eV width.

Even the simplest possible addition (copper atom in the central vacancy of $Au_{144}(SH)_{60}$) increases the oscillator strength of transitions in the Au_{144} spectrum at around 540 nm, 440, and 380 nm (Figure 18). In addition, figure 19 shows the computed absorption spectra of each structure and compares them to the spectrum for $Au_{144}(SH)_{60}$,[31] demonstrating that the inclusion of copper changes the absorption features dramatically. Spectra of 8, 9, and 10 display a single, broad, and strong feature peaking at about 560-570 nm. These clusters have 24 to 25 copper atoms in symmetric positions in the inner core (M1 and M2 shells, and at origin, see Table 5) and are also energetically favorable ones (Figure 17). The enhanced absorption peak around 560-570 nm of 8, 9, and 10 agrees qualitatively very well with the recent observation from Dass group, who reported a formation of a "plasmon-like" absorption peak around 520 nm in intermetallic $Au_{144-x}Cu_x(SR)_{60}$ clusters, where $x \leq 23$.[48]

It is well-known that due to relativistic effects, the electronic structure (particularly the s-d gap) of a single gold atom is closer to copper atom than that of silver.[153] In the bulk phase, the upper edge of the Cu(3d) and Au(5d) bands are about 2.0 and 2.4 eV from the Fermi surface, respectively, as compared to 3.7 eV for silver.[154-156] This band edge alignment results in a strong modification of the frequency-dependent dielectric function due to d → sp interband transitions in copper and gold in the visible range (providing the color of the material) as contrast to silver where the d → sp transition is in the ultraviolet region.[114] We analyzed the metal s-, p-, and d-states by projection of the Kohn-Sham orbitals onto spherical harmonics in local atomic spheres, and the result is shown in Figure 20 for the minimal-doped (2) and maximal-doped (9) clusters. The 3d states of a single copper atom appear in a very narrow energy region around -1.4 eV in 1, slightly off from the band edge of Au(5d) states. These states broaden into a band that aligns

almost perfectly with the Au(5d) band in 9, where the upper edges of Cu(3d) and Au(5d) are both at -1.6 eV.

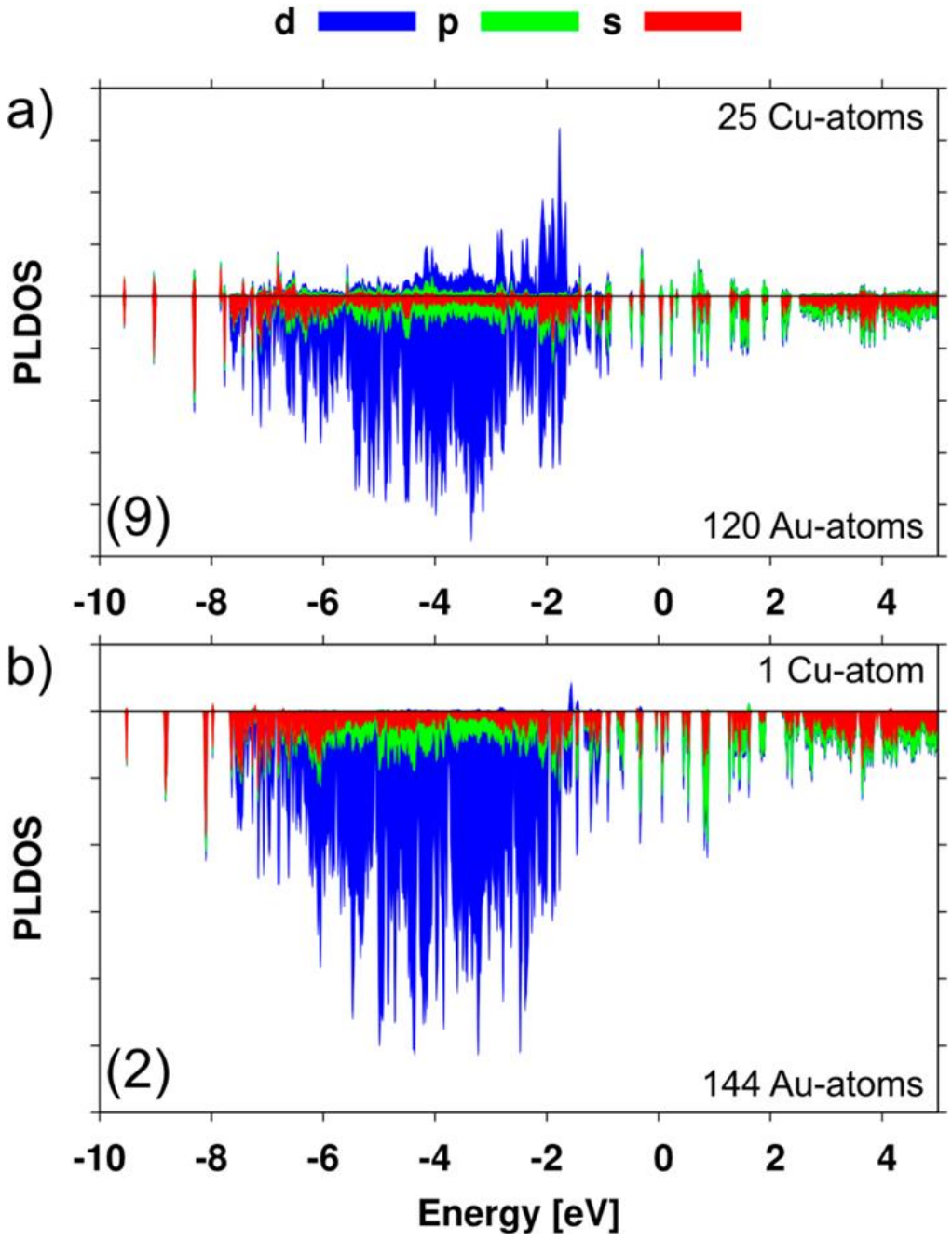

Figure 20. Decomposition of metal states to d and sp bands for (A) cluster 9 and (B) cluster 2. The energy axis is referenced to the Fermi energy at zero.

Figures 21 and 22 show the analysis of the 535 nm absorption for cluster 2 and 564 nm for cluster 9 respectively, and shows their respective induced densities and transition contribution maps (TCM).[31] Visualization of the induced electron density at these excitation energies of the corresponding clusters shows a collective dipole-like oscillation in the whole volume of the cluster, which the Au(5d)/Cu(3d) electrons oscillating in the opposite phase to the Au(6sp)/Cu(4sp) electrons. Previously we termed this kind of excitation as a "core plasmon" for $Au_{144}(SH)_{60}$. The TCM maps reveal that these excitations involve significant contribution from both intraband (sp to sp) and interband (d to sp) components. A crucial difference between the $Au_{(144,145)-x}Cu_x(SH)_{60}$ clusters studied here and the $Au_{144-x}Ag_x(SH)_{60}$ studied by us before[128] is the fact that the Ag(4d) band does not align with Au(5d), limited the ability of $Au_{144-x}Ag_x(SH)_{60}$ conjugates to undergo a strong enhancement from interband absorption. Indeed, the experimental absorption spectra of $Au_{144-x}Ag_x(SH)_{60}$ from the Dass group showed multiple peaks instead of a single strong peak, as the silver content is increased.[127]

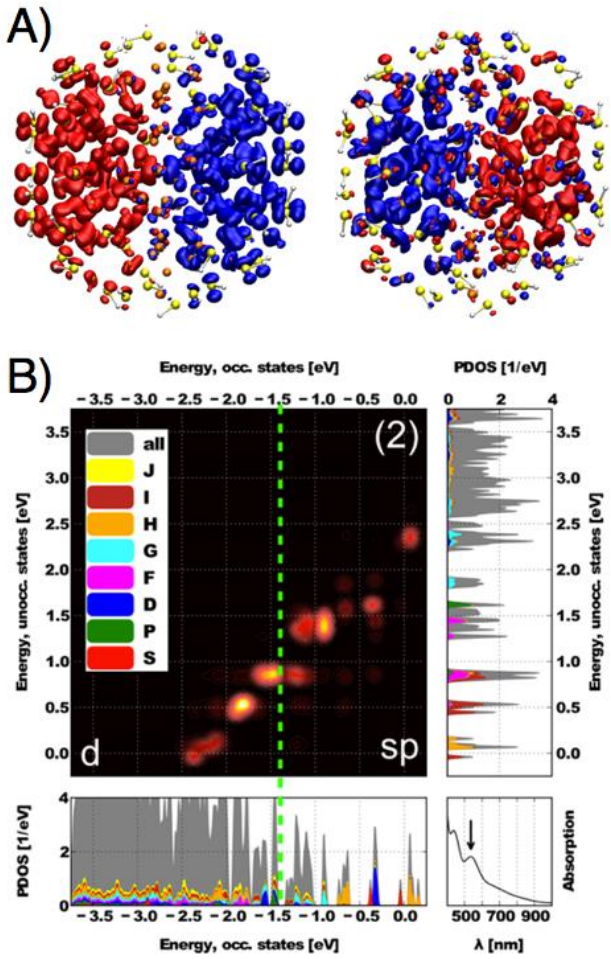

Figure 21. (A) Induced densities for cluster 2 at wavelength of 535 nm. The sp/ligand and d-contributions are visualized separately and the classification is based on the location of the hole states (initially occupied single-electron states). Note the collective dipole-like density oscillation and the opposite phase in oscillations of d-electrons to that of the sp/ligand visualizing a screening effect. (B) TCM analysis of optical transitions for cluster 2 at wavelength of 535 nm. The electronic state contributions to absorption arising from the Au(5d)/Cu(3d)-bands and ligand/Au(6sp)/Cu(4sp)-bands are divided by the vertical dotted lines. Angular momentum projected electronic density of states (vertical in each subfigure. The brighter the yellow area in the correlation plot, the stronger the contribution from this region of occupied to unoccupied single-electron contribution in the transition (Fermi energy is referenced to zero).

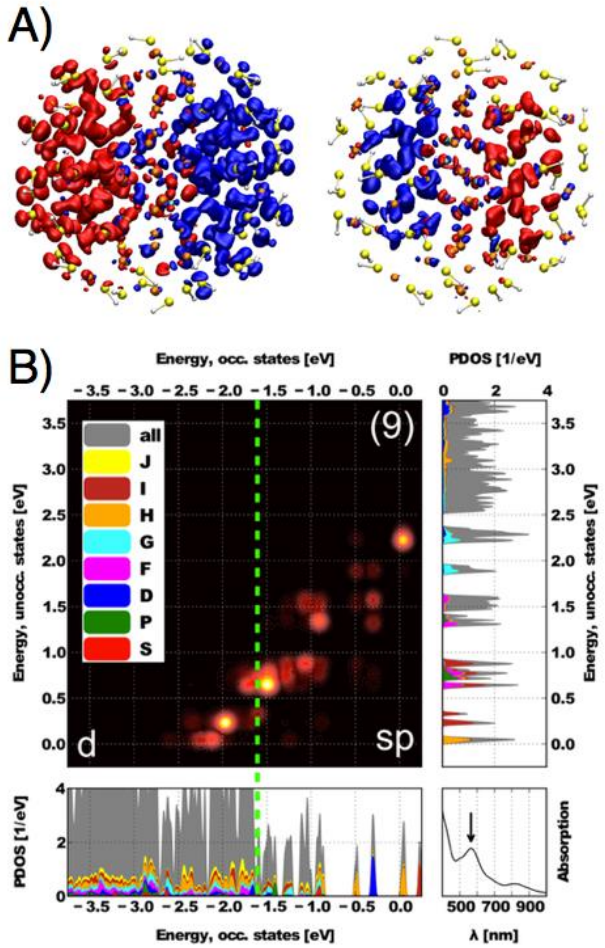

Figure 22. (A) Induced densities for cluster 9 at wavelength of 564 nm. The sp/ligand and d-contributions are visualized separately and the classification is based on the location of the hole states (initially occupied single-electron states). Note the collective dipole-like density oscillation and the opposite phase in oscillations of d-electrons to that of the sp/ligand visualizing a screening effect. (B) TCM analysis of optical transitions for cluster 9 at wavelength of 564 nm. The electronic state contributions to absorption arising from the Au(5d)/Cu(3d)-bands and ligand/Au(6sp)/Cu(4sp)-bands are divided by the vertical dotted lines. Angular momentum projected electronic density of states (vertical in each subfigure. The brighter the yellow area in the correlation plot, the stronger the contribution from this region of occupied to unoccupied single-electron contribution in the transition (Fermi energy is referenced to zero).

Finally, we note that cluster 3 has the minima formation energy (Figure 17) but does not show a plasmonic absorption peak (Figure 19). Cluster 3 has the composition $Au_{114}Cu_{30}(SH)_{60}$ where all the copper atoms are in the ligand shell. It is interesting to note that Negishi et al. reported an EXAFS study of silver- and copper-doped $Au_{25-x}M_x(SR)_{18}$ clusters.[157] Their data shows that copper indeed can be found also in the ligand layer. However, they speculated that these clusters are more prone to aerobic oxidation as compared to clusters where copper is in the metal core, and thus are short-lived in samples exposed to ambient conditions. Little is known about atomic-scale mechanisms by which bimetallic $Au_{(144,145)-x}Cu_x(SR)_{60}$ clusters form. Consequently, our theoretical prediction of energetically preferable $Au_{(144,145)-x}Cu_x(SR)_{60}$ clusters with a high content of copper in the ligand shell challenges experimenters to stabilize and observe cases where ligands directly drive the final composition architecture of heterometallic nanoclusters. If copper is stabilized against aerobic oxidation at the core/ligand interface or in the ligand shell, our calculations predict that such systems are non-plasmonic.

3.4 **Conclusion**

In conclusion, motivated by a recent experiment on intermetallic thiol-stabilized gold-copper clusters with 143 to 145 metal atoms and 60 thiols, we performed detailed computational studies of optical absorption of intermetallic model clusters $Au_{(144,145)-x}Cu_x(SH)_{60}$ with up to 30 incorporated copper atoms in the widely used icosahedral-based $Au_{144}(SR)_{60}$ structure. The calculations predict that the most thermodynamically stable position to dope Cu is in the ligand layer of $Au_{144}(SR)_{60}$. However, the ligand layer is known to be subject to aerobic oxidation and therefore is not thought to be observed experimentally. On the other hand, Cu doping in the inner

metal core is also thermodynamically favorable relative to $Au_{144}(SR)_{60}$, and leads to heterometallic clusters that exhibit plasmonic absorption at sizes that do not exhibit plasmonic absorption in pure $Au_{144}(SR)_{60}$ clusters. Electron charge is transferred from copper to gold and an almost perfect alignment of Cu(3d) and Au(5d) bands is observed. Strong absorption between 500 and 600 nm is observed for the energetically most favorable clusters, and our analysis of the transition reveals that it is a plasmon-like collective excitation in the metal core. Our study demonstrates the need to understand and synthetically control the atomistic details controlling optical properties of thiol-stabilized gold and intermetallic gold-based clusters. In particular, the relationship between atomic arrangement and optoelectronic properties is enriched in systems containing 100 - 200 metal atoms, where aspects of both “molecular” and “metallic” electronic structures drive nanoparticle behavior.

4.0 Surface Chemistry Controls Magnetism in Cobalt Nanoclusters

(Portions of this work were published previously and are reprinted with permission from Hartmann, M. J.; Millstone, J. E.; Häkkinen, H. *J. Phys. Chem. C* **2016**, 20822-20827. Copyright 2015 American Chemical Society.)

4.1 **Introduction**

Magnetic materials have received widespread interest due to their potential in technological applications ranging from biomedicine to data storage.[3, 158] Nanomaterials provide attractive platforms to build magnetic systems because their properties emerge from a large but tunable parameter space defined by size, shape, composition, and surface chemistry.[159-161] Specifically, nanomaterials in the 1-3 nm size range are particularly interesting due to the cross over from discrete quantum-confined electron energy levels to continuous electronic band structure observed in bulk materials.[162-164] These systems often exhibit enhanced per atom magnetic moments relative to bulk, generally attributed to an average under-coordination of atoms in the particle.[165]

Results from both experiments and simulations on monometallic gas-phase Co nanoclusters (Co_N, $N < 100$) predict a strong size dependent per atom magnetic moment, where magnetic moments as high as 2.6 μ_B/atom are observed,[166-167] significantly higher than the bulk

value of 1.72 μ_B/atom.[167] Although beam experiments can yield a wealth of useful information on size-specific properties of naked metal clusters, the clusters exist in the experiment for only a few milliseconds.[168] For practical studies of nanoparticles, interparticle reactivity must be suppressed. Interparticle reactivity can be suppressed effectively with wet chemistry techniques, where clusters are terminated by an adsorbate layer (adsorbate may range from solvent molecules to polymers), and these adsorbates passivate the nanocluster by making bonds to the reactive metal surface.[169-170] Unfortunately, the introduction of these ligand shells may also quench the magnetic moment of the system.[171-172]

In general, the extent of ligand-induced quenching is dependent on the identity of both the metal and the ligand.[173] One strategy that has been used to overcome magnetic moment quenching due to ligand passivation is to stabilize clusters by polymer physisorption. The authors found that with these weakly interacting ligands, magnetism was not significantly impacted and the resulting clusters exhibited a per atom magnetic moment ~25% higher than bulk Co.[172] Implantation of magnetic impurities and growth of magnetic nanoparticles in a semiconductor material can also act as a stabilizing matrix for the nanoparticle, and has proven successful in isolating systems with elevated magnetic moments.[174-175]

Despite successful synthesis of nanomaterials with enhanced magnetism relative to bulk, a broad understanding of the fundamental principles that describe nanoparticle magnetism for a given metal-ligand combination does not currently exist. Metal-ligand interactions are well described in molecular coordination complexes studied in classical inorganic chemistry, where ligand identity has long been known to have dramatic influence over the emergent electronic and magnetic properties of the constituent metal atom(s).[176-178] Specifically, ligands impact two major electronic parameters in coordination complexes: 1) changing the d-electron count on the

metal and thereby changing the number of unpaired electrons, and/or 2) changing the energy level splitting of the metal d orbitals through a ligand field effect. These strong impacts of ligands on the emergent properties of coordination complexes, indicate the potential for important ligand effects in larger metal containing structures, especially with respect to how they may scale as a function of metal cluster size.

Herein, we demonstrate how surface chemistry of Co_N (N = 13, 55) nanoclusters dictates the emergent magnetic properties of the entire structure. Icosahedral Co_{13} and Co_{55} cores provide ideal starting points for this study because they have been predicted to be a global structural minimum for gas-phase Co clusters, while also exhibiting high magnetic moments relative to bulk Co due to under-coordination of the surface atoms.[166-167, 179] Specifically, we report that ligand binding induces local changes on the surface of Co_{13} nanoclusters, analogous to effects in ligand field theory However, because the local coordination site is a component of a larger nanocluster, the impact of each ligand is observed beyond the metal center to which it is directly bound. For example, ligand identity can induce significant changes in the magnetic moment of atoms in the center of the clusters, despite no direct contact between the ligand and the metal. Further, we investigate how ligand effects scale as a function of cluster size by considering how ligand composition impacts the magnetic moment of nanoclusters with a Co_{55} core. To evaluate the origin of the variation in magnetic properties as a function of cluster ligand identity, we analyze atomic Bader charges,[180] local and total magnetic moments (TMM), as well as projected density of states for a variety of ligand shell compositions.

4.2 **Computational Methods**

Density functional theory as implemented in GPAW (grid-based projector augmented wave method) is used for all calculations.[181] Each calculation was preformed within the generalized gradient approximation (GGA) with the Perdew-Burke-Ernzerhof (PBE) exchange correlation functional.[182] The GGA level of theory has been used extensively to describe magnetic properties in similar Co nanocluster systems,[183] and has provided good agreement with experimental results.[172] The system was modeled on a real space grid with a grid spacing of 0.2 Å, all optimizations were performed with a convergence criterion of 0.05 eV/Å for the residual force, without a symmetry constraint, and scalar relativistic corrections were included for Co. The TMM was determined iteratively by simultaneous optimization with the molecular orbitals during the self-consistent field procedure. All clusters were modeled as neutral and a starting magnetic moment of 2.0 μ_B per Co atom was used to initialize each calculation. Various starting magnetic moments were tested for a bare Co_{13} cluster in order to verify that the final spin state was independent of the initial conditions from the calculation (Table 7).

Non-collinear magnetism calculations we executed with the Quantum Espresso (QE) software package.[184] We used a similar computational setup for the QE calculations as the GPAW calculations with the exception that a plane-wave basis set with a cut-off energy of 30 Ry and ultrasoft Vanderbilt pseudopotentials[185] were used to treat the core electrons. Our calculated TMMs from QE were consistent with those calculated with GPAW (Table 8).

Table 7. Various starting local magnetic moments (LMMs) used to initiate single point calculations for bare Co_{13} cluster and final total magnetic moment (TMM) of the cluster.

Initial LMM (μ_B/atom)	Calculated TMM (μ_B)
0.1	30.92
1.0	30.92
1.5	30.92
2.0	30.92
2.5	30.92

Table 8. Total magnetic moments of each system calculated with GPAW and QE.

System	TMM with GPAW (μ_B)	TMM with QE (μ_B)
Co_{13} (bare cluster)	30.9	31.0
$Co_{13}(PH_3)_{12}$	21.0	21.0
$Co_{13}(PH_3)_9Cl_3$	24.0	24.0
$Co_{13}(PH_3)_6Cl_6$	27.0	27.0
$Co_{13}(PH_3)_3Cl_9$	29.8	29.9
$Co_{13}Cl_{12}$	29.7	29.7
$Co_{13}F_{12}$	31.1	31.2
$Co_{13}Br_{12}$	27.8	27.8
$Co_{13}(OH)_{12}$	28.9	29.0
$Co_{13}(CO)_{12}$	20.2	20.7
$Co_{13}(NH_3)_{12}$	22.6	23.0
$Co_{13}(PCl_3)_{12}$	21.0	21.0

The ligand binding energy (LBE) of each Co_N (N = 13 or 55) cluster was calculated using the following equation.

$$LBE = E[Co_{\mathrm{N}}(Lig)_{\mathrm{M}}] - (E[Co_{\mathrm{N}}] + \mathrm{M} * E[Lig])$$

Where M is the number of ligands in the cluster. In cases where the ligand has an unpaired electron and is therefore not stable as a radical (i.e. Cl), the hydrogenated version of the ligand was used to calculated E[Lig] and the LBE was calculated with the following modified version of the above equation.

$$LBE = \left(E[Co_{\mathrm{N}}(Lig)_{\mathrm{M}}] + \frac{M}{2} * E[H_2]\right) - (E[Co_{\mathrm{N}}] + \mathrm{M} * E[Lig])$$

The local magnetic moment atom i is given by the following equation.[186]

$$\mu_i = \int_0^R [\rho_\uparrow(r) - \rho_\downarrow(r)]dr$$

Where R is the radius of the augmentation sphere centered at atom i, and $\rho_{\uparrow}(r)$ ($\rho_{\downarrow}(r)$) is the majority (minority) spin density. The radius of the augmentation sphere in which the integration is preformed is chosen as half the bond length of the nearest neighbor bond length to ensure there is no overlap between atoms. The total magnetic moment of the system is given by the sum of each atoms local magnetic moment.

To estimate the error in the calculation of total magnetic moment we report the value of spin contamination in Table 10. The total magnetic moment is calculated as an integral of the net spin density over all space. In an unrestricted calculation, the spatial components of the spin-up and spin-down wave functions can be different. Spatial mismatch results in regions of space where the net spin density is negative. In DFT, spin contamination is calculated as the integral of the net spin density over all space where the spin down electron density is greater than the spin up electron density.

4.3 **Results and Discussion**

Eleven unique ligand shell compositions were considered, each with an icosahedral Co_{13} core. For each system, the ligand shell consists of 12 ligands, each one binding directly to one Co atom on the surface of the core (Figure 23). The main 'families' of ligands considered are X-type ligands where both the ligand and metal provide one electron to form a bond with the surface and L-type ligands where the ligand provides 2 electrons to the surface to form a dative bond. We also consider a set of clusters with ligand shells that are a mixture of the two ligand types. Together these families sample a wide range of electronic interactions with the Co surface. Phosphine and chlorine ligands used throughout this work are commonly seen binding directly to a single surface metal atom in clusters of similar size, particularly for Au-based clusters.[187-188] These Au-phosphine and Au-halide motifs provided a starting point for the construction of other ligand systems, and in each case our structure successfully converged to a local geometry minimum without a significant change in ligand binding motif (Table 9). For each cluster considered, ligand binding was found to be favorable as demonstrated by the negative binding energies for each system (Table 10). However, we note that it can be challenging to determine binding motifs of these ligands due to a lack of *a priori* knowledge concerning ligand binding geometries to the surface of a nanocluster and are likely in local geometry minima.[188]

Table 9. Average bond length for three different bonds and angle formed between center, Co-surface, and ligand head group atoms in each cluster with a Co_{13} core.

System	Center-Surface BL (Å)	Surface-Surface BL (Å)	Surface-Ligand BL (Å)	Co-Co-Ligand angle (°)
Co_{13} (bare cluster)	2.34	2.46	-	-
$Co_{13}(PH_3)_{12}$	2.35	2.48	2.20	172
$Co_{13}(PH_3)_9Cl_3$	2.35	2.48	2.21	172
$Co_{13}(PH_3)_6Cl_6$	2.36	2.48	2.20	171
$Co_{13}(PH_3)_3Cl_9$	2.36	2.48	2.16	170
$Co_{13}Cl_{12}$	2.36	2.48	2.07	175
$Co_{13}F_{12}$	2.37	2.49	1.74	172
$Co_{13}Br_{12}$	2.35	2.47	2.21	176
$Co_{13}(OH)_{12}$	2.35	2.48	1.77	1.67
$Co_{13}(CO)_{12}$	2.37	2.50	1.81	174
$Co_{13}(NH_3)_{12}$	2.35	2.48	2.08	174
$Co_{13}(PCl_3)_{12}$	2.37	2.55	2.20	171

Table 10. Average LBE and percentage of spin contamination with a Co_{13} core.

System	Average LBE (eV/Ligand)	Spin Contamination (%)
$Co_{13}(PH_3)_{12}$	-1.06	4.1
$Co_{13}(PH_3)_9Cl_3$	-1.28	2.4
$Co_{13}(PH_3)_6Cl_6$	-1.44	1.8
$Co_{13}(PH_3)_3Cl_9$	-1.50	1.7
$Co_{13}Cl_{12}$	-1.43	2.5
$Co_{13}F_{12}$	-0.87	2.2
$Co_{13}Br_{12}$	-1.62	3.2
$Co_{13}(OH)_{12}$	-0.70	2.7
$Co_{13}(CO)_{12}$	-1.35	2.2
$Co_{13}(NH_3)_{12}$	-0.64	4.5
$Co_{13}(PCl_3)_{12}$	-1.04	3.7

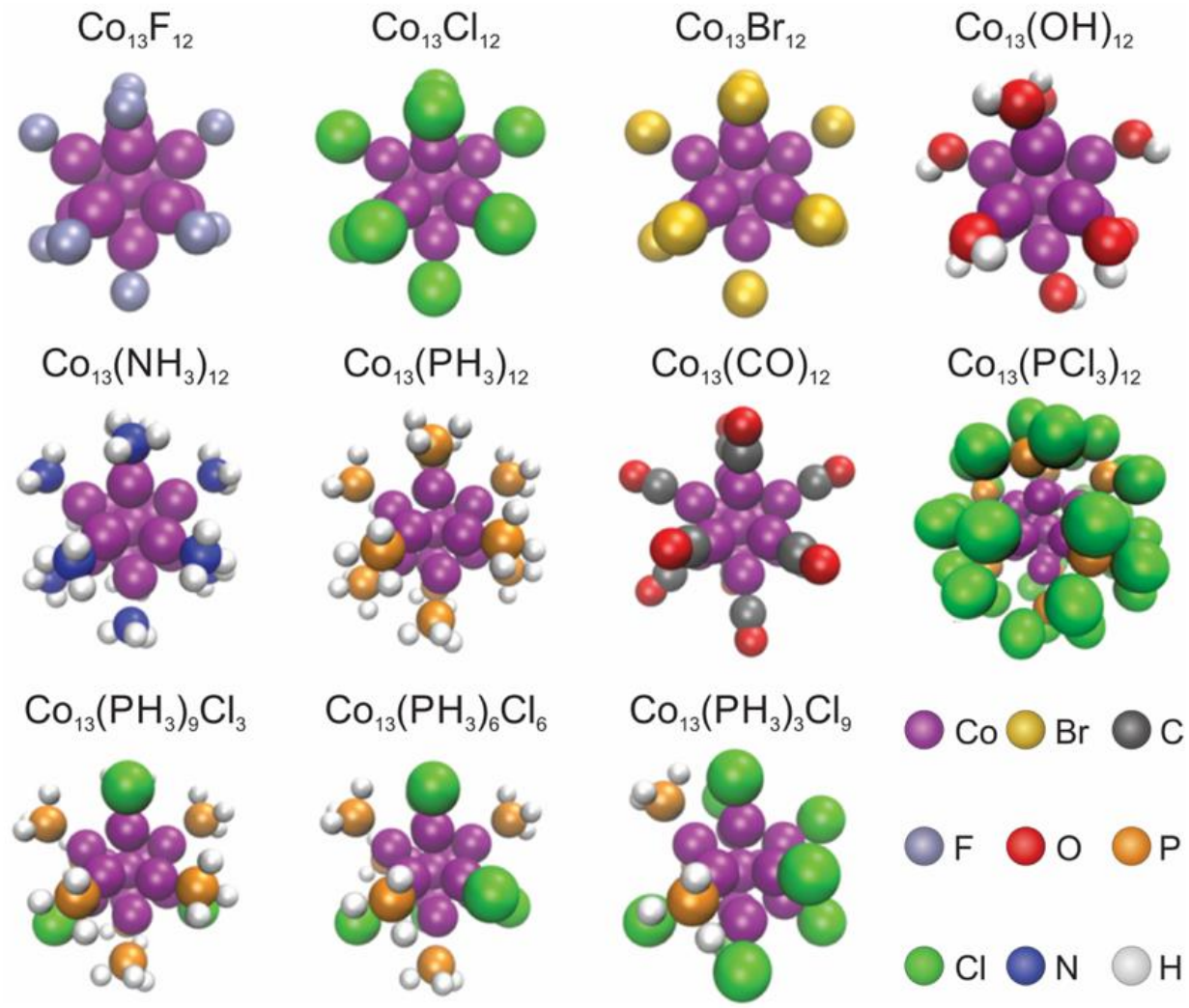

Figure 23. Optimized Co_{13} core structures for each unique ligand composition considered.

Figure 24 shows the relationship between the TMM and the total Bader charge on the Co_{13} core. The horizontal dotted line at 30.9 μ_B indicates the TMM for the bare Co_{13} cluster. In general, there is a net quenching of the TMM relative to the bare Co_{13} cluster for each system due to spins being paired to form surface-ligand bonds. However, as the charge on the Co_{13} core becomes more positive, the TMM of the nanocluster increases. This effect persists through the fully fluorinated ligand shell, where the TMM of the bare cluster can be completely recovered relative to the bare cluster. Since the ligand identity controls the amount of electron density withdrawn from the core, electronegativity of the ligand binding group provides a handle within each ligand family to control the TMM of the nanocluster. While the majority of ligands exhibit a linear relationship between core charge and TMM (R^2 = 0.91 without CO), CO exhibits a dramatic departure from this trend. A ligand shell containing 12 CO ligands withdraws a total of 2.4 electrons from the Co_{13} core. This amount of withdrawn charge is consistent with the electronegativity difference between the Co and C atoms. However, based on the TMM vs. charge correlation formed by the other ligand shell compositions considered, we would expect a total magnetic moment of approximately 24.8 μ_B. Instead, we calculate a TMM of 20.2 μ_B for a complete CO ligand shell. This result agrees with existing literature, where it is known that CO has a dramatic effect in quenching the magnetic moment of both Co_N[189] and Ni_N[173] nanoclusters. To understand these trends, we consider both local magnetic moments (LMM) and atomic charges as a function of atom position for each unique ligand shell composition considered.

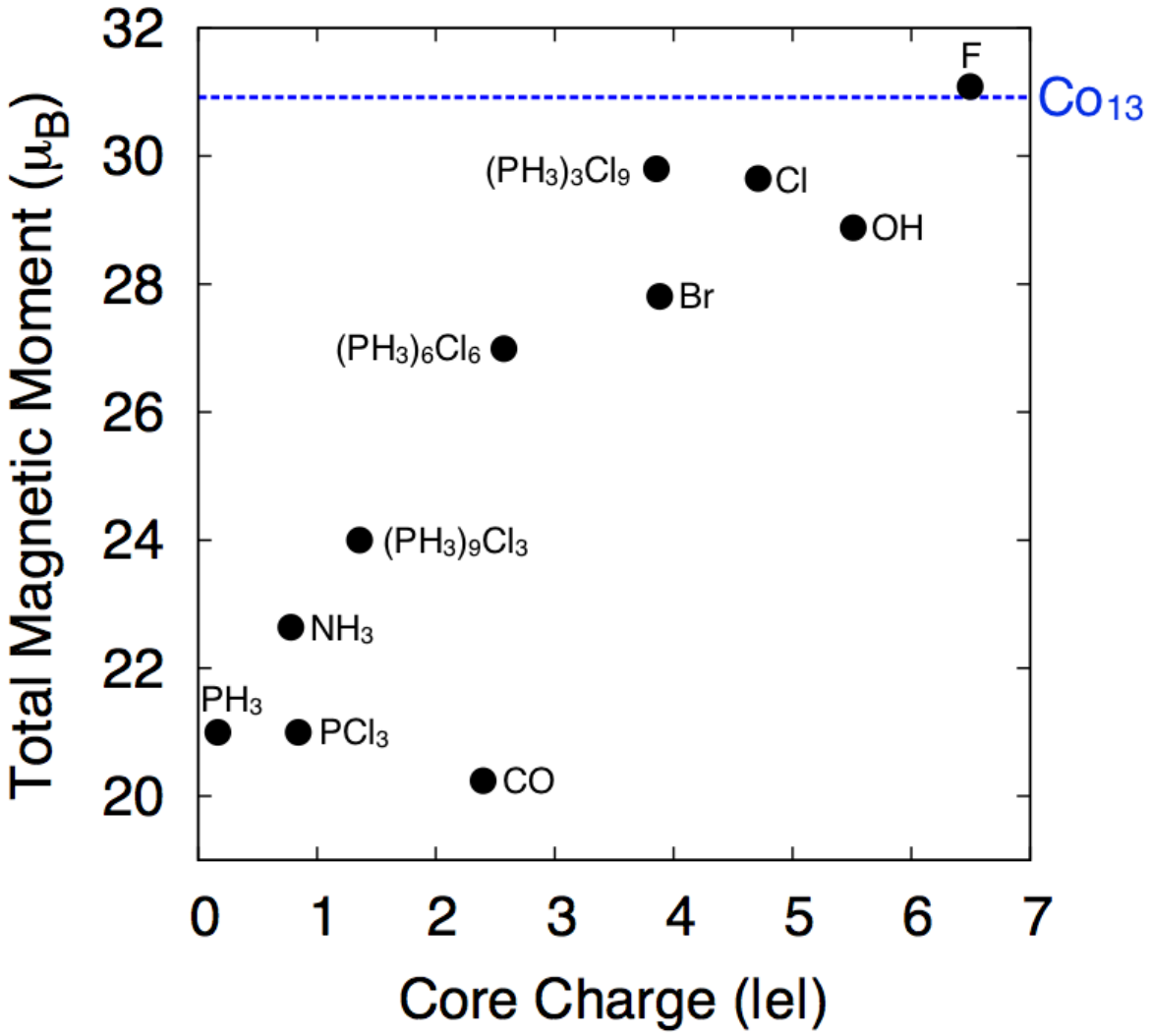

Figure 24. Total magnetic moment as a function of Bader charge on cluster core; dotted line indicates value for bare Co_{13} cluster.

The average LMM on each Co atom spans a wide range as a function of different ligand shells (Table 11). For example, the PH_3 ligand system quenches the LMM of each Co atom dramatically to 1.61 $\mu_B/atom_{Co}$; smaller than the bulk value of 1.72 $\mu_B/atom_{Co}$. However, as the charge on the Co_{13} core increases from ligand binding, the LMM/$atom_{Co}$ reaches a peak of 2.39 $\mu_B/atom_{Co}$ with a fluorine ligand, appreciably higher than the bulk value. In each case non-collinear magnetism calculations show that the absolute magnetization is between 1.2-2.9 μ_B more than the total magnetization, indicating that there is little antiferromagnetic coupling between metal and ligand. Core-to-surface and surface-to-surface bond lengths, as well as surface-to-ligand bond angles show that the changes in the magnetic moment are not driven by changes in geometry between ligand shells (Table 9).

Table 11. Magnetic properties as a function of position in the cluster for Co_{13} clusters.

System	TMM (μ_B)	Absolute Magnetization (μ_B)	Center LMM (μB/atom)	Average Surface LMM (μB/atom)
Co_{13} (bare cluster)	30.9	32.1	2.43	2.37
$Co_{13}(PH_3)_{12}$	21.0	23.4	0.10	1.74
$Co_{13}(PH_3)_9Cl_3$	24.0	25.9	0.47	1.94
$Co_{13}(PH_3)_6Cl_6$	27.0	28.4	1.04	2.12
$Co_{13}(PH_3)_3Cl_9$	29.8	31.6	1.37	2.29
$Co_{13}Cl_{12}$	29.7	31.7	1.42	2.24
$Co_{13}F_{12}$	31.1	32.8	1.38	2.30
$Co_{13}Br_{12}$	27.8	30.1	1.28	2.07
$Co_{13}(OH)_{12}$	28.9	31.1	1.40	2.12
$Co_{13}(CO)_{12}$	20.2	21.8	-0.18	1.71
$Co_{13}(NH_3)_{12}$	22.6	25.5	0.07	1.87
$Co_{13}(PCl_3)_{12}$	21.0	23.2	0.17	1.72

Table 12. Bader charges as a function of position in the cluster for Co_{13} clusters.

System	Total Core Charge (e)	Center Atom Charge (e)	Average Surface Atom Charge (e)
Co_{13} (bare cluster)	0.00	0.19	-0.02
$Co_{13}(PH_3)_{12}$	0.17	-0.33	0.04
$Co_{13}(PH_3)_9Cl_3$	1.36	-0.31	0.14
$Co_{13}(PH_3)_6Cl_6$	2.57	-0.29	0.24
$Co_{13}(PH_3)_3Cl_9$	3.85	-0.28	0.34
$Co_{13}Cl_{12}$	4.71	-0.31	0.42
$Co_{13}F_{12}$	6.49	-0.36	0.57
$Co_{13}Br_{12}$	3.88	-0.28	0.35
$Co_{13}(OH)_{12}$	5.51	-0.29	0.48
$Co_{13}(CO)_{12}$	2.40	-0.45	0.24
$Co_{13}(NH_3)_{12}$	0.78	-0.28	0.09
$Co_{13}(PCl_3)_{12}$	0.84	-0.32	0.10

The most dramatic difference in the LMM between systems capped with X-type vs. L-type ligands is at the center atom. A 100% PH_3 ligand almost completely quenches the magnetic moment in the center of the cluster. However, as the percentage of Cl ligands in the ligand shell increases, the LMM at the center atom recovers to 1.42 μ_B for the fully chlorinated ligand shell. Interestingly, the charge at the center of the cluster does not change appreciably as the ligand shell changes. The constant charge but dynamic magnetic moment of the center atom indicates that the ligand induces a collective effect where the ligand shell controls the spin state of the Co atom at the center of the cluster, despite not being directly bound.

In addition to composition, the morphology of ligand shells containing both X-type and L-type ligands may impact the magnetism of the cluster. To understand the impact various ligand shell morphologies has on the calculated magnetic properties, we generated three different

systems with a ligand shell composition of $(PH_3)_6Cl_6$. These three systems include the randomly generated structure discussed in the main text, a 'half' system with a completely phase separated ligand shell, and a 'striped' system with a stripe of PH_3 ligands around the equator of the core that separates 2 bunches of 3 Cl ligands. Figure 25 and Table 13 show the structures and magnetic properties of these three systems respectively. Overall, there is very little deviation in the distribution of net spin density between these three systems, indicating that ligand shell composition instead of morphology is the dominant factor in determining the final magnetic properties of the nanocluster.

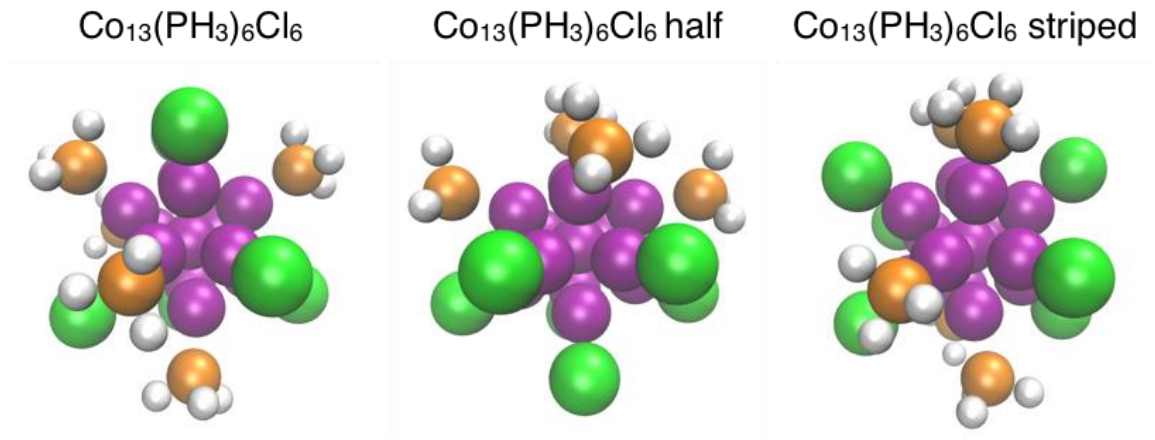

Figure 25. Structures of each ligand morphology considered with a $(PH_3)_6Cl_6$ ligand shell composition.

Table 13. Magnetic properties of $(PH_3)_6Cl_6$ ligand shells with three different morphologies.

System	TMM (μ_B)	Center LMM (μ_B/atom)	Edge LMM (μ_B/atom)
$Co_{13}(PH_3)_6Cl_6$ mixed	27.0	1.04	2.12
$Co_{13}(PH_3)_6Cl_6$ half	27.0	1.02	2.10
$Co_{13}(PH_3)_6Cl_6$ striped	27.0	0.93	2.12

The LMM on the surface is controlled directly by the ligand, where Co surface atoms bound to X-type ligands (i.e. Cl) have higher magnetic moments than those bound to L-type ligands (i.e. PH_3). To further elucidate the impact of ligand passivation on the magnetic properties of Co_{13}, we studied multiple ligand systems from each bonding family outlined above. Within the family of X-type ligands, a clear trend is observed consistent with the Nephelauxetic effect.[10] Here, the nature of the ligands bond with the metal atom plays a role in determining observed magnetic properties. In the case of fluorine, which polarizes the bond with the surface more strongly than the other X-type ligands, the ligands interaction with the surface becomes more localized. This means the bond has a smaller volume, driving up the repulsion energy between electrons participating in the bond, causing the electrons participating in the interaction to not pair-up completely from ligand passivation. Therefore, the electron localizing ability of fluorine provides a driving force for the spins to remain unpaired and contribute to the high LMMs of the surface atoms. For X-type ligands, this effect is also responsible for a small magnetic moment on the ligand itself in the case of X-type ligands (0.1 – 0.2 μ_B/ligand, Table 14). The electron localizing ability of X-type ligands provides fine control of the TMM and distribution of spin density in the Co_{13} nanoclusters.

Table 14. Average Bader charge and average LMM on each ligand bond to Co_{13} core.

System	Ligand Charge (e/ligand)	Ligand LMM (μ_B/ligand)
$Co_{13}(PH_3)_{12}$	-0.01	0.00
$Co_{13}(PH_3)_9Cl_3$	-0.11	0.02
$Co_{13}(PH_3)_6Cl_6$	-0.21	0.04
$Co_{13}(PH_3)_3Cl_9$	-0.32	0.08
$Co_{13}Cl_{12}$	-0.39	0.12
$Co_{13}F_{12}$	-0.54	0.18
$Co_{13}Br_{12}$	-0.32	0.11
$Co_{13}(OH)_{12}$	-0.46	0.16
$Co_{13}(CO)_{12}$	-0.20	0.00
$Co_{13}(NH_3)_{12}$	-0.06	0.00
$Co_{13}(PCl_3)_{12}$	-0.07	0.00

Each L-type ligand shell causes the LMM at the center of the cluster to be almost completely quenched, a distinct behavior from the X-type ligands. For the PH_3 ligand, we calculate a small LMM of 0.10 μ_B/atom$_{Co}$ at the center atom, and a near bulk value of 1.74 μ_B/atom$_{Co}$ on the surface of the core. The NH_3 ligand system showed a 0.07 μ_B/atom$_{Co}$ LMM at the center, and had a slightly higher surface LMM of 1.87 μ_B/atom$_{Co}$ due to the difference in electron localizing ability between P and N (*vide supra*). Interestingly, the LMM at the center for the CO ligand took a small negative value, indicating a small amount of spin contamination near the center atom.

To investigate whether CO's ability to π-backbond is responsible for the more dramatic quenching of the Co_{13} magnetic moment, we considered a PCl_3 ligand shell that has a π-acidity between that of the PH_3 and CO ligand shells. Phosphines are known to have molecular orbitals

of π symmetry, formed from hybridization between P 3d orbitals and P-R σ* orbitals, that can accept electron density from a metal.[190] Increasing the ability of the phosphine to π-backbond with chlorine functionality has little impact on the TMM and distribution of LMMs in the Co_{13} nanocluster, where the LMM of $Co_{13}(PCl_3)_{12}$ is 21.0 μ_B, identical to the $Co_{13}(PH_3)_{12}$ system. The distribution of LMMs in the PH_3 and PCl_3 exhibit center atom LMMs of 0.10 and 0.17 $\mu_B/atom_{Co}$ and have average surface LMMs of 1.74 and 1.72 $\mu_B/atom_{Co}$ respectively. However, the addition of chlorine in the ligand does impact the charge on the Co_{13} core, giving it a charge of -0.84 e, placing it between the $Co_{13}(PH_3)_{12}$ and $Co_{13}(CO)_{12}$ nanoclusters in Figure 24.

In order to show the difference between the influence of X-type and L-type ligand binding, we plotted the projected local density of states for a single Co-ligand pair for PH_3, CO, F, and Cl ligands in Figure 26A. Here, the difference in binding influences several aspects of the density of states. First, each ligand type causes the 3d Co states to hybridize with p states. Also, although the majority spin d states remain almost entirely occupied, there is a shift to lower energies for the minority spin d-band, leading to an increase in the number of spin down electrons and a net quenching of the TMM relative to particles terminated by X-type ligands. The minority HOMO orbitals showing the qualitative difference in orbital character is shown Figure 26B.

The RPDF of the change in electron density induced from binding a ligand shell is shown in Figure 26C. Here, we calculated the difference in electron density ($\Delta\rho_B$) induced by ligating the bare nanocluster using the following equation.

$$\Delta\rho_B = \rho_{total} - (\rho_{core} + \rho_{ligand})$$

Where ρ_{total} is the total electron density, ρ_{core} is the electron density of the bare core isolated from the ligands, and ρ_{ligand} is the density of the whole ligand system when isolated from the core.

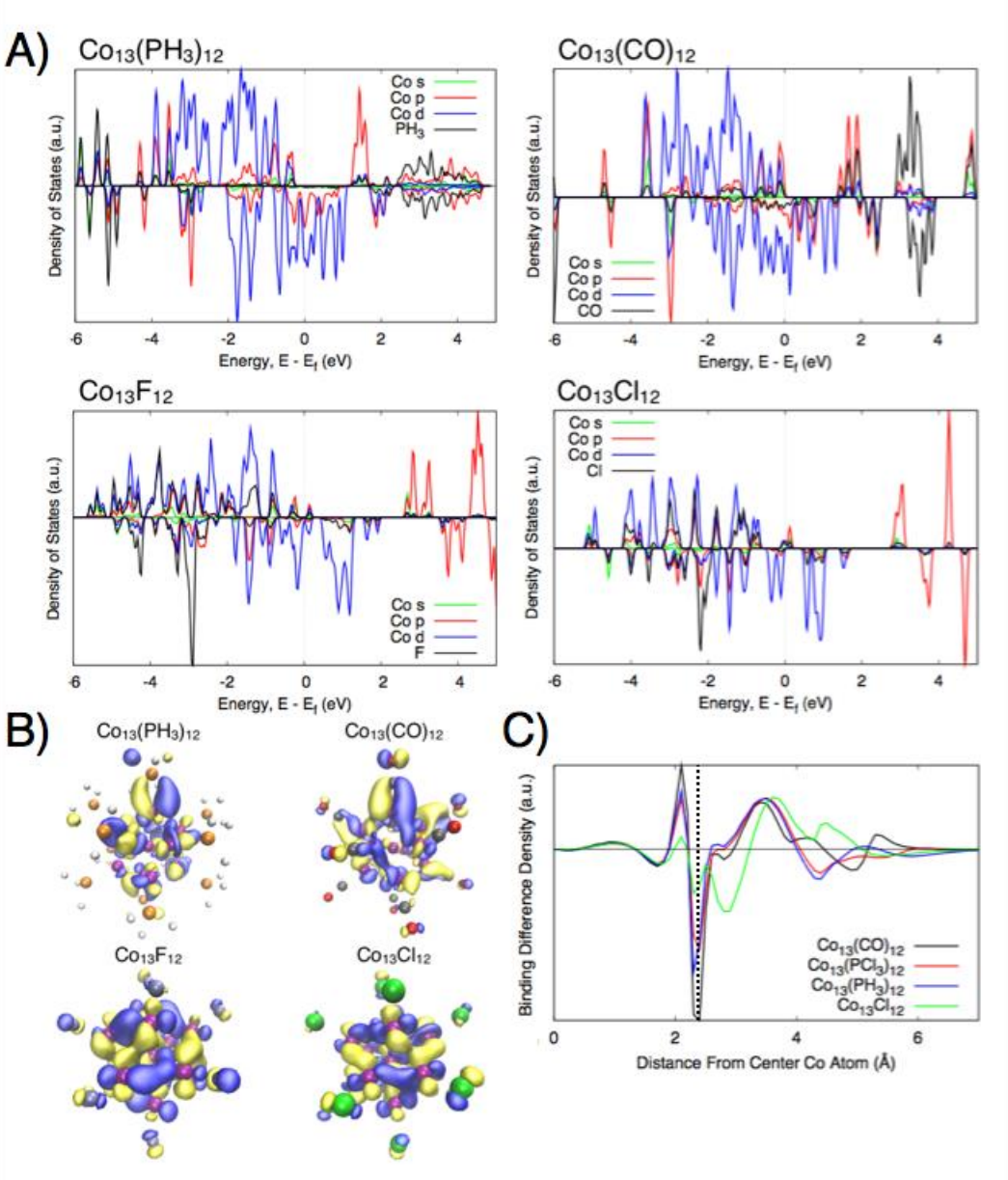

Figure 26. (A) Projected density of states of states for a single metal-ligand pair from the $Co_{13}(PH_3)_{12}$, $Co_{13}(CO)_{12}$, $Co_{13}F_{12}$, $Co_{13}Cl_{12}$ systems. Majority (minority) spin channel is plotted above (below) x-axis. (B) Minority spin HOMO orbitals for $Co_{13}(PH_3)_{12}$, $Co_{13}(CO)_{12}$, $Co_{13}F_{12}$, and $Co_{13}Cl_{12}$ systems. (C) Radial probability density function of the difference electron density induced from the binding of the ligand shell. Vertical dashed line at a radial distance of 2.36 Å corresponds to the position of the surface Co atoms relative to the center atom in the clusters.

Overall, the net result of binding any ligand considered here to a bare Co_{13} core is a charge transfer from the Co surface atoms to the ligands, as seen from a negative peak (depletion) at 2.3 Å and a positive peak (accumulation) at 3.5 Å. Inside the nanocluster core, the overall character of the binding is the same for each ligand shell considered, with the only differences being the amount of charge transfer to the ligands. Chlorine, an X-type ligand, shows the smallest change in electron density in the core, but has a qualitatively different binding character in the ligand shell than the L-type ligands. Binding of each L-type ligand show very similar binding behaviors up until a radial distance of 4.0 Å, approximately the radial position of the ligand head groups. Here, the difference in π-acidities becomes evident where CO shows accumulation at 4.1 Å and 5.5 Å, the radial positions where CO's π* orbitals have largest amplitude. The same behavior between the $Co_{13}(PH_3)_{12}$ and $Co_{13}(PCl_3)_{12}$ systems, where deviations due to π-backbonding emerge at the radial position of the π* orbitals on the phosphine ligands, around 5 Å. Together, these results indicate that π-backbonding is observed at the surface and plays a role in controlling the distribution of electron density throughout the Co_{13} nanoclsuters.

For Co_{13} nanoclusters, specific molecular descriptors of binding are strongly correlated with magnetic properties, likely because the overall electronic structure of each cluster is discrete. However, particle size plays a key role in determining magnetic properties in these materials because a slight increase in the number of core metal atoms can have a large influence on spacing between energy levels, where bulk-like electronic structures can emerge at only a few nanometers.[191] In order to study the scope of the size dependent ligand-controlled magnetic properties, we considered a set of Co_{55} nanoclusters that are one atomic layer larger. Three

different ligand shells of 100% PH_3, 50% PH_3/50% Cl, and 100% Cl were studied, and were designed to transition between a full X-type ligand shell and a full L-type ligand shell (Figure 27A).

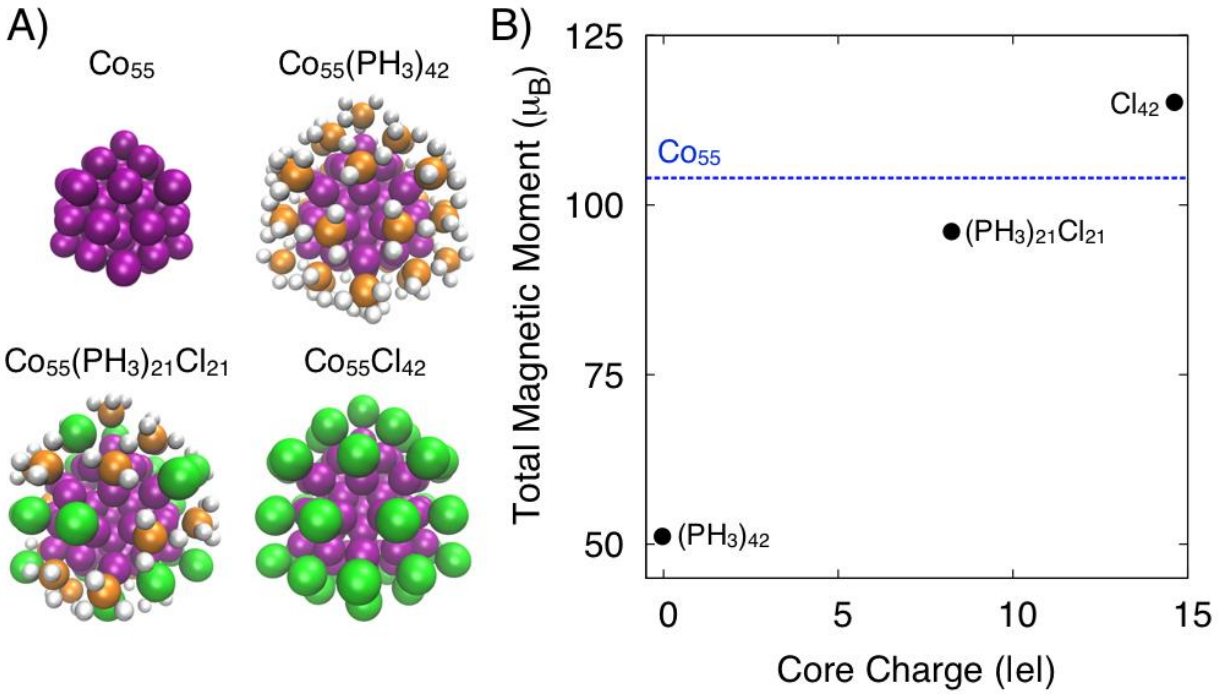

Figure 27. (A) Optimized bare Co_{55} core and three ligated Co_{55} systems considered. (B) Total magnetic moment as a function of Bader charge on Co_{55} core; dotted line indicates value of the bare Co_{55} cluster.

Figure 27B shows the correlation between TMM and core charge for the Co_{55} clusters considered. Similar to the Co_{13} analogs of these ligand shell compositions, as the number of Cl ligands increases, and therefore the core charge, so does the TMM. For the Co_{55} nanoclusters however, the system with a fully chlorinated ligand shell supports a higher TMM than the bare Co_{55} cluster. The origin of this behavior can be seen by looking at the LMMs by position reported in Table 15, where each surface atom has a higher LMM when directly bound to a Cl atom, analogous to the behavior observed in the Co_{13} case.

Table 15. Positional LMMs for clusters with a Co_{55} core.

System	TMM (μ_B)	Center LMM (μ_B/atom)	Middle Shell LMM (μ_B/atom)	Surface LMM (μ_B/atom)
Co_{55} (bare cluster)	104.0	1.71	1.81	1.92
$Co_{55}(PH_3)_{42}$	51.2	1.07	1.04	0.91
$Co_{55}(PH_3)_{21}Cl_{21}$	96.1	1.56	1.44	1.81
$Co_{55}Cl_{42}$	115.2	1.88	1.49	2.14

In general, the per-atom LMMs for both the bare and ligand-stabilized systems are lower for all Co_{55} clusters when compared to their Co_{13} analogs, due to a higher average Co coordination number. The $Co_{55}(PH_3)_{42}$ system induces a similar LMM quenching at the center as is observed in the $Co_{13}(PH_3)_{12}$ system, however the center atom magnetic moment is less quenched in the Co_{55} system. Further, the quenching behavior is observed uniformly over each atom in the cluster, where each atom has a LMM between 0.9 and 1.1 $u_B/atom_{Co}$. The $Co_{55}Cl_{42}$ system also follows the trends seen in the $Co_{13}Cl_{12}$ system, with the chlorine ligands localizing charge and increasing the LMM of the bound Co atom. A small LMM on each chlorine ligand is also observed when bound to a Co_{55} core. Overall, the range of LMMs is not as wide as it is for

clusters with a Co_{13} core, but is still significant and ranges over 1 $\mu_B/atom_{Co}$ from largest to smallest.

4.4 **Conclusion**

We have demonstrated that ligand chemistry is a powerful method to manipulate the magnetic properties of Co nanoclusters. First, the type of metal-ligand bond at the surface plays a major role in determining the TMM by modulating the charge of the cluster core. Further, parameters such as the polarization of the metal-ligand bond, as well as the ability of the ligand to π-backbond significantly influences the resulting magnetic behavior of the system. Finally, as the size of the cluster increases, ligand dependent magnetic properties persist, although they are dampened. Taken together, the exceptional sensitivity of Co particles to their surface chemistry, make them an exciting and broad class of targets for discovery and enhancement of magnetic behavior in materials.

5.0 Ligand Mediated Evolution of Size Dependent Magnetism in Cobalt Nanoclusters

(Portions of this work were published previously and for reproduction of material from PCCP: Adapted from ref 58 with permission from the PCCP owners society. Hartmann, M. J.; Millstone, J. E.; Häkkinen, H. Phys. Chem. Chem. Phys. 2018, 4563-4570. Copyright 2018 Royal Society of Chemistry.)

5.1 **Introduction**

Magnetic materials have received widespread interest due to their diverse applications ranging from data storage devices to biomedicine.[50, 192-196] Magnetic nanomaterials provide particularly promising platforms to develop these technologies largely due to their immense configurational space defined by material size, shape, composition, as well as surface chemistry.[159-161, 197] Specifically, nanomaterials with diameters (d) between 1 and 3 nm bridge the regimes of discrete, molecular electronic structure and that of bulk materials that exhibit continuous band electronic structure.[162, 198] In the d = 1 – 3 nm size range, the addition of a single atom either to the metal core or to the surface as a ligand can have a significant impact on the overall electronic structure of the nanoparticle.[45, 125] Understanding how the position and identity of every atom in these particles contributes to their electronic structure - and ultimately physical

and chemical properties of that system - is vital for translation into next generation magnetic materials.

In recent years, many gas phase experiments have shown that nanoclusters containing 10 - 400 atoms of magnetic elements such as Fe, Co and Ni can exhibit enhanced average per atom local magnetic moments (LMM) relative to their bulk counterparts.[199-200] Specifically, average LMMs in Co nanoclusters have been measured to be as high as 2.6 μ_B/Co atom,[166] 50% higher than the bulk value of 1.72 μ_B/atom for hcp Co. This enhanced magnetism has been shown to result from undercoordination of the surface atoms, which become the dominant species when the number of atoms in a nanocluster drops below approximately 400 atoms.[200]

Gas phase experiments of bare nanoclusters have proven extremely valuable for elucidating the electronic features that lead to a given magnetic behavior. However, gas phase nanoclusters only persist on the order of a few milliseconds,[168] and are therefore not practical systems from which to build new technologies. In order to stabilize magnetic nanoclusters long enough to be useful in magnetic materials, introduction of an external layer around the cluster is required to stabilize the high surface energy of the nanocluster.[169] Colloidal nanocluster syntheses that produce monolayer protected nanoparticles provide a promising route towards ligand-mediated surface stabilization. Unfortunately, attachment of a ligand to the surface of nanoparticles is notoriously correlated with magnetic quenching of the system of interest.[171-172, 183] We have recently shown that magnetic moment quenching from the introduction of a ligand shell to the nanocluster surface is primarily influenced by specific electronic descriptors of the ligand (i.e. X-type vs. L-type), providing insight into how the total magnetic moment of a nanocluster can be tuned through ligand shell engineering.[55] A key question raised by our previous work originated from the observation of an unexpected distribution of LMMs

throughout the Co_{13} and Co_{55} cluster cores as a function of size. Clearly, as the size of the nanocluster increases, a convergence to bulk magnetism must be observed at some system size, however the mode of progression (e.g. linear vs. non-linear), size of cluster at which bulk magnetism emerges, and impact of ligands on these two parameters is currently unknown.

Here, we demonstrate that the LMM of each Co atom within a Co_NL_M nanocluster is primarily determined by the geometric structure and symmetry of the immediate coordination environment. From the collection of these local coordination environments present in a given system, the measured size dependence of magnetism emerges. Using a suite of classically optimized, global minimum, bare Co_N nanoclusters with between 15 and 55 atoms as starting structures, we study 4 types of clusters (44 total clusters studied): bare clusters (i.e. without ligands), clusters terminated in an X-type (Cl) ligand shell, an L-type ligand shell (PH_3), and ligand shells composed of a mixture of the X- and L-type ligands. This large suite of varied nanoclusters differing in core size, ligand identity, and ligand coverage, allow us to sample the correlation between local atomic structure and local nanocluster magnetism in Co_NL_M nanoclusters.

Specifically, we report how the ligand shell composition mediates the evolution of nanocluster magnetism as both a function of size and percent ligand coverage. We show, by leveraging and combining theories for both molecular and bulk systems, that the ligand has both a short range impact, where it directly modifies the LMM of the atom to which it is bound, and a long range impact, where the LMM of subsurface atoms can be influenced by the ligands bound to adjacent atoms. To evaluate the origin of size and coverage dependent magnetism in Co nanoclusters, we analyze the value and distribution of local magnetic moments, atomic Bader charges, ligand binding energies, and projected density of states, and correlate these

computationally accessible figures of merit to structural and topological trends present in the Co_NL_M nanoclusters considered.

5.2 **Computational Methods**

Density functional theory (DFT) as implemented in GPAW (grid-based projector-augmented wave method) is used for all calculations.[181] Each calculation was performed within the generalized gradient approximation (GGA) with the Perdew-Burke-Ernzerhof (PBE) exchange correlation functional.[182] The GGA level of theory has been used extensively in the simulation of magnetic properties in similar Co nanoclusters and shown to agree well with experimental results.[167, 172, 183] Each system was simulated on a real space grid with a grid point spacing of 0.2 Å, the optimizations were performed to a convergence criterion of 0.05 eV/Å for the residual force, and at least 6 Å of vacuum from the edge of the system to the edge of the simulation box surrounded each cluster. Additionally, each optimization was performed without a symmetry constraint and scalar relativistic corrections were included for Co. The total magnetic moment (TMM) of each system was determined iteratively by simultaneous and dynamic optimization with the molecular orbitals during the self-consistent field procedure. Each cluster had a net charge of zero, and a starting magnetic moment of 2.0 μB per Co atom was used to initialize the spin polarization for each system. For each ligand shell type, we verified that our results were independent of the initial value used.

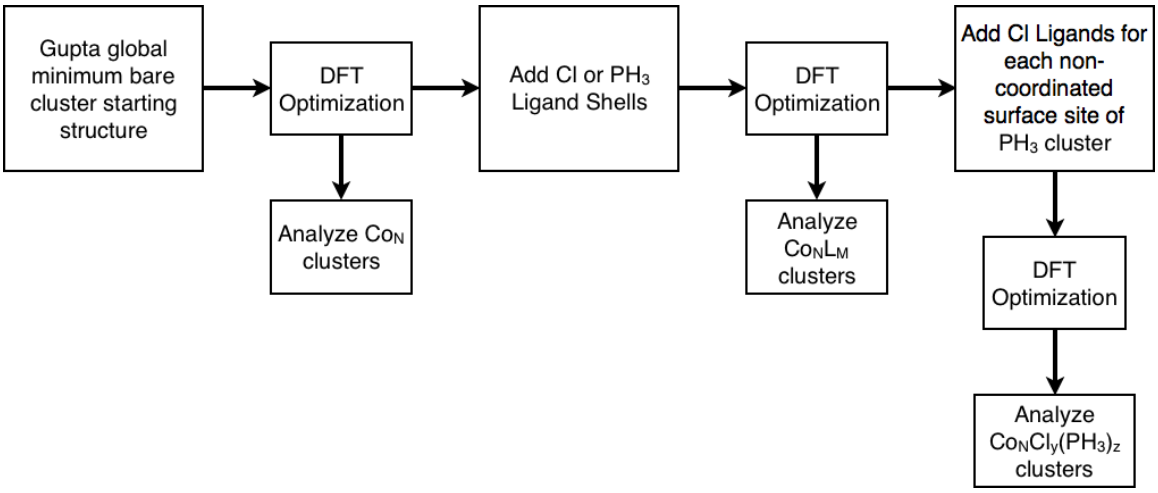

Figure 28. Step-by-step description of process used to create each system considered.

Figure 28 illustrates the method used to generate each structure in this study. Briefly, the initial structures were originally determined by Zhan et al,[201] were attained for this study via the Cambridge Energy Landscape Database, and are the global minimum clusters optimized with the Gupta potential[17] (Co_N, $15 \leq N \leq 55$ in steps of 5). The experimental gas-phase structures of Co_N are not known, so the Gupta minimum structures present a reasonable starting point for this study. These classically optimized Co nanoclusters were then relaxed with DFT to a local minimum, and the resulting structures were used both in the analysis of the bare clusters and as the preoptimized cores to which ligands were added. To avoid the biased positioning of ligands, addition of a ligand shell to the bare clusters was accomplished by parameterization of a line from the geometric center of the cluster through each surface atom, where each surface atom was defined as having a Co-Co coordination number of ≤ 9. The head group of the ligand was placed along this line at a distance of 2.25 Å for each ligand, a reasonable guess for the bond length of each ligand with Co. Following placement of each ligand, a number of randomly selected ligands were chosen to be removed to generate ligand shells with partial coverage, and these new

structures were optimized again with DFT. Finally, the dual ligand shell clusters were generated by adding Cl ligands to each bare surface atom present in the pure PH_3 clusters using the same line parameterization procedure described above. While frequency calculations were not performed to ensure the final geometry was a local minimum, the multiple geometry optimization steps used here helped minimize this possibility. Finally, these dual ligand shell clusters were optimized to obtain the fully ligated systems. All together, a total of 44 clusters were used in this study 9 bare clusters, 13 Cl passivated clusters, 13 PH_3 passivated clusters, and 9 clusters with mixed ligand shells containing both Cl and PH_3 ligands.

The local magnetic moment atom i is given by the following equation.[181]

$$\mu_i = \int_0^R [\rho_\uparrow(r) - \rho_\downarrow(r)]dr$$

Where R is the radius of the augmentation sphere centered at atom i, and $\rho_{\uparrow}(r)$ ($\rho_{\downarrow}(r)$) is the majority (minority) spin density. The radius of the augmentation sphere in which the integration is preformed is chosen as half the bond length of the nearest neighbor bond length to ensure there is no overlap between atoms. The total magnetic moment of the system is given by the sum of each atoms local magnetic moment.

The total magnetic moment is calculated as an integral of the net spin density over all space. In an unrestricted calculation, the spatial components of the spin-up and spin-down wave functions can be different. Spatial mismatch results in regions of space where the net spin density is negative. In DFT, spin contamination is calculated as the integral of the net spin density over all space where the spin down electron density is greater than the spin up electron density.[202]

In order to characterize the local atomic structure of each cluster and correlate this structure with local magnetism of a given position in the cluster we utilize the coordination number of a given atom position extensively. Because the average Co-Co bond lengths are

different for each cluster, both as a function of size and ligand shell composition it is difficult to assign whether or not a bond exists between two atoms. To calculate coordination numbers consistently across each cluster, we calculated a fractional coordination number given below:

$$C_i = \sum_{j=1}^{N} C_{ij}$$

$$C_{ij} = \begin{cases} 1 & ,if\ r_{ij} \leq r_{eq} \\ exp\left(-\left(\frac{r_{ij} - r_{eq}}{\sigma}\right)^2\right) & ,otherwise \end{cases}$$

First we calculate every bond length between each pair of Co atoms less than 3.0 Å apart. From this set of bond lengths we calculate the average (r_{eq}) and the standard deviation (σ). The coordination number of atom i is given by equation 1, where we calculate the distance between atom i and atom j (r_{ij}), if this value is less than the equilibrium BL we add one to the coordination number, if it is greater than the equilibrium BL the value is weighted with a Gaussian distribution.

The ligand binding energy (LBE) of each Co_N (N = 15 - 55) cluster was calculated using the following equation.

$$LBE = E[Co_N(Lig)_M] - (E[Co_N] + M * E[Lig])$$

Where M is the number of ligands in the cluster. In cases where the ligand has an unpaired electron and is therefore not stable as a radical (i.e. Cl), the hydrogenated version of the ligand was used to calculated E[Lig] and the LBE was calculated with the following modified version of the above equation.

$$LBE = \left(E[Co_N(Lig)_M] + \frac{M}{2} * E[H_2]\right) - (E[Co_N] + M * E[Lig])$$

5.3 **Results and Discussion**

5.3.1 **Unpassivated clusters agree with experimental data**

First, we examine the electronic structures of Co clusters of various sizes in the absence of any capping ligands to validate our method against previous experimental and computational results as well as define a reference electronic structure to compare with ligand passivated clusters (*vide infra*). Figure 29A shows the core structures for each bare cluster used throughout this study after the initial DFT optimization. Atoms in these clusters are colored according to their Co-Co coordination number (CN). The coordination number of a Co atom without the presence of a ligand is known to play a primary role in determining the LMM of that position. As the CN of a Co atom increases, its local contribution to the particle magnetism decreases due to an increase in the width of the d-band of that atom (Figure 29B).[200] Additionally, the average bond length (BL) of the surrounding Co atoms in a given coordination environment plays a secondary role in Co atom LMMs. De Heer et al. provide a good description of the relationship between magnetic moment and d-band width.[200] Overall, the 9 bare Co_N nanocluster cores establish not only a range of cluster sizes, but also a range of surface atom coordination environments, from which to study the impacts of further ligand passivation.

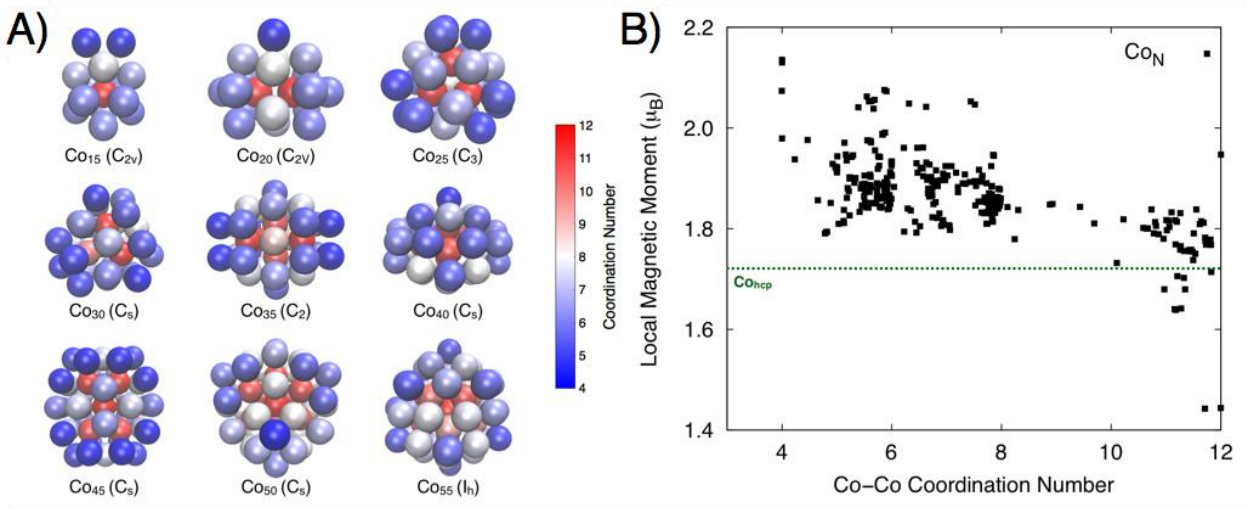

Figure 29. (A) Structures of each bare Co_N core used in this study. Color of each Co atom indicates the Co-Co coordination number of the atom. (B) LMM as a function of Co-Co coordination number for bare Co_N clusters. The horizontal line denotes the experimental value of the LMM per Co atom in a HCP lattice.

The Co_N nanoclusters considered show a progression from molecular to bulk electronic structure as size increases, but complete bands are not observed even for the largest clusters studied. Isosurfaces of orbitals for Co_{20} and Co_{45} in both the low and high energy regions of the d-band show this progression in Figure 30. As the energy of the orbital increases, the number of anitbonding interactions (nodal planes) between adjacent Co atoms also increases. As originally described by Hoffmann in language familiar to chemists,[203] bulk band diagrams can be qualitatively derived by considering the symmetries of the orbitals that make up the unit cell. By considering all phase combinations between infinitely many unit cells, a continuum of energy levels is created, which is called a band. For Co_{20} (a smaller cluster), the d-band is not yet fully continuous, however the d-states are arranged in qualitatively the same order as they would be in a bulk system (Figure 30A). Likewise, despite having a d-band closer to fully continuous, Co_{45}

shows the same progression from mostly in phase, to mostly out of phase arrangement of energy levels (Figure 30B). In general, the d-states in a Co_N cluster are arranged from mostly bonding to mostly antibonding interactions. However, the precise d-band nodal structure and energy level ordering is unique for each atomic packing arrangement and core symmetry.

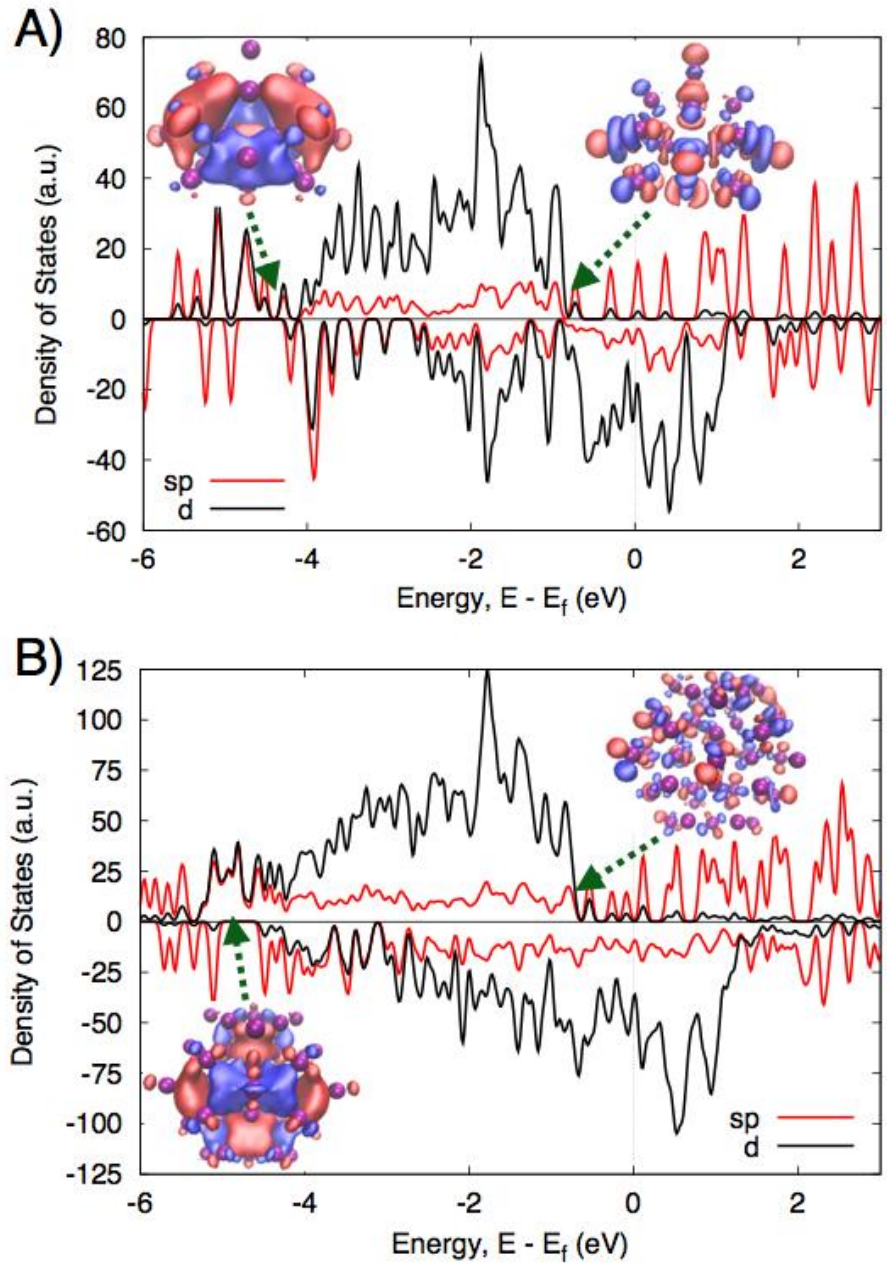

Figure 30. Total sp- and d-band density of states for bare (A) Co_{20} and (B) Co_{45} nanoclusters with orbital isosurfaces shown at low and high energy regions of their d-bands.

5.3.2 **Direct impact of ligands on LMM at the cluster surface**

As N increases from 15 to 55 atoms in unpassivated Co_N clusters, the average spacing between d-band energy levels decreases, suggesting a progression towards bulk-like electronic structure, yet across the core sizes chosen, we find little discernible size dependence in the average LMM per Co atom within this size range. We can understand this behavior as each different core size not only has a different percentage of surface atoms but also exhibits a unique distribution of surface atom coordination numbers.

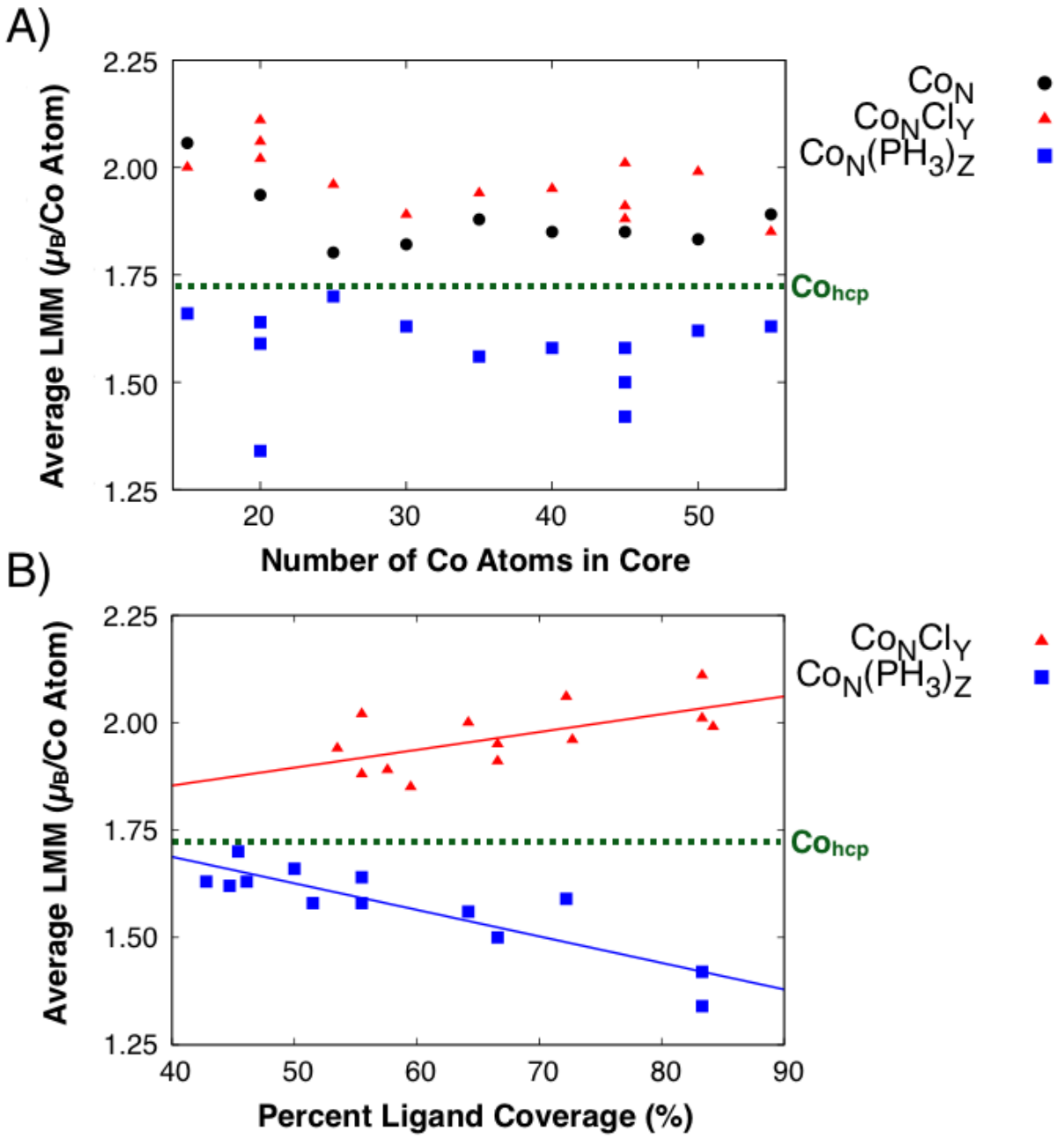

Figure 31. (A) Average LMM as a function of cluster size for each set of clusters considered. (B) Average LMM as a function of ligand coverage for Cl and PH_3 passivated clusters.

With a description of bare cluster geometries, electronic structure, and LMMs in hand, we build from these data to understand the impact of introducing a ligand shell. Figure 31A shows the relationship between average LMM per Co atom in each cluster as a function of the number of Co atoms in the clusters core, for each ligand shell considered. Each bare cluster lies above the bulk line due to the presence of under-coordinated surface atoms, and the introduction of a ligand shell leads to a change in LMM relative to the bare value of a given core size. Specifically, each cluster passivated with a chlorine ligand shell sees an enhancement in the average LMM per Co atom, while the introduction of a phosphine ligand shell quenches the magnetism of the clusters to values below the bulk value of 1.72 μ_B/atom.

While size dependent effects are not prevalent for either ligand shell composition in the nanocluster size range considered here, we do see a dependence of LMM on the percentage of the surface atoms interacting with a ligand. Specifically, we examine the impact of ligand coverage in two ways; by varying the number of ligands on the Co_{20} and Co_{45} cores, and by randomizing the percent ligand coverage across each other core size considered, effectively generating a distribution of percent ligand coverage across our suite of clusters. Percent ligand coverage is defined as the number of ligands divided by the number of atoms with coordination number ≤ 9, therefore if each surface atom has a ligand the percent coverage would be 100%. In Figure 31A, the 3 data points at core sizes of both 20 and 45 Co atoms represent 3 different ligand coverages studied on those cores. For both sizes, varying the percent ligand coverage leads to large differences in the average LMM on Co atoms in the core. Surprisingly, the range of LMM values observed within a single core is as large as the range spanned due to differences in the size of the core, indicating a significant, often dominant, role of surface ligands in the magnetic behaviors of these materials.

To quantify the impact of ligand coverage on the overall magnetism of Co_NL_M nanoclusters, we plot the average LMM per Co atom as a function of the percent ligand coverage for each system with a pure ligand shell (Figure 31B). In the case of each ligand type, there is a strong correlation between ligand coverage and resulting average LMM per Co atom in the core. However, the two different ligand binding types (X- vs L-type) lead to opposite trends. Increasing Cl coverage has an enhancing effect on the total magnetism of the cluster, where the line of best fit indicates that the LMM per Co atom is increasing by 0.0043 LMM/percent coverage. In contrast, increasing PH_3 coverage leads to a quenching of average LMM by 0.0065 LMM/percent coverage. Taken together, the deviations in average LMM as a function of ligand identity and coverage are evidence that the ligand coverage has a stronger impact on Co cluster LMMs than the size of the cluster within this size regime.

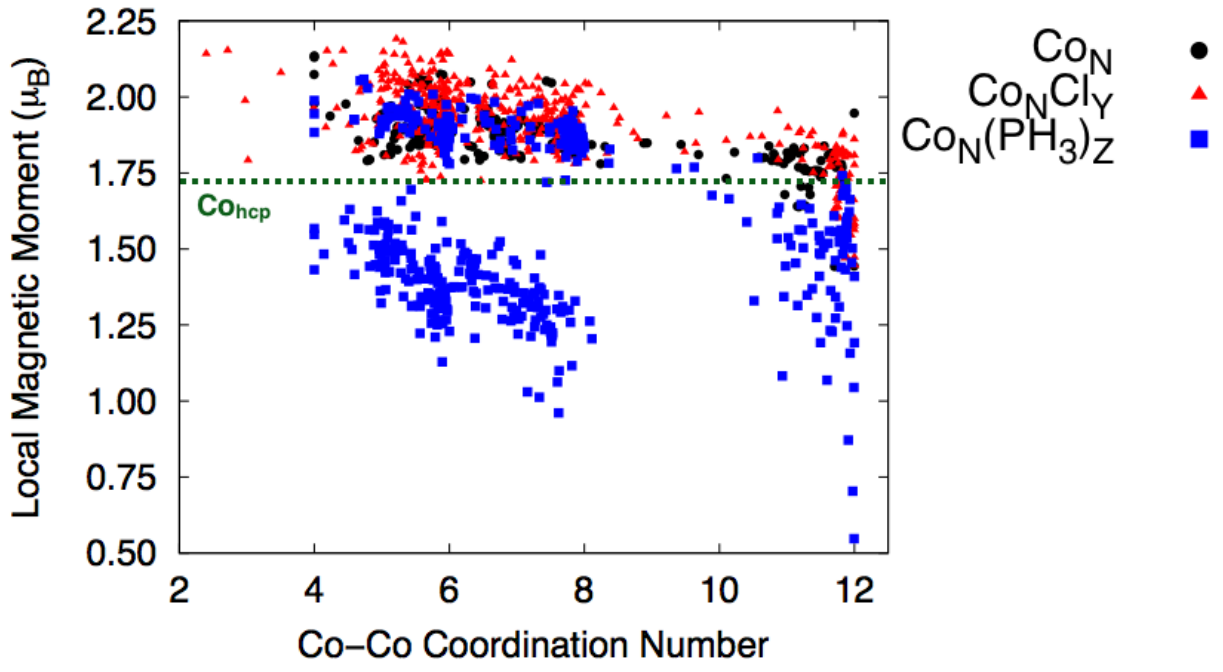

Figure 32. LMM as a function of Co-Co coordination number for every atom in Co_N, Co_NCl_Y, and $Co_N(PH_3)_Z$ clusters, respectively.

By systematically examining the influence of size and surface chemistry with DFT, we are also able to understand how the magnetic moment of the whole particle is distributed across each atom in the cluster. Specifically, we can correlate how local changes in atomic coordination environment lead to differences in the local electronic structure and therefore local magnetic moment. Further, we describe these trends by drawing parallels to metal-ligand bonding in classic coordination chemistry, which provides a useful formalism to understand how metal ligand hybridization on the surface of a nanocluster leads to specific magnetic behaviors. Figure 32 shows the LMM as a function of Co-Co coordination number for every atom in the Co_N, Co_NCl_Y, and $Co_N(PH_3)_Z$ sets of nanoclusters. The trends for the bare Co_N clusters (Figure 32, black circles) are consistent with what has been observed previously in gas phase studies of bare Co nanoclusters, where larger LMMs are observed for undercoordinated Co atoms (*vide supra*). As the Co-Co coordination number increases, the LMM decreases and approaches the bulk value of 1.72 μ_B/atom in the limit of full coordination (i.e. 12 surrounding Co atoms). Interestingly, a very similar behavior is found for the Co_NCl_Y clusters (Figure 32, red triangles). The noise in LMM relative to bare clusters is observed in the Co_NCl_X data due to the ligand introducing more disorder on the surface, but in general, a decrease in the LMM is observed as the Co-Co coordination number increases.

The clusters passivated with pure PH_3 ligand shells (Figure 32, blue squares) show that particular surface sites manifest magnetic behavior that is distinct from both the bare and Cl passivated Co_N clusters. In the atom-by-atom breakdown of the LMM vs. Co-Co coordination number for $Co_N(PH_3)_Z$ systems, two distinct trends emerge for the surface atoms ($CN \leq 9$). One of the trends overlaps well with that of the Co_N and Co_NCl_Y clusters and originates from the surface atoms that remain bare on the surface of $Co_N(PH_3)_Z$. The second trend below the bulk

line at 1.72 μB/atom clearly deviates from the bare and Cl-capped cluster results and emerges from surface Co atoms bound directly to a PH_3 ligand. Here, PH_3 ligands result in a direct quenching effect that increases quickly as the Co-Co coordination number increases. Importantly, the emergence of two divergent trends, even when considering atoms on the same nanocluster, suggests that the local Co coordination environment drives the LMM on the surface of the nanocluster. In addition to clusters with single component ligand shells, nanoclusters with both Cl and PH_3 ligands were studied. Although the structural diversity at the surface is much larger with these more realistic, dual ligand shell clusters, we find that the prevalence of the local coordination environment still determines surface magnetic moment. The primary difference arises from the added variety in surface structures resulting in a larger distribution of surface LMMs. (*vide infra*, Figure 34A).

To further explain the observed magnetic differences between clusters with different surface passivation schemes, we examine the local projected density of states resulting from hybridization of representative individual metal-ligand bonds of each type. In the center of Figure 33A, we plot an energy level diagram formed from the hybridization of a Cl ligand (left) and a bare Co core (right) constructed from the density of states of each component. There is little qualitative change in the d-DOS of the Co atom before and after the hybridization with Cl, consistent with the observation of a similar Co-Co coordination dependent trend between Co_N and Co_NCl_Y systems seen in Figure 32. The key difference between the Co_N and Co_NCl_Y systems comes from the manner in which Cl ligands hybridize across the entire d-band of the Co atoms in both spin channels. Inspection of the spatial extent of these states shows that the Co d-states maintain the original energy level spacing, ordering, and emergent band structure as the Co_N clusters, essentially remaining unaffected from Cl binding (Inset of Figure 33A). Because Cl is a

π-donating ligand, there is symmetry agreement between the dangling d-states and the bonding orbitals of the ligand. Additionally, the Cl bonding orbitals are aligned in energy with the d-band edges of Co, allowing for optimal hybridization. Since the Cl does not directly change the distribution of states originating from atomic d-orbitals, the magnetism remains primarily unaltered. The slight enhancement seen in the Co_NCl_Y clusters relative to Co_N clusters is from a slight magnetic moment on the Cl atom itself due to matching the occupation difference between spin channels of the Co d-states.

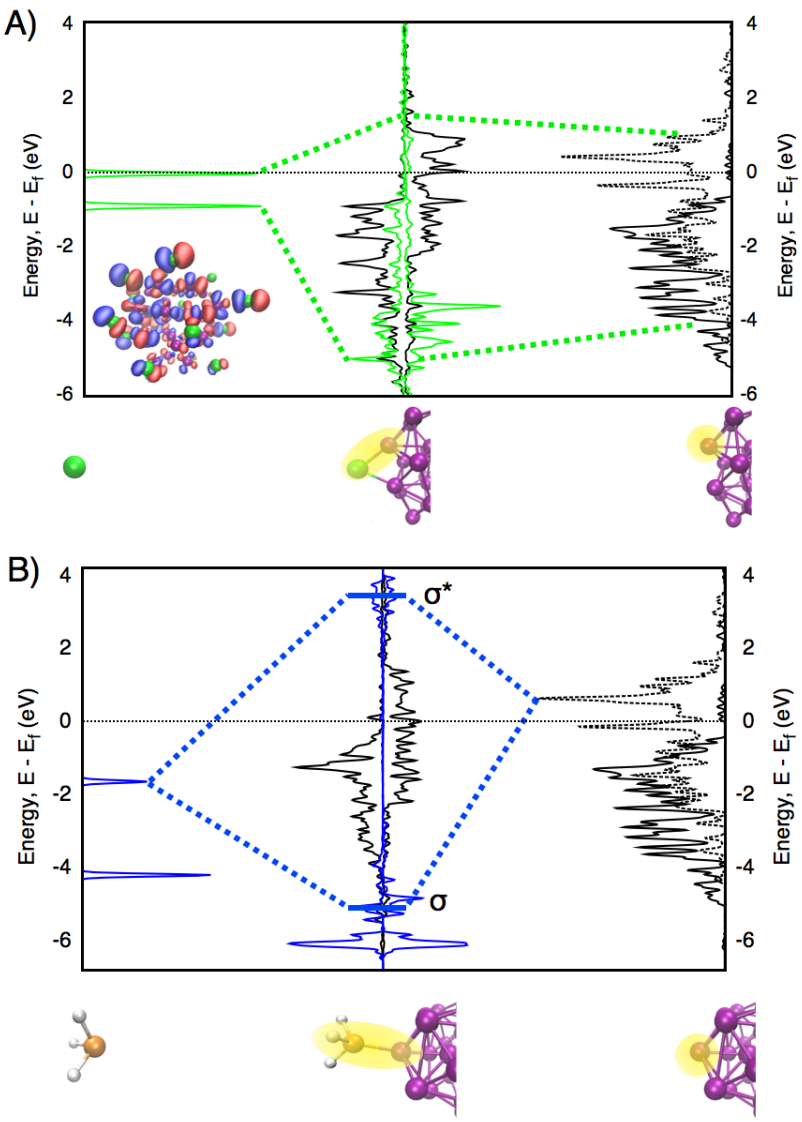

Figure 33. Molecular orbital diagram illustrating the bonding between a bare Co_N surface and Cl ligand (A) or a PH_3 ligand (B). In both cases, the d-DOS from a surface atom on the Co_{30} core is used (solid line is spin up DOS, dotted line is spin down DOS). Center plot for both (A) and (B) has spin up down states left (right) of vertical axis. (Inset) Isosurface of spin down HOMO of $Co_{30}Cl_{15}$ system.

In contrast to the Cl case, the σ-donating PH_3 ligand hybridizes directly with the Co_N surface to form a more traditional dative bond, resulting in a bonding-antibonding pair of surface states (Figure 33B). Since PH_3 is an L-type ligand and provides both electrons to the bond, the Co_N states that participate in the bond come from the unoccupied, spin down states just above the Fermi level. Population of an unoccupied state in bare Co_N, balances out the relative occupation of the two spin channels and induces a net quenching of the LMM at the surface Co atom.

The electronic structure of the bonding interactions of the Co_NCl_Y and $Co_N(PH_3)_Z$ clusters each mirror bonding motifs observed in quantum dots (QD). In the case of phosphine-terminated Co_N clusters, the bond formed between PH_3 ligands and a Co_N cluster surface, demonstrated here for Co_{30}, is a common motif found on the surface of many small nanoparticle systems. For instance, ligand bonding with the surface of quantum dots shows strikingly similar bonding behavior, where a ligand bonding orbital in the mid-band region of the quantum dot will hybridize with the lowest energy unoccupied states when it forms a bond with the surface. In quantum dots, the lowest energy states available are often mid-gap or trap states, meaning ligand bonding results in the 'cleaning' of the band gap of traps, often observed by increasing photoluminescence quantum yield after ligand binding. In the case of Co nanoclusters, the PH_3 HOMO is aligned in the middle of both the spin up and spin down d-bands of Co_N. Since there is a near continuum of states near the Fermi level, no dramatic optical effect from near Fermi level transitions should be observed, however a population of low lying unoccupied states from the Co_N core leads to a quenching of local magnetic moments at the surface.

Likewise, the resulting electronic structure from Co-Cl hybridization in Co_NCl_Y clusters is similar to other bonding motifs seen in QDs, where delocalization of electron density across the nanocrystal core-ligand interface is observed. Weiss et al. have shown that certain ligands

can increase the excitonic radius of a QD without directly changing the size of the nanocrystal core.[204] This interfacial wave-function delocalization behavior in QDs occurs when the symmetry of the ligand binding orbital matches that of the band it is hybridizing with, and when the binding orbital from the free ligand is aligned in energy with the valence band of the QD.[205] In Co_NCl_Y nanoclusters, the Cl ligand reproduces these two conditions when passivating Co_N nanoclusters, where there is a π-symmetry match between Cl binding orbitals and the dangling d-states on the surface of Co, as well as an energy alignment in both spin channels. Interestingly, the appearance of wave-function delocalization across a nanocrystal-ligand interface leads to a minimal impact on the LMM, indicating that the impact of such a behavior is dependent on the property considered.

5.3.3 **Impact of multiple component ligand shells on the magnetic properties of Co_N nanocluster cores**

Many synthetically accessible nanoclusters with fewer than 100 metal atoms contain multiple component ligand shells, where each type of ligand is important for the stability of the nanocluster.[206-208] Structural diversity on the surface often arises due to the presence of many components in the solution at the time of nucleation, and a high energy surface that can bind to many different ligands in order to increase both thermodynamic and kinetic stability. To extend our work toward more realistic model systems, we built a set of clusters with both Cl and PH_3 ligands present. The Cl ligands were added to bare surface sites of the $Co_N(PH_3)_Z$ set of ligands and subsequently reoptimized. Overall, 9 $Co_NCl_Y(PH_3)_Z$ clusters were considered and together, 7 unique surface coordination environments were generated by the ligand shell after optimization (Figure 34A). Here a unique environment was defined as either having a coordination number to

each Cl and PH_3 ligands (i.e. $1Cl/1PH_3$ vs. $2Cl/PH_3$), or as having the coordinating ligand binding to a different number of surface atoms (i.e. direct binding vs. bridging 2 Co atoms).

In bare clusters and single component ligand shells, we find a clear correlation between the composition of the immediate coordination environment at a surface Co atom and its LMM, allowing us to isolate the role the ligand plays on the electronic structure at the surface. Consistent with these observations with single component ligand shells, as the Co-Co coordination number increases in the dual component ligand shells a general quenching of the LMM is observed, independent of the ligand coordination. However, coordination environments containing both Cl and PH_3 ligands present show LMMs that fall between what is expected based on results form single component ligand shells. LMM averaging leads to the total magnetic moment of the dual ligand shell clusters falling between that of the pure Cl and PH_3 ligand shells for a given core size (Figure 34B). Importantly, the $Co_NCl_Y(PH_3)_Z$ clusters does not qualitatively differ from the pure ligand shells, where no size dependent evolution of magnetism is observed. The lack of size dependence indicates that the local coordination environment remains the determining factor in the LMM in complex ligand shells, and the set of coordination environments on a given nanocluster determines the overall magnetism of a given system.

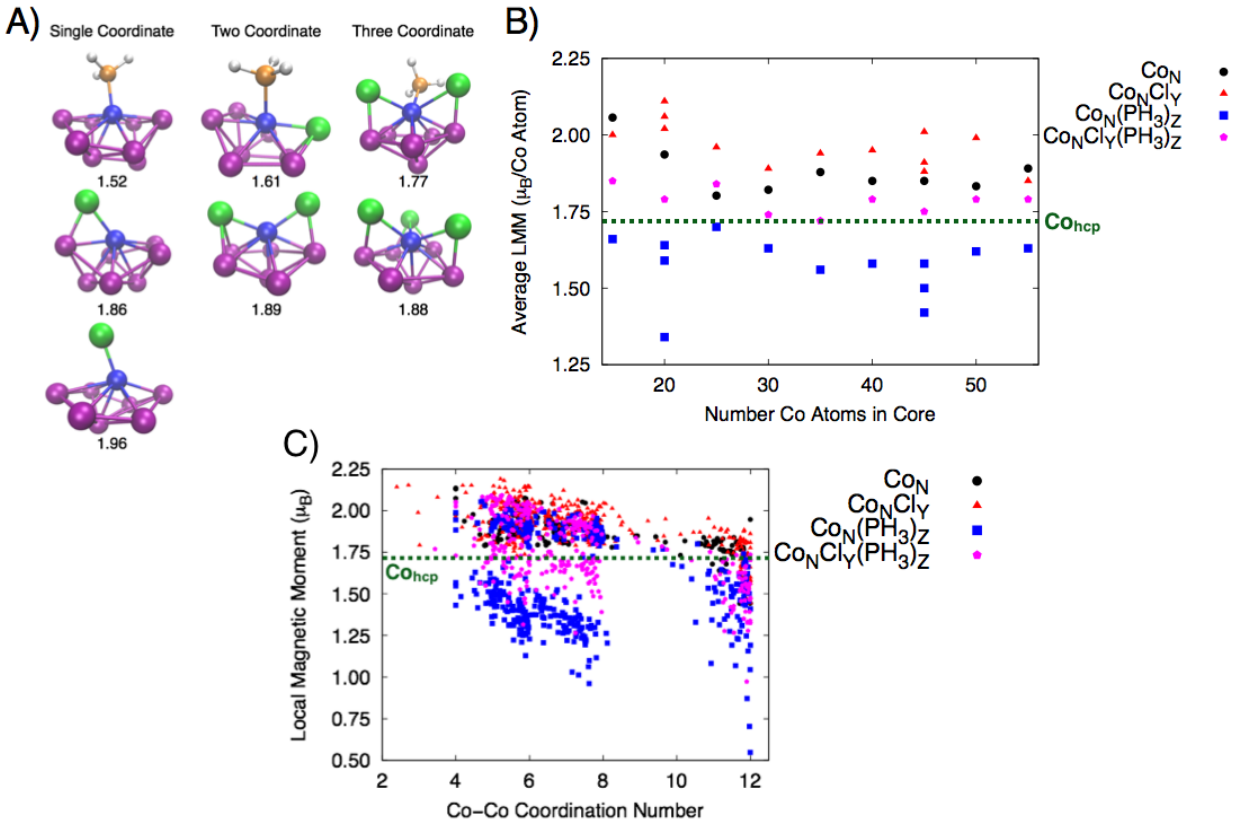

Figure 34. (A) Each unique local structural motif generate from ligand shells in $Co_NCl_Y(PH_3)_Z$ clusters. The number below each structure indicates the LMM of the center of the coordination environment (blue atom). (B) Average LMM on each Co atom as a function of the number of atoms in the core of each cluster considered including dual ligand shell systems. (C) LMM as a function of Co-Co coordination number for ever atom in each cluster considered in this study.

5.3.4 **Long-range impact of ligand on subsurface LMM**

In bare Co_N clusters, the CN on the surface dictates the LMM at a given site, where in the core, a quick convergence to bulk like LMM values is observed when the CN approaches 12. Figure 35A shows the relationship between subsurface LMM and ligand coverage of the surface adjacent to a given subsurface Co atom. Here, ligand coverage of the surface adjacent to a subsurface Co atom is defined with a similar CN described above. However, in order to select for nearby ligands, the equilibrium bond length is taken to be the sum of the average Co-Co bond and a Co-ligand bond. The subsurface LMM covers a significant range, where values from almost 2.00 μ_B/atom down to 0.53 μ_B/atom are observed, even at nearly identical coordination numbers. Subsurface LMM quenching is particularly strong in the $Co_N(PH_3)_Z$ nanoclusters, and interestingly, increases with higher concentrations of nearby ligand. This quenching behavior indicates that the PH_3 ligand has a long-range perturbative effect on the LMM. In other words, the PH_3 ligand influences the LMM of atoms to which it is not directly bound.

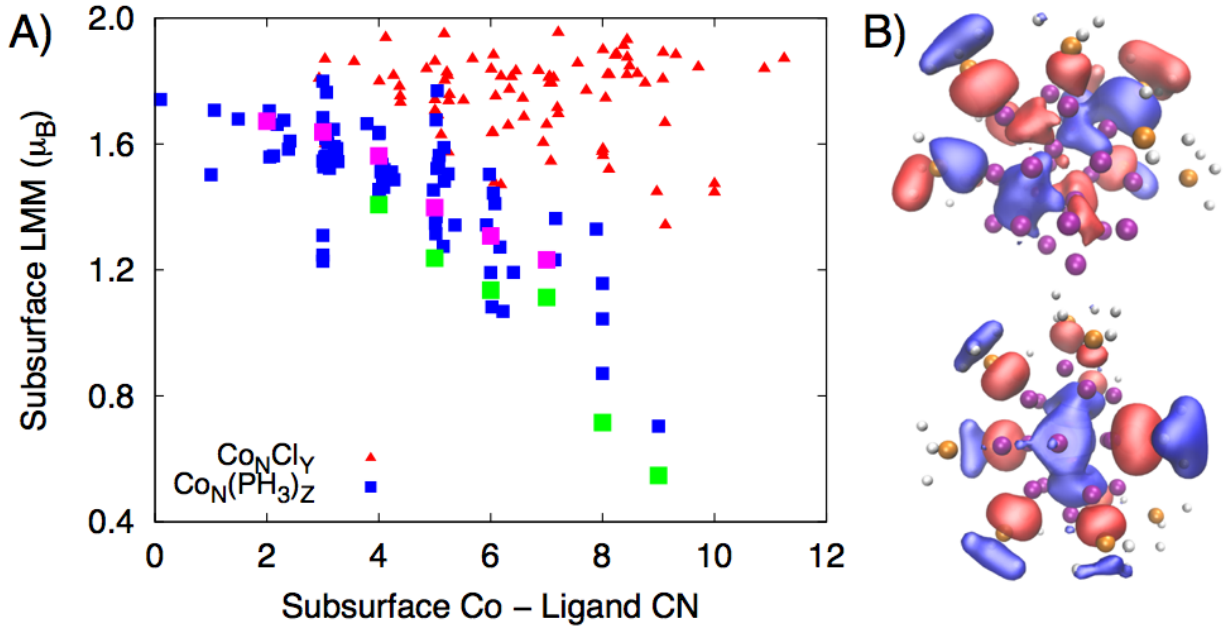

Figure 35. (A) LMM as a function of subsurface Co-Ligand coordination number for every subsurface atom in Co_NCl_Y and $Co_N(PH_3)_Z$ cluster (green/pick points represent systematic removal of ligands, see text for further description). (B) Spatial extent of orbital with linearly hybridized states extended from the PH_3 ligand to the subsurface of the $Co_{25}(PH_3)_{10}$ cluster.

The nature of the Co-ligand bond described above provides insight into why the two ligand types induce different subsurface quenching trends. Because the Cl ligand simply hybridizes with the d-band of Co, it provides a relatively small perturbation on both short and long-range interactions throughout the cluster. On the other hand, PH_3 ligands form bonding-antibonding hybrid orbital pairs when anchored on a Co surface. Figure 35B shows the spatial extent of two orbitals that extend from the subsurface to the ligand and head group for the $Co_{20}(PH_3)_{10}$ cluster. In each case, the orbital has significant amplitude at the subsurface atom, which leads to a net quenching of the LMM at the subsurface position. As more and more PH_3's bind to the surface surrounding a subsurface atom, the more of these linear hybrid states exist, systematically quenching the LMM at the subsurface.

To show that the LMM quenching at the subsurface was controlled by the ligand coverage of the immediate surface, we chose two subsurface atoms and systematically removed ligands that are thought to quench their LMM. The green and pink points in Figure 35A represent a single subsurface atom in the $Co_{20}(PH_3)_{15}$ and $Co_{45}(PH_3)_{30}$ clusters respectively. This data was generated by systematically stripping ligands two bonds away from the subsurface atom of interest and recalculating the LMM. In the case of both small (Co_{20}) and large (Co_{45}) cluster cores, the LMM at the subsurface increases monotonically as the number of ligands two bonds away decreases, suggesting this long-range binding is the main driving force for the quenching of the subsurface LMM in PH_3 terminated clusters.

Finally, we note that finite size effects intrinsic to each nanocluster core play a role in the range of LMMs accessible in these nanoclusters. First, linear strings of atoms from the ligand head group down to the subsurface emerges from regions of the surface with local 5-fold symmetry, reminiscent of icosahedral symmetry. In bulk hcp Co, subsurface Co atoms are offset

relative to the surface Co atoms, preventing this specific atomic arrangement. Second, the size of these clusters leads to high curvature of the surface, allowing the number of ligands that pack around a subsurface atom to be much higher than on a flat surface. For example, we calculated subsurface Co to ligand coordination numbers up to 9 for PH_3 ligand shell and 11 for Cl ligand shells. As the surface curvature decreases, the maximum number of ligands two bonds away from a subsurface Co atom will decrease, limiting the range of accessible LMMs at the subsurface. Together, structural parameters specific to a nanocluster of interest are essential to fully understand the distribution of local magnetic moments throughout a Co_N nanoclusters, and therefore the emergence of specific magnetic behaviors in a cluster.

5.4 **Conclusion**

In summary, the total magnetism of a Co_NL_M nanocluster is not linearly correlated with size; instead the distribution of local coordination environments throughout a give cluster must be known. The local magnetic moment of a give coordination environment is dependent on both the Co-Co CN and the overall composition of the coordination environment. On the surface of a Co_NL_M nanocluster, molecular descriptors of ligand binding known from coordination chemistry are useful to predict the impact of ligands on the LMMs of surface Co atoms, and describe how the LMM will differ relative to a bare Co atom with the same Co-Co coordination number. In the core of a Co_NL_M nanocluster, hallmarks from band structure dominate the LMM, where Co-Co CN is the primary factor in determining LMM. However, certain ligands have long-range quenching effects despite not being directly bound. Overall, knowing the collection of coordination environments in a Co_NL_M nanocluster can lead to the prediction of both their size

and coverage dependent magnetic behavior. Give the important and pervasive role of a ligand in the synthesis and performance of nanocluster, the immense structural complexity possible in Co nanoclusters, these materials are an exciting class of targets for discovery and enhancement of magnetic materials.

6.0 Finite Temperatures Improve Excitation Energies in Configuration Interaction Singles

(Portions of this work are being prepared for submission as Hartmann, M. J.; Lambrecht, D. S. **2018**, in preparation.)

6.1 **Introduction**

Configuration interaction singles (CIS) is the simplest and computationally least expensive wave function based *ab initio* method to calculate electronic excitation energies.[209] CIS extends Hartree-Fock (HF) to excited states, where the wave-function is generated by a linear combination of single excitations relative to the HF reference determinant. Quartic scaling of computational cost with system size allows CIS to be applied to relatively large systems. Additionally, combining with ideas such as a fragment product ansatz enables expedited calculations due to exploiting sparsity that makes application to several hundred atoms possible.[210-211] In addition to its moderate computational scaling, CIS is an attractive entry level method because it is variational and qualitatively includes the correct -1/r long-range behavior for the exchange potential in the asymptotic limit.[212] The primary drawback of CIS, even for weakly correlated systems where HF is qualitatively correct, is that it overestimates excited state energies because orbital optimization is biased toward the self-consistent field (SCF) arising from the occupied orbitals, limiting the accuracy of CIS predictions involving 'excited'

determinants.[213-216] Including excited state determinants in the Hartree-Fock potential in which the orbitals are optimized could lead to a better simultaneous description of the ground and excited states, and improve the accuracy of excitation energies calculated with CIS. This would enable more quantitative, computationally efficient CIS-type predictions of large scale, experimentally interesting systems.

Capturing excited-state effects at the mean field level has been studied for a long time;[217] some more recent examples include Neuscamman's excited-state mean field theory[218] or Subotnik's orbital-optimized CIS.[219] In this study we utilize fractional occupation numbers (FON) in the one-particle density matrix (1-RDM) to include virtual orbitals into the mean-field description to generate a new set of orbitals for use in a CIS calculation to improve the accuracy of excitation energies. Utilizing FON allows us to optimize the SCF orbitals, which, by construction are relaxed within a field arising from a linear combination of 'ground state' and 'excited' determinants, and thus improve the quality of the one-particle basis for describing excited states (vide infra). Methods employing fractional occupation numbers have been applied successfully within quantum chemistry, for example to accelerate mean field convergence for systems with small HOMO/LUMO gaps.[220] Moreover, FON approaches have been used to target specific shortcomings of electronic structure approaches, such as mitigating self-interaction error to improve band gaps predicted by pure density functional theory,[221-222] or to include static correlation in DFT functionals via thermally assisted occupation DFT.[223-224] Finally, FON based methods have also been used in wave function based method, for example to approximate orbital relaxation so that CASCI orbitals can yield CASSCF quality results without the need for explicit orbital optimization.[225-226]

Our approach takes an empirical route to improve excited state mean field effects, where we use the electronic temperature in the Fermi-Dirac occupation number distribution similar to a variational parameter to modify the 1-RDM in the SCF cycle. We then use this parameterized HF density to obtain optimized orbitals and orbital energies for use in subsequent CIS calculation (FON-CIS). This FON-CIS approach shows a dramatic improvement in calculated molecular transition energies with small computational overhead compared to CIS.

6.2 **Theoretical Approach**

The proposed FON-CIS approach is simple and can be easily incorporated into existing electronic structure codes. In HF, the one-electron Fock operator, $\hat{f}(\alpha)$ is defined as the sum of the core Hamiltonian operator, $\hat{h}(\alpha)$ and the effective one-electron HF potential,

$$\langle \phi_p(\alpha) | \hat{f}(\alpha) | \phi_q(\alpha) \rangle = h_{pq} + V_{pq}^{HF}$$

The HF potential is composed of Coulomb and exchange terms:

$$V_{pq}^{HF} \equiv \langle \phi_p(\alpha) | \hat{V}^{HF}(\alpha) | \phi_q(\alpha) \rangle = \sum_{i=1}^{N_{occ.}} [2(ii|pq) - (iq|pi)]$$

shown here, without loss of generality, for a restricted closed-shell calculation. From this equation it is evident that the HF orbitals are optimized in response to Coulomb- and exchange-type interactions exclusively with the occupied space (j = 1…N_{occ}), that is, interactions excluding virtual (unoccupied) orbitals. This treatment is consistent within standard ground-state predictions, where interactions with the occupied space are included at the mean-field level.

Additionally, the standard HF energy from this approach can be written as the sum of occupied MO eigenvalues (ε_i) minus coulomb and exchange integrals that account for double counting:

$$E_{HF} = \sum_{i}^{Nocc} \varepsilon_i - \frac{1}{2} \sum_{i}^{Nocc} \sum_{j}^{Nocc} \langle ij \| ij \rangle$$

Finally, the CIS energy for an excitation between occupied orbital i and virtual orbital a can be written as the sum of the HF energy and the MO's of and coulomb and exchange integrals between initially occupied and virtual orbitals participating in transition.

$$E_{CIS} = E_{HF} + \sum_{ia} (t_i^a)^2 (\varepsilon_a - \varepsilon_i) + \sum_{ijab} t_i^a t_j^b \langle aj \| ib \rangle$$

This approach inherently treats virtual orbitals on a different footing, because they do not enter the HF potential, yet the MO eigenvalues of the virtual orbitals participating in the transition do enter the Hartee-Fock potential. The FON formalism allows these virtual orbitals to be included in the HF potential and therefore contribute to the SCF in which the orbitals are optimized. In FON, all orbitals are allowed (including conventionally occupied and virtual) to have non-zero, non-integer occupation numbers as follows:

$$\langle \phi_p | \hat{V}_{FON}^{HF} | \phi_q \rangle = \sum_{i=1}^{N_{all}} n_i [2(ii|pq) - (iq|pi)]$$

shown here again, without restriction of generality, for a closed-shell calculation. Here, n_r is the occupation number of molecular orbital r, determined by a Fermi-Dirac distribution:

$$n_i = \frac{1}{1 + exp\left(\frac{\epsilon_i - \epsilon_f}{kT}\right)}$$

In the Fermi-Dirac distribution above, T is the electronic temperature, k is the Boltzmann constant, and ε_f and ε_r are the Fermi energy and energy of eigenvalue of orbital r, respectively.

While the total number of electrons in the system is conserved, n_r can be fractional ($0 \leq n_r \leq 1$), allowing the sum runs over all molecular orbitals ($r = 1 \ldots N_{all}$), and each term is weighted by the fractional occupation number n_r. Analogous to above, the ground state energy with FON can be written as:

$$E_{HF}^{FON} = \sum_{i}^{N} n_i \varepsilon_i - \frac{1}{2} \sum_{i}^{N} \sum_{j}^{N} n_i \langle ij \| ij \rangle$$

While E_{HF}^{FON} will be higher than the standard HF energy due to mixing the HF ground state with higher energy HF solutions, the CIS energy is now a functional of the occupation number distribution. This allows the CIS energy to be optimized with respect to temperature:

$$E_{CIS}^{FON} = E_{HF}^{FON} + \sum_{ia} (t_i^a)^2 \big(\varepsilon_a(T) - \varepsilon_i(T)\big) + \sum_{ijab} t_i^a t_j^b \langle aj \| ib \rangle$$

Here, ε_a and ε_i depend on the electronic temperature parameter and provide a handle on the CIS energy. Overall, FON-CIS adds two important parameters to the conventional integer-occupation HF ansatz: 1) orbitals are optimized including mean-field interactions with the entire (occupied plus virtual) orbital space, and 2) the 'electronic temperature' parameter T provides a parameterization to control the relative weights with which different orbitals enter the HF potential. We utilize this flexibility gained by the FON ansatz to control the HF potential to yield orbitals resulting in more accurate excitation energies within FON-CIS.

Specifically, we employ the electronic temperature of the FON method as a parameter to optimize specific sets of CIS transition energies. We tested the FON-CIS ansatz on a range of systems; here we present results for a test set of representative π-conjugated molecules as well as the formaldehyde-water dimer sampled for several local minima plus geometries sampled from molecular dynamics simulations. By analyzing the temperature dependence of the FON-CIS

excitation energies, we improve the predicted transition energy at the CIS level of theory relative to benchmark equation of motion coupled cluster singles and doubles (EOM-CCSD) calculations and suggest a simple principle to select the optimal temperature *a priori*.

The FON-CIS was implemented into a development copy of the Q-Chem version 4.0 program package.[227] Throughout this study, each system's geometry was optimized at the Hartree-Fock level of theory within the cc-pVDZ basis set.[228] The optimized structures were then used to calculate the first ten singlet excited states with CIS, FON-CIS, and EOM-CCSD. The formaldehyde-water structures were generated along three separate *ab initio* molecular dynamics (AIMD) trajectories, where each trajectory was initiated with one of three local geometry minima structures predicted for the H_2CO-H_2O system.[229] The AIMD simulations were performed at the HF/cc-pVDZ level, at a temperature of 300K, and were allowed to run for 2000 MD steps with a time step of 15 atomic units. Starting with the 50^{th} step, the geometries were sampled at every 30^{th} step along each trajectory, resulting in 65 geometries for each initial structure (195 total geometries).

6.3 **Results and Discussion**

Figure 36 shows the energy of the HOMO-LUMO transition of 1,3-butadiene calculated with FON-CIS as a function of electronic temperature. The CIS value for the HOMO-LUMO transition of 1,3-butadiene is 6.84 eV, which is overestimated by nearly double relative to the EOM-CCSD value of 3.52 eV. Using FON-CIS, the transition energy can vary from the CIS value, across the EOM-CCSD value, to 1.58 eV as a function of electronic temperature. The FON-CIS value matches EOM-CCSD between 48,000K and 50,000K.

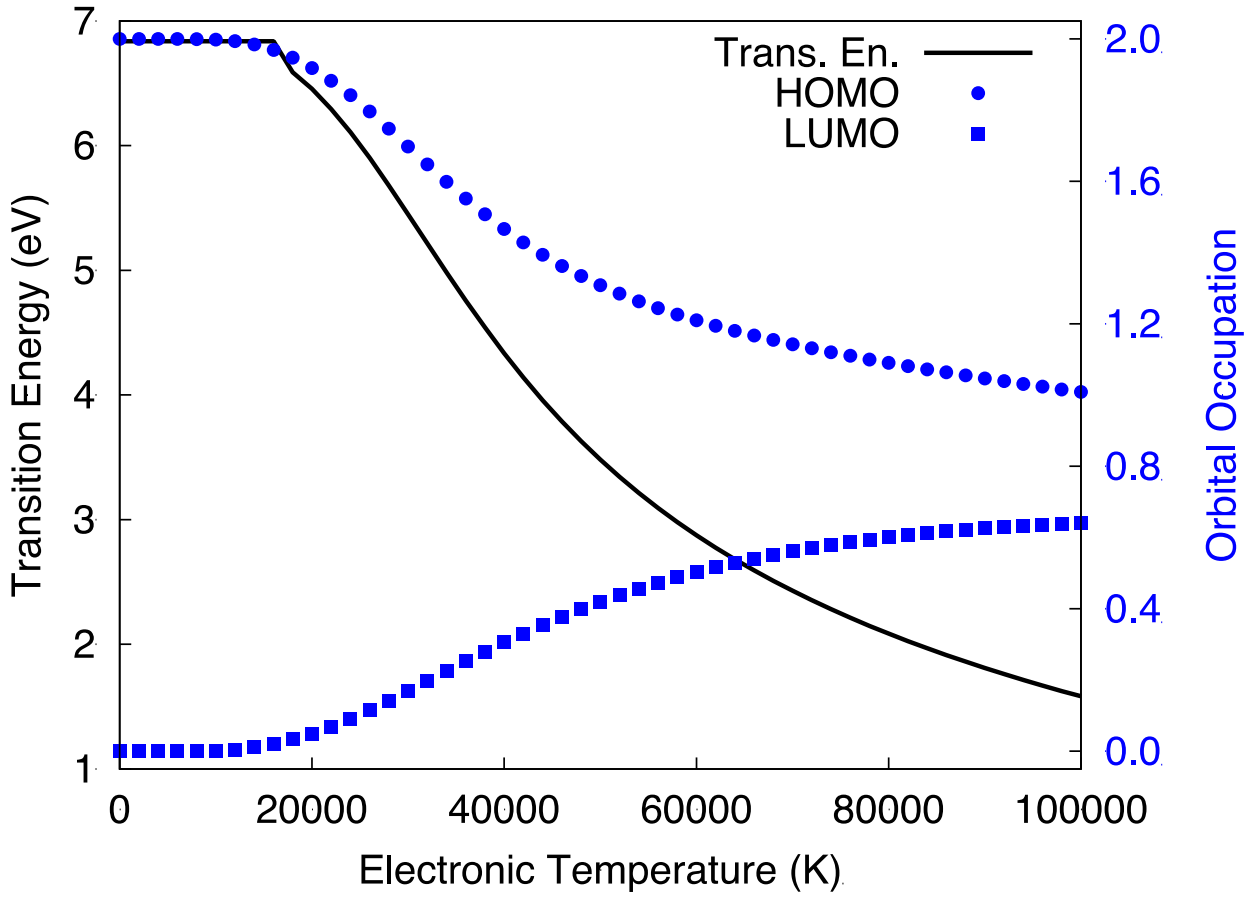

Figure 36. FON-CIS transition energies and frontier orbital occupation numbers as a function of temperature for 1,3-butadiene. Black line represents transition energy; blue circles (squares) are HOMO (LUMO) occupation numbers at each temperature.

As a function of temperature, the FON-CIS transition energy curve exhibits three distinct regimes that are defined by the occupation number distribution between the participating orbitals. Specifically, the low temperature regime (0K $\leq$ T $\leq$ 16000K) for 1,3-butadiene is defined by no change in transition energy and negligible change in the occupations of the HOMO and LUMO. As the temperature increases above 16,000K, occupation transfer from the HOMO to the LUMO begins, and a decrease in the HOMO-LUMO transitions energy is observed. We find that relatively small occupation number transfer is required before changes in the transition energy are observable, where the change in HOMO occupation is reduced by 0.03 electrons at 18,000K relative to 0K. In this intermediate temperature range (18,000K $\leq$ temperature $\leq$ 40,000K for 1,3-butadiene) the change in transition energy is sensitive to increasing temperature and responds nearly linearly as temperature increases. The near linear change in transition energies is mirrored by a similar linear change in occupation numbers of the HOMO and LUMO. A monotonic decrease in transition energy continues in the high temperature regime, above 40,000K for 1,3-butadiene, however the change is less sensitive to temperature and the curve flattens at high temperatures. In the high temperature regime, the HOMO and LUMO occupation numbers also flatten due to many lower and higher lying orbitals other than the frontier orbitals undergoing occupation number changes. Overall, our data suggests that the occupation of the HOMO and LUMO directly correlate to HOMO-LUMO transition energy of 1,3-butadiene predicted by FON-CIS. More broadly, the occupations of the HOMO and LUMO orbitals modify the HF potential in which the orbitals are formed via the density matrix, thus controlling the energy of the HOMO-LUMO transition.

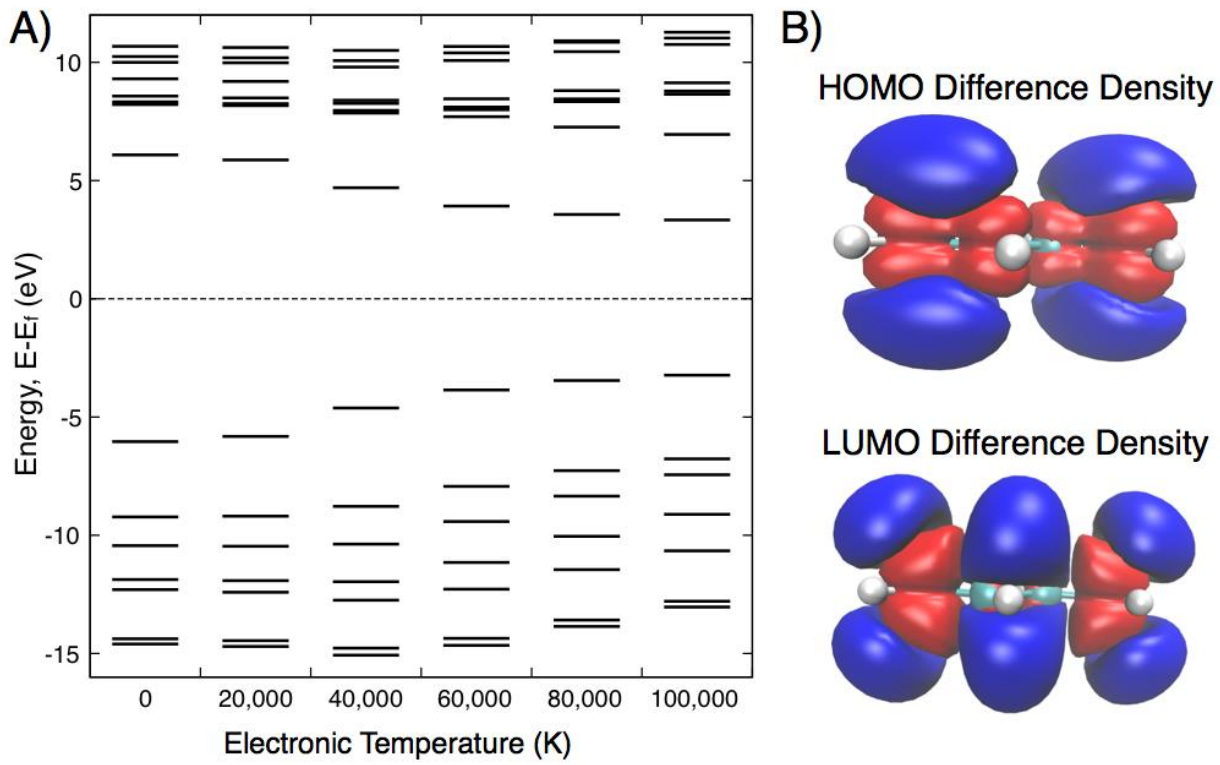

Figure 37. (A) Orbital energy level diagram of 1,3-butadiene at various temperatures. (B) Difference density of frontier orbitals between 0K and 100,00K. Blue surface shows where 0K orbital amplitude is larger, red surface shows where 100,000K orbital amplitude is larger.

Occupation number changes directly modify elements of the atomic orbital (AO) basis density matrix by changing the prefactor of each molecular orbital coefficient: $P_{\mu\nu}^{AO} = \sum_{r=1}^{N_{all}} n_r \, C_{\mu r}^{*} C_{\nu r}$. In addition to changing the values of the matrix elements in the density matrix, there are more non-zero entries along the diagonal of the molecular orbital (MO) basis density matrix $D_{pq}^{MO} = n_p \delta_{pq}$ due to population of the virtual orbitals. The combination of these two changes to the density matrix with FON directly impacts the HF potential by changing both the number of integrals and values of the Coulomb and exchange integrals. As a consequence, the FON ansatz modifies SCF results, that is, orbital energy eigenvalues, the orbital coefficients and densities, and thus also the shape of the orbitals. Normally, the HOMO is low and the virtual orbitals are too high due to not being included in the SCF optimization. Upon introduction of fractional occupation numbers, we optimize with respect to a superposition of configurations, causing HOMO to increase and the LUMO to decrease in the energy. In Figure 37B we also show the difference between the squared amplitudes of the HOMO and LUMO between the 0K and 100,000K temperatures (blue – larger amplitude at 0K, red – larger amplitude at 100,000K). In both the HOMO and LUMO, a localization of the electron density is observed with increasing temperature.

From the above description, it is clear that the role of temperature in the FON-CIS method is to introduce a non-linear parameterization of the mean field electron density. In order to make the FON-CIS a practical and routine method to calculate transition energies with improved accuracy relative to standard CIS, the optimal temperature parameter should be made *a priori*. Here, we propose to employ the transition energy at the inflection points of the temperature vs. occupation number curve as a practical choice for the FON-CIS predicted transition energy. The rationale for this choice is that as occupation is transferred from occupied

to virtual orbitals, the extent of their contribution to the HF potential is also transferred, including contributions from excited configurations. The inflection point represents an averaged configuration at which an equal treatment of the orbitals participating in the transition is reached. For 1,3-butadiene, the FON-CIS transition energy at the inflection point predicts an excitation energy of 4.51 eV (cubic fit in Figure 38, a 28% overestimation of the EOM-CCSD result, a significant improvement from the 94% overestimation produced by standard CIS. To demonstrate the transferability of the inflection point as a good choice for the FON-CIS excitation energy, we applied this method to a suite of straight chain, π-conjugated hydrocarbons (Figure 39).

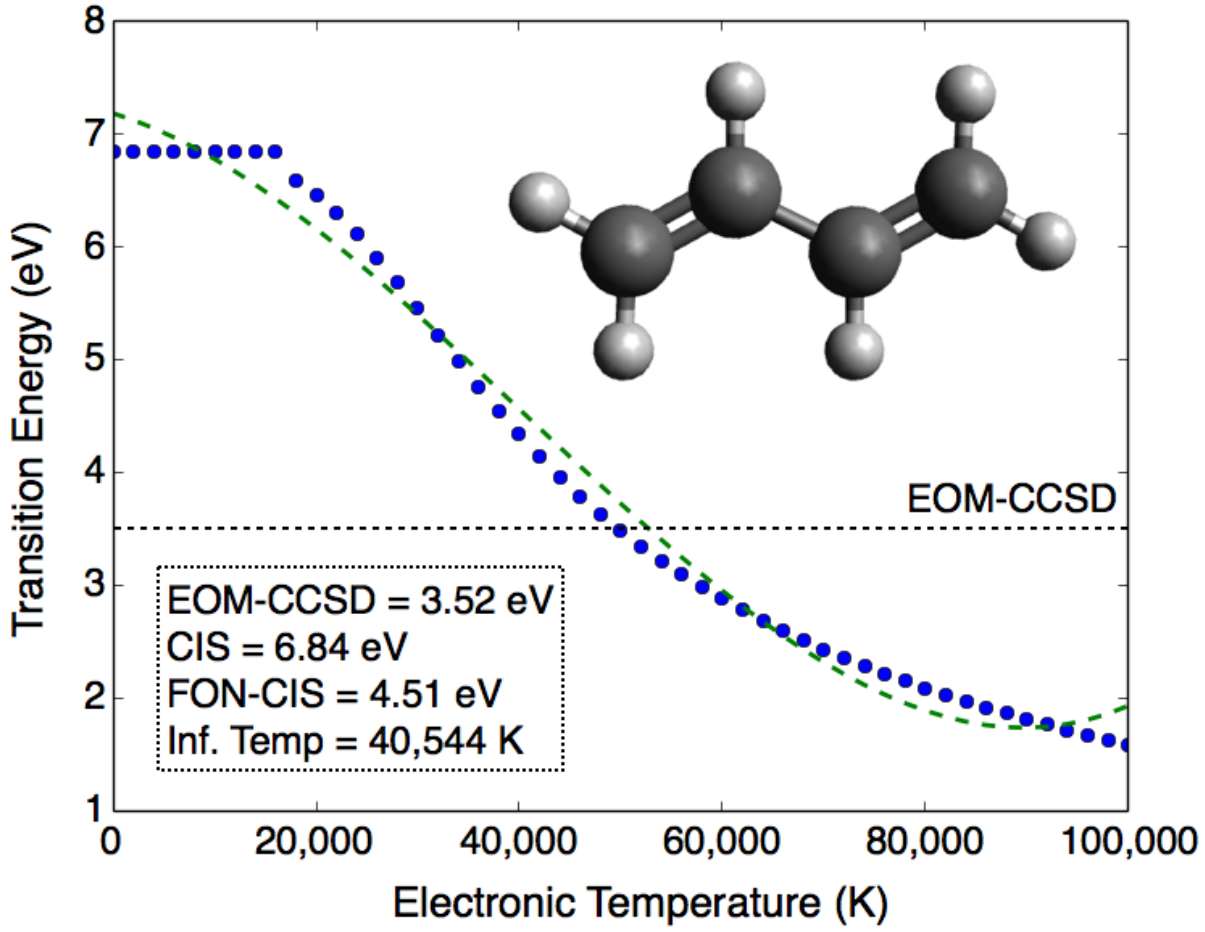

Figure 38. Transition energy as a function of temperature for 1,3-butadiene (blue circles) and cubic polynomial fit (green line). Horizontal dashed line represents EOM-CCSD value.

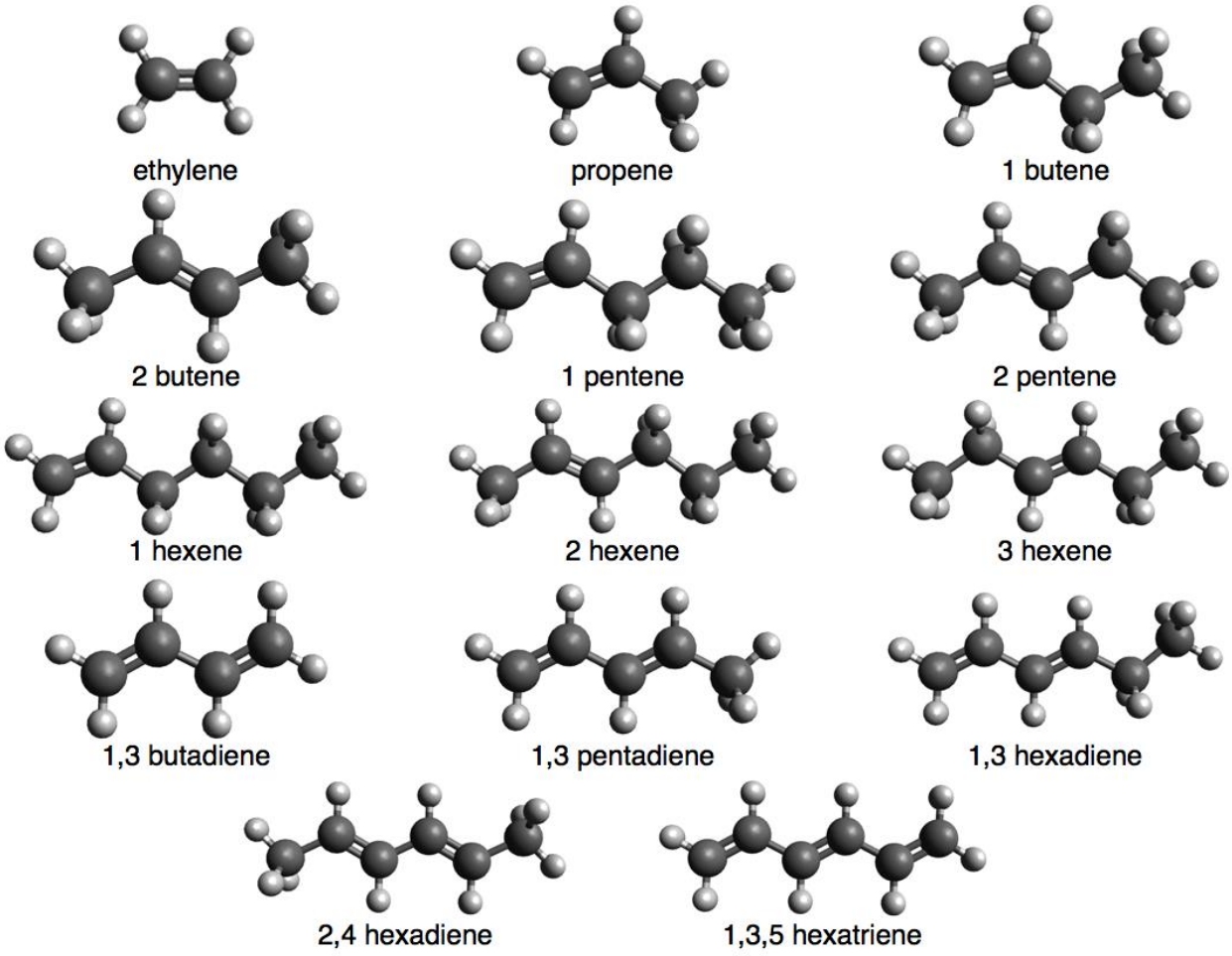

Figure 39. Suite of π-conjugated system used in this study.

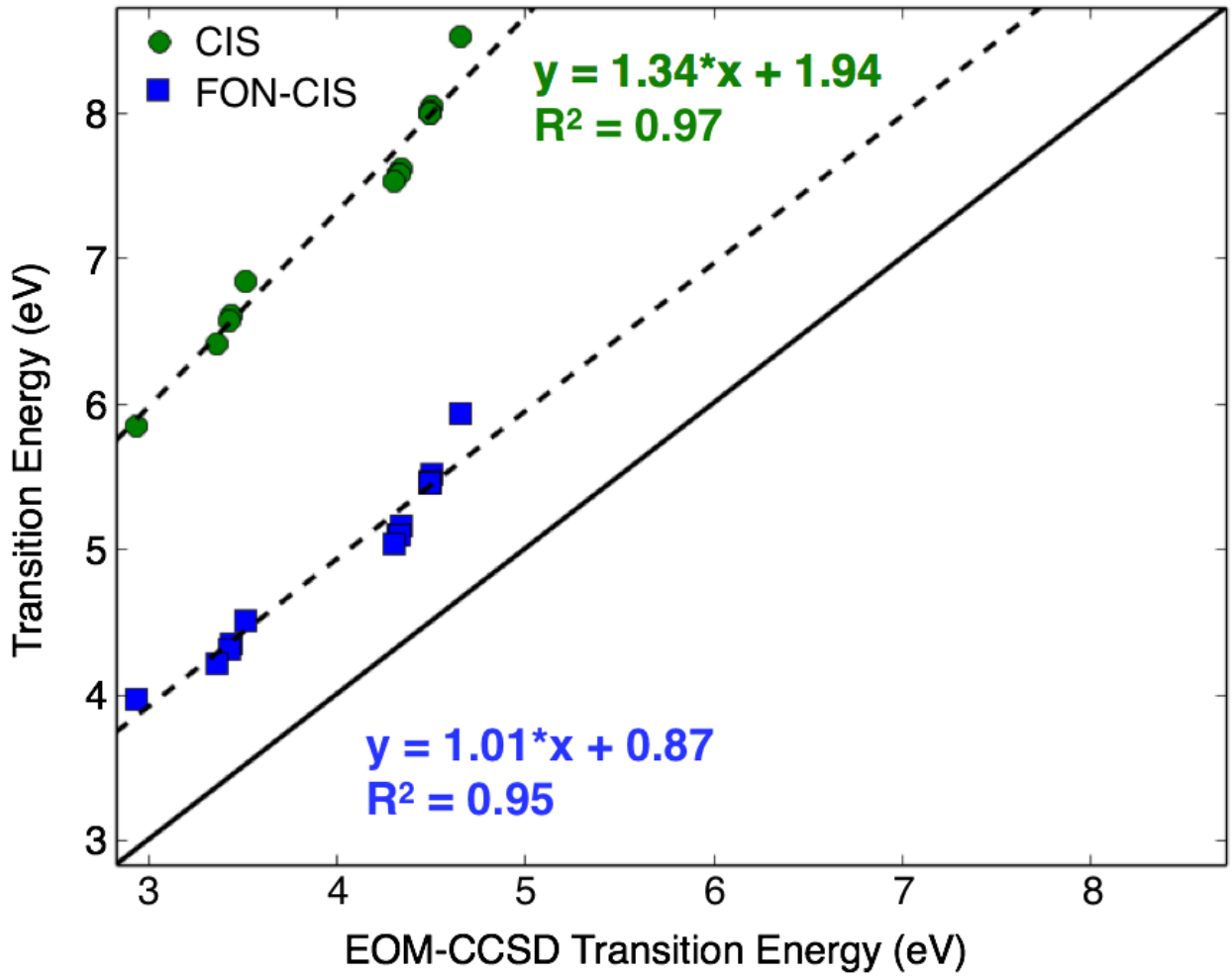

Figure 40. CIS (green) and FON-CIS (blue) as a function of EOM-CCSD excitation energy of HOMO-LUMO ($\pi \rightarrow \pi^*$) transition for each π=conjugated system. Dotted lines are linear fits of CIS and FON-CIS data set respectively. Solid line guides the eye to show ideal values for perfect agreement with EOM-CCSD results.

For each π-conjugated system we calculated the energy of the first EOM-CCSD transition as well as the CIS transition energy (Figure 40). The green data points show the relationship between the calculated HOMO-LUMO excitation energy of standard CIS and EOM-CCSD. CIS systematically overestimates the transition energy by about 3.0 eV relative to EOM-CCSD. Further, CIS introduces a non-parallelity error relative to the 1:1 EOM-CCSD line indicated by the 1.34 slope of the fitted line. In order to calculate the FON-CIS HOMO-LUMO transition energies (blue points in Figure 40), a FON-CIS calculation was performed at each temperature point along a grid ranging from 0K to 100,000K in steps of 2,000K and the resulting transition energy vs. temperature data was fit to a cubic polynomial. The FON-CIS values at the inflection point were calculated and plotted against EOM-CCSD results (Figure 40, blue squares). The FON-CIS approach reduced the overestimation of CIS relative to EOM-CCSD by an average of 72%, or 1.07 eV, for the HOMO-LUMO transition energy of each π-conjugated system considered. Moreover, the FON-CIS method virtually eliminated the non-parallelity error (slope of fit = 1.01) without impacting the quality of the fit (R^2=0.97 for CIS and R^2=0.95 for FON-CIS).

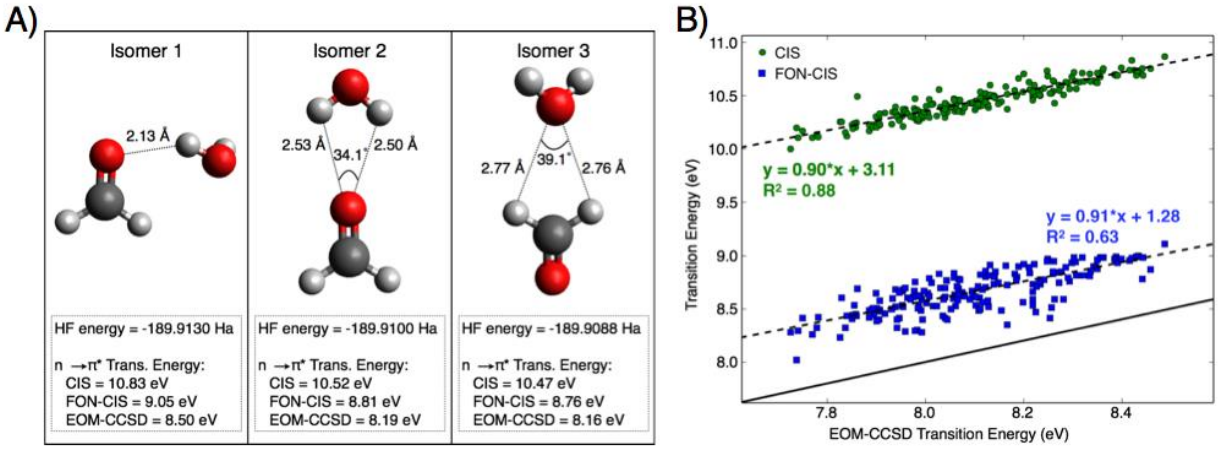

Figure 41. (A) Starting geometries and transition energies for each AIMD trajectory. (B) CIS (green) and FON-CIS (blue) as a function of EOM-CCSD excitation energy of n → π* transition. Each point represents a single geometry along an AIMD trajectory. Dotted lines are linear fits of CIS and FON-CIS data sets respectively. Solid line guides the eye to show ideal values for perfect agreement with EOM-CCSD results.

The transferability of the FON-CIS approach and choice of electronic temperature was tested by application to 195 formaldehyde-water dimer structures sampled from AIMD trajectories. In the gas phase, the formaldehyde-water dimer is predicted to have three primary local minimum structures.[229] Each of these local minima were built in Avogadro, optimized at the HF level of theory, and used as the starting structures for 3 AIMD simulations (structures in Figure 41A). The three different staring points allowed a significant portion of configurational space to be sampled. Altogether, 195 unique geometries of the formaldehyde-water dimer were considered and CIS, FON-CIS, and EOM-CCSD calculations were performed on each structure to collect statistics on the performance of the FON-CIS method. For each structure we target the

well-known n → π* transition of the Formaldehyde-water dimer, here showing up as the either the 4th, 5th, or 6th root of the CIS calculations.[230-231]

Because we sampled many geometries, the n → π* transition appears at a range of energies and often mixes with minor contributions from other amplitudes. Our analysis isolated the transition where the n → π* component was the majority contribution of the overall transition and followed that root as a function of electronic temperature. A total of 12 structures did not exhibit a root with dominant n → π* character and were therefore omitted from the data set in Figure 41B.

In Figure 41B the green circles show the relationship between CIS and EOM-CCSD transition energy, where CIS systematically overestimates the transition energy by more than 2.0 eV and a small non-parallelity error was observed in the CIS data (slope of fit = 0.90). Similar to the results from the π-conjugates systems, the FON-CIS transition energy data (Figure 41B, blue squares) shows a dramatic reduction in the transition energy error relative to EOM-CCSD: FON-CIS has a 1.83 eV (76%) smaller error in the transition energy compared to standard CIS calculations. While a small increase in the scatter was observed (probable errors: CIS = 0.041 eV and FON-CIS = 0.084 eV), the improvement was systematic and no additional non-parallelity error was introduced (slopes of line are 0.90 and 0.91 for CIS and FON-CIS respectively).

6.4 **Conclusion**

In conclusion, we have presented a method that uses fractional occupation numbers to improve excitation energies calculated with CIS at small computational overhead. Specifically, we treat CIS excitation energies as functionals of the HF single particle density, which we

parameterize using a single, fictitious electronic temperature parameter. As the electronic temperature is increased, this approach transfers occupation from occupied to previous empty orbitals, thus mixing excited electron configurations into the HF potential in which the orbitals are optimized. As a consequence, this approach allows us to target sets of specific excited states whose energies improve upon optimization of the participating orbitals. We found that the inflection point of the transition energy versus electronic temperature curve provides an accurate and transferable choice for *a priori* determination of the FON-CIS transition energy relative to EOM-CCSD benchmark results for the test systems studied. These improved excitation energies are likely associated with the finding that the inflection point marks a more balanced description of orbitals describing the participating ground and excited states. For example, FON-CIS resulted in a 1.07 eV (72%) improvement in $\pi \rightarrow \pi^*$ transition energy for π-conjugated hydrocarbons and a 1.83 eV (76%) improvement in $n \rightarrow \pi^*$ transition energy in the formaldehyde-water dimer. Overall, FON-CIS presents an attractive route toward inexpensive and improved excited state prediction with potential to provide accurate prediction of optoelectronic properties for previously intractable systems.

References

1.Gao, D.; Zhou, H.; Wang, J.; Miao, S.; Yang, F.; Wang, G.; Wang, J.; Bao, X., Size-Dependent Electrocatalytic Reduction of CO_2 Over Pd Nanoparticles. *J. Am. Chem. Soc.* **2015,** *137* (13), 4288-4291.

2.Gao, J.; Gu, H.; Xu, B., Multifunctional Magnetic Nanoparticles: Design, Synthesis, and Biomedical Applications. *Accounts Chem. Res.* **2009,** *42* (8), 1097-1107.

3.Pankhurst, Q. A.; Connolly, J.; Jones, S.; Dobson, J., Applications of Magnetic Nanoparticles in Biomedicine. *J. Phys. D: Appl. Phys.* **2003,** *36* (13), R167.

4.Andolina, C. M.; Dewar, A. C.; Smith, A. M.; Marbella, L. E.; Hartmann, M. J.; Millstone, J. E., Photoluminescent Gold–Copper Nanoparticle Alloys with Composition-Tunable Near-Infrared Emission. *J. Am. Chem. Soc.* **2013,** *135* (14), 5266-5269.

5.Marbella, L. E.; Andolina, C. M.; Smith, A. M.; Hartmann, M. J.; Dewar, A. C.; Johnston, K. A.; Daly, O. H.; Millstone, J. E., Gold- Cobalt Nanoparticle Alloys Exhibiting Tunable Compositions, Near- Infrared Emission, and High T2 Relaxivity. *Adv. Funct. Mater.* **2014,** *24* (41), 6532-6539.

6.James, T. E.; Hemmingson, S. L.; Campbell, C. T., Energy of Supported Metal Catalysts: from Single Atoms to Large Metal Nanoparticles. *ACS Catal.* **2015,** *5* (10), 5673-5678.

7.Gawande, M. B.; Goswami, A.; Felpin, F.-X.; Asefa, T.; Huang, X.; Silva, R.; Zou, X.; Zboril, R.; Varma, R. S., Cu and Cu-Based Nanoparticles: Synthesis and Applications in Catalysis. *Chem. Rev.* **2016,** *116* (6), 3722-3811.

8.Wilson, W. L.; Szajowski, P.; Brus, L., Quantum Confinement in Size-Selected, Surface-Oxidized Silicon Nanocrystals. *Science* **1993,** *262* (5137), 1242-1244.

9.Griffith, J.; Orgel, L., Ligand-Field Theory. *Q. Rev. Chem. Soc.* **1957,** *11* (4), 381-393.

10.Schäffer, C. E.; Jørgensen, C. K., The Nephelauxetic Series of Ligands Corresponding to Increasing Tendency of Partly Covalent Bonding. *J. Inorg. Nucl. Chem.* **1958,** *8*, 143-148.

11.Sappa, E.; Tiripicchio, A.; Braunstein, P., Selective Metal-Ligand Interactions in Heterometallic Transition Metal Clusters. *Coordin. Chem. Rev.* **1985,** *65*, 219-284.

12.Poliakoff, M.; Turner, J. J., Structure and Reactions of Matrix-Isolated Tetracarbonyliron(0). *J. Chem. Soc. Dalton* **1974,** (20), 2276-2285.

13.Mingos, D. M. P., Polyhedral Skeletal Electron Pair Approach. *Acc. Chem. Res.* **1984,** *17* (9), 311-319.

14.Wade, K., The Structural Significance of the Number of Skeletal Bonding Electron-Pairs in Carboranes, the Higher Boranes and Borane Anions, and Various Transition-Metal Carbonyl Cluster Compounds. *J. Chem. Soc. Chem. Comm.* **1971,** (15), 792-793.

15.Sappa, E.; Tiripicchio, A.; Carty, A. J.; Toogood, G. E., Butterfly Cluster Complexes of the Group VIII Transition Metals. *Prog. Inorg. Chem.* **1987**, 437-525.

16.Hoffmann, R., How Chemistry and Physics Meet in the Solid State. *Angew. Chem. Int. Ed.* **1987,** *26* (9), 846-878.

17.Gupta, R. P., Lattice Relaxation at a Metal Surface. *Phys. Rev. B* **1981,** *23* (12), 6265.
18.Sandy, A.; Mochrie, S.; Zehner, D.; Huang, K.; Gibbs, D., Structure and Phases of the Au(111) Surface: X-Ray-Scattering Measurements. *Phys. Rev. B* **1991,** *43* (6), 4667.
19.MacLean, D., Grain Boundaries in Metals. **1957**.
20.Priyadarshini, D.; Kondratyuk, P.; Picard, Y. N.; Morreale, B. D.; Gellman, A. J.; Miller, J. B., High-Throughput Characterization of Surface Segregation in Cu x Pd1–x Alloys. *J. Phys. Chem. C* **2011,** *115* (20), 10155-10163.
21.Tomanek, D.; Mukherjee, S.; Kumar, V.; Bennemann, K., Calculation of Chemisorption and Absorption Induced Surface Segregation. *Surf. Sci.* **1982,** *114* (1), 11-22.
22.Miller, J. B.; Priyadarshini, D.; Gellman, A. J., Segregation at the Surfaces of Cu_xPd_{1-x} Alloys in the Presence of Adsorbed S. *Surf. Sci.* **2012,** *606* (19-20), 1520-1526.
23.Hammer, B.; Nørskov, J., Electronic Factors Determining the Reactivity of Metal Surfaces. *Surf. Sci.* **1995,** *343* (3), 211-220.
24.Nørskov, J. K.; Bligaard, T.; Hvolbæk, B.; Abild-Pedersen, F.; Chorkendorff, I.; Christensen, C. H., The Nature of the Active Site in Heterogeneous Metal Catalysis. *Chem. Soc. Rev.* **2008,** *37* (10), 2163-2171.
25.Desireddy, A.; Conn, B. E.; Guo, J.; Yoon, B.; Barnett, R. N.; Monahan, B. M.; Kirschbaum, K.; Griffith, W. P.; Whetten, R. L.; Landman, U., Ultrastable Silver Nanoparticles. *Nature* **2013,** *501* (7467), 399.
26.Jadzinsky, P. D.; Calero, G.; Ackerson, C. J.; Bushnell, D. A.; Kornberg, R. D., Structure of a Thiol Monolayer-Protected Gold Nanoparticle at 1.1 Å Resolution. *Science* **2007,** *318* (5849), 430-433.
27.De Heer, W. A., The Physics of Simple Metal Clusters: Experimental Aspects and Simple Models. *Rev. Mod. Phys.* **1993,** *65* (3), 611.
28.Walter, M.; Akola, J.; Lopez-Acevedo, O.; Jadzinsky, P. D.; Calero, G.; Ackerson, C. J.; Whetten, R. L.; Grönbeck, H.; Häkkinen, H., A Unified View of Ligand-Protected Gold Clusters as Superatom Complexes. *Proc. Natl. Acad. Sci. USA* **2008,** *105* (27), 9157-9162.
29.Azubel, M.; Koivisto, J.; Malola, S.; Bushnell, D.; Hura, G. L.; Koh, A. L.; Tsunoyama, H.; Tsukuda, T.; Pettersson, M.; Häkkinen, H.; Kornberg, R. D., Electron Microscopy of Gold Nanoparticles at Atomic Resolution. *Science* **2014,** *345* (6199), 909-912.
30.Heaven, M. W.; Dass, A.; White, P. S.; Holt, K. M.; Murray, R. W., Crystal Structure of the Gold Nanoparticle [N(C8H17)4][Au25(SCH2CH2Ph)18]. *J. Am. Chem. Soc.* **2008,** *130* (12), 3754-3755.
31.Malola, S.; Lehtovaara, L.; Enkovaara, J.; Häkkinen, H., Birth of the Localized Surface Plasmon Resonance in Monolayer-Protected Gold Nanoclusters. *ACS Nano* **2013,** *7* (11), 10263-10270.
32.Higaki, T.; Zhou, M.; Lambright, K. J.; Kirschbaum, K.; Sfeir, M. Y.; Jin, R., Sharp Transition from Nonmetallic Au_{246} to Metallic Au_{279} with Nascent Surface Plasmon Resonance. *J. Am. Chem. Soc.* **2018,** *140* (17), 5691-5695.
33.Yi, C.; Tofanelli, M. A.; Ackerson, C. J.; Knappenberger Jr, K. L., Optical Properties and Electronic Energy Relaxation of Metallic $Au_{144}(SR)_{60}$ Nanoclusters. *J. Am. Chem. Soc.* **2013,** *135* (48), 18222-18228.
34.Negishi, Y.; Nakazaki, T.; Malola, S.; Takano, S.; Niihori, Y.; Kurashige, W.; Yamazoe, S.; Tsukuda, T.; Häkkinen, H., A Critical Size for Emergence of Nonbulk Electronic and Geometric Structures in Dodecanethiolate-Protected Au Clusters. *J. Am. Chem. Soc.* **2015,** *137* (3), 1206-1212.

35.Kaappa, S.; Malola, S.; Häkkinen, H., Point Group Symmetry Analysis of the Electronic Structure of Bare and Protected Metal Nanocrystals. *arXiv preprint arXiv:1808.01868* **2018**.
36.Malola, S.; Kaappa, S.; Hakkinen, H., From Molecular to Metallic Gold Nanoparticles: The Role of Nanocrystal Symmetry in the Crossover Region. *arXiv preprint arXiv:1809.04411* **2018**.
37.Stamenkovic, V. R.; Mun, B. S.; Arenz, M.; Mayrhofer, K. J.; Lucas, C. A.; Wang, G.; Ross, P. N.; Markovic, N. M., Trends in Electrocatalysis on Extended and Nanoscale Pt-Bimetallic Alloy Surfaces. *Nat. Mater.* **2007,** *6* (3), 241.
38.Valden, M.; Lai, X.; Goodman, D. W., Onset of Catalytic Activity of Gold Clusters on Titania with the Appearance of Nonmetallic Properties. *Science* **1998,** *281* (5383), 1647-1650.
39.Schebarchov, D.; Baletto, F.; Wales, D., Structure, Thermodynamics, and Rearrangement Mechanisms in Gold Clusters—Insights from the Energy Landscapes Framework. *Nanoscale* **2018,** *10* (4), 2004-2016.
40.Hume-Rothery, W.; Powell, H. M., On the Theory of Super-Lattice Structures in Alloys. *Z. Kristallogr.* **1935,** *91* (1-6), 23-47.
41.Palomares-Baez, J.-P.; Panizon, E.; Ferrando, R., Nanoscale Effects on Phase Separation. *Nano Lett.* **2017,** *17* (9), 5394-5401.
42.Baskaran, A.; Smereka, P., Mechanisms of Stranski-Krastanov Growth. *J. Appl. Phys.* **2012,** *111* (4), 044321.
43.Negishi, Y.; Iwai, T.; Ide, M., Continuous Modulation of Electronic Structure of Stable Thiolate-Protected Au_{25} Cluster by Ag Doping. *Chem. Commun.* **2010,** *46* (26), 4713-4715.
44.Kurashige, W.; Munakata, K.; Nobusada, K.; Negishi, Y., Synthesis of Stable Cu_nAu_{25-n} Nanoclusters (n=1–9) Using Selenolate Ligands. *Chem. Commun.* **2013,** *49* (48), 5447-5449.
45.Tofanelli, M. A.; Salorinne, K.; Ni, T. W.; Malola, S.; Newell, B.; Phillips, B.; Häkkinen, H.; Ackerson, C. J., Jahn–Teller Effects in $Au_{25}(SR)_{18}$. *Chem. Sci.* **2016,** *7* (3), 1882-1890.
46.Yao, C.; Lin, Y.-j.; Yuan, J.; Liao, L.; Zhu, M.; Weng, L.-h.; Yang, J.; Wu, Z., Mono-cadmium vs Mono-mercury Doping of Au_{25} Nanoclusters. *J. Am. Chem. Soc.* **2015,** *137* (49), 15350-15353.
47.Hartmann, M. J.; Häkkinen, H.; Millstone, J. E.; Lambrecht, D. S., Impacts of Copper Position on the Electronic Structure of $[Au_{25-x}Cu_x(SH)_{18}]^-$ Nanoclusters. *J. Phys. Chem. C* **2015,** *119* (15), 8290-8298.
48.Dharmaratne, A. C.; Dass, A., $Au_{144-x}Cu_x(SC_6H_{13})_{60}$ Nanomolecules: Effect of Cu Incorporation on Composition and Plasmon-Like Peak Emergence in Optical Spectra. *Chem. Commun.* **2014,** *50* (14), 1722-1724.
49.Malola, S.; Hartmann, M. J.; Hakkinen, H., Copper Induces a Core Plasmon in Intermetallic $Au_{(144,145)-x}Cu_x(SR)_{60}$ Nanoclusters. *J. Phys. Chem. Lett.* **2015,** *6* (3), 515-520.
50.Sun, S.; Murray, C. B.; Weller, D.; Folks, L.; Moser, A., Monodisperse FePt Nanoparticles and Ferromagnetic FePt Nanocrystal Superlattices. *Science* **2000,** *287* (5460), 1989-1992.
51.Marbella, L. E.; Chevrier, D. M.; Tancini, P. D.; Shobayo, O.; Smith, A. M.; Johnston, K. A.; Andolina, C. M.; Zhang, P.; Mpourmpakis, G.; Millstone, J. E., Description and Role of Bimetallic Prenucleation Species in the Formation of Small Nanoparticle Alloys. *J. Am. Chem. Soc.* **2015,** *137* (50), 15852-15858.
52.Taylor, M. G.; Mpourmpakis, G., Thermodynamic Stability of Ligand-Protected Metal Nanoclusters. *Nat. Commun.* **2017,** *8*, 15988.
53.Häkkinen, H., The Gold–Sulfur Interface at the Nanoscale. *Nat. Chem.* **2012,** *4* (6), 443.
54.Liu, P.; Qin, R.; Fu, G.; Zheng, N., Surface Coordination Chemistry of Metal Nanomaterials. *J. Am. Chem. Soc.* **2017,** *139* (6), 2122-2131.

55.Hartmann, M. J.; Millstone, J. E.; Häkkinen, H., Surface Chemistry Controls Magnetism in Cobalt Nanoclusters. *J. Phys. Chem. C* **2016,** *120* (37), 20822-20827.
56.Rodríguez-López, J.; Aguilera-Granja, F.; Michaelian, K.; Vega, A., Structure and Magnetism of Cobalt Clusters. *Phys. Rev. B* **2003,** *67* (17), 174413.
57.Xu, X.; Yin, S.; Moro, R.; de Heer, W. A., Magnetic Moments and Adiabatic Magnetization of Free Cobalt Clusters. *Phys. Rev. Lett.* **2005,** *95* (23), 237209.
58.Hartmann, M. J.; Millstone, J. E.; Häkkinen, H., Ligand Mediated Evolution of Size Dependent Magnetism in Cobalt Nanoclusters. *Phys. Chem. Chem. Phys.* **2018,** *20* (6), 4563-4570.
59.Crawford, S. E.; Andolina, C. M.; Smith, A. M.; Marbella, L. E.; Johnston, K. A.; Straney, P. J.; Hartmann, M. J.; Millstone, J. E., Ligand-Mediated "Turn On," High Quantum Yield Near-Infrared Emission in Small Gold Nanoparticles. *J. Am. Chem. Soc.* **2015,** *137* (45), 14423-14429.
60.El-Sayed, M. A., Some Interesting Properties of Metals Confined in Time and Nanometer Space of Different Shapes. *Acc. Chem. Res.* **2001,** *34* (4), 257-264.
61.Zhang, J. Z., Ultrafast Studies of Electron Dynamics in Semiconductor and Metal Colloidal Nanoparticles: Effects of Size and Surface. *Acc. Chem. Res.* **1997,** *30* (10), 423-429.
62.Voisin, C.; Christofilos, D.; Fatti, N. D.; Vallee, F.; Prevel, B.; Cottancin, E.; Lerme, J.; Pellarin, M.; Broyer, M., Size-Dependent Electron-Electron Interactions in Metal Nanoparticles. *Phys. Rev. Lett.* **2000,** *85* (10), 2200-2203.
63.Jain, P. K.; Huang, X.; El-Sayed, I. H.; El-Sayed, M. A., Noble Metals on the Nanoscale: Optical and Photothermal Properties and Some Applications in Imaging, Sensing, Biology, and Medicine. *Acc. Chem. Res.* **2008,** *41* (12), 1578-1586.
64.Link, S.; El-Sayed, M. A., Spectral Properties and Relaxation Dynamics of Surface Plasmon Electronic Oscillations in Gold and Silver Nanodots and Nanorods. *J. Phys. Chem. B* **1999,** *103* (40), 8410-8426.
65.Willets, K. A.; Van Duyne, R. P., Localized Surface Plasmon Resonance Spectroscopy and Sensing. *Annu. Rev. Phys. Chem.* **2007,** *58*, 267-297.
66.Kelly, K. L.; Coronado, E.; Zhao, L. L.; Schatz, G. C., The optical properties of metal nanoparticles: the influence of size, shape, and dielectric environment. *J. Phys. Chem. B* **2003,** *107* (3), 668-677.
67.Jain, P. K.; Lee, K. S.; El-Sayed, I. H.; El-Sayed, M. A., Calculated Absorption and Scattering Properties of Gold Nanoparticles of Different Size, Shape, and Composition: Applications in Biological Imaging and Biomedicine. *J. Phys. Chem. B* **2006,** *110* (14), 7238-7248.
68.Link, S.; El-Sayed, M. A., Size and Temperature Dependence of the Plasmon Absorption of Colloidal Gold Nanoparticles. *J. Phys. Chem. B* **1999,** *103* (21), 4212-4217.
69.Santillán, J. M. J.; Videla, F. A.; Scaffardi, L. B.; Schinca, D. C., Plasmon Spectroscopy for Subnanometric Copper Particles: Dielectric Function and Core–Shell Sizing. *Plasmonics* **2013,** *8* (2), 341-348.
70.Zheng, J.; Zhou, C.; Yu, M.; Liu, J., Different Sized Luminescent Gold Nanoparticles. *Nanoscale* **2012,** *4* (14), 4073-4083.
71.Christopher, P.; Xin, H.; Linic, S., Visible-Light-Enhanced Catalytic Oxidation Reactions on Plasmonic Silver Nanostructures. *Nat. Chem.* **2011,** *3* (6), 467.
72.Kleis, J.; Greeley, J.; Romero, N.; Morozov, V.; Falsig, H.; Larsen, A. H.; Lu, J.; Mortensen, J. J.; Dułak, M.; Thygesen, K. S., Finite Size Effects in Chemical Bonding: From Small Clusters to Solids. *Catal. Lett.* **2011,** *141* (8), 1067-1071.

73.Kim, D.; Resasco, J.; Yu, Y.; Asiri, A. M.; Yang, P., Synergistic Geometric and Electronic Effects for Electrochemical Reduction of Carbon Dioxide using Gold–Copper Bimetallic Nanoparticles. *Nat. Commun.* **2014,** *5*.
74.Sharma, P.; Brown, S.; Walter, G.; Santra, S.; Moudgil, B., Nanoparticles for Bioimaging. *Adv. Colloid Interfac.* **2006,** *123–126* (0), 471-485.
75.Marbella, L. E.; Andolina, C. M.; Smith, A. M.; Hartmann, M. J.; Dewar, A. C.; Johnston, K. A.; Daly, O. H.; Millstone, J. E., Gold-Cobalt Nanoparticle Alloys Exhibiting Tunable Compositions, Near-Infrared Emission, and High T2 Relaxivity. *Adv. Funct. Mater.* **2014,** *24* (41), 6532-6539.
76.Negishi, Y.; Takasugi, Y.; Sato, S.; Yao, H.; Kimura, K.; Tsukuda, T., Magic-Numbered Aun Clusters Protected by Glutathione Monolayers (n = 18, 21, 25, 28, 32, 39): Isolation and Spectroscopic Characterization. *J. Am. Chem. Soc.* **2004,** *126* (21), 6518-6519.
77.Walter, M.; Akola, J.; Lopez-Acevedo, O.; Jadzinsky, P. D.; Calero, G.; Ackerson, C. J.; Whetten, R. L.; Grönbeck, H.; Häkkinen, H., A Unified View of Ligand-Protected Gold Clusters as Superatom Complexes. *P. Natl. Acad. Sci. USA* **2008,** *105* (27), 9157-9162.
78.Akola, J.; Walter, M.; Whetten, R. L.; Häkkinen, H.; Grönbeck, H., On the Structure of Thiolate-Protected Au25. *J. Am. Chem. Soc.* **2008,** *130* (12), 3756-3757.
79.Brack, M., The Physics of Simple Metal Clusters: Self-Consistent Jellium Model and Semiclassical Approaches. *Rev. Mod. Phys.* **1993,** *65* (3), 677.
80.Yang, H.; Wang, Y.; Huang, H.; Gell, L.; Lehtovaara, L.; Malola, S.; Häkkinen, H.; Zheng, N., All-Thiol-Stabilized Ag44 and Au12Ag32 Nanoparticles with Single-Crystal Structures. *Nat. Commun.* **2013,** *4*.
81.Knoppe, S.; Lehtovaara, L.; Häkkinen, H., Electronic Structure and Optical Properties of the Intrinsically Chiral 16-Electron Superatom Complex [Au20 (PP3) 4] 4+. *J. Phys. Chem. A* **2014**.
82.Nishigaki, J.-i.; Tsunoyama, R.; Tsunoyama, H.; Ichikuni, N.; Yamazoe, S.; Negishi, Y.; Ito, M.; Matsuo, T.; Tamao, K.; Tsukuda, T., A New Binding Motif of Sterically Demanding Thiolates on a Gold Cluster. *J. Am. Chem. Soc.* **2012,** *134* (35), 14295-14297.
83.Yang, H.; Wang, Y.; Edwards, A. J.; Yan, J.; Zheng, N., High-Yield Synthesis and Crystal Structure of a Green Au30 Cluster Co-Capped by Thiolate and Sulfide. *Chem. Commun.* **2014,** *50* (92), 14325-14327.
84.Morinaga, M.; Yukawa, N.; Adachi, H., Alloying Effect on the Electronic Structure of BCC Fe. *J. Phys. F Met. Phys.* **1985,** *15* (5), 1071.
85.Rodriguez, J. A.; Jirsak, T.; Chaturvedi, S.; Hrbek, J., Surface Chemistry of SO2 on Sn and Sn/Pt(111) Alloys: Effects of Metal−Metal Bonding on Reactivity toward Sulfur. *J. Am. Chem. Soc.* **1998,** *120* (43), 11149-11157.
86.Lopez, N.; Nørskov, J. K., Synergetic Effects in CO Adsorption on Cu–Pd(111) Alloys. *Surf. Sci.* **2001,** *477* (1), 59-75.
87.Peng, Z.; Yang, H., Designer Platinum Nanoparticles: Control of Shape, Composition in Alloy, Nanostructure and Electrocatalytic Property. *Nano Today* **2009,** *4* (2), 143-164.
88.Panizon, E.; Bochicchio, D.; Rossi, G.; Ferrando, R., Tuning the Structure of Nanoparticles by Small Concentrations of Impurities. *Chemistry of Materials* **2014,** *26* (11), 3354-3356.
89.Guidez, E. B.; Mäkinen, V.; Häkkinen, H.; Aikens, C. M., Effects of Silver Doping on the Geometric and Electronic Structure and Optical Absorption Spectra of the Au25–nAgn(SH)18– (n = 1, 2, 4, 6, 8, 10, 12) Bimetallic Nanoclusters. *J. Phys. Chem. C* **2012,** *116* (38), 20617-20624.

90.Tang, W.; Sanville, E.; Henkelman, G., A Grid-Based Bader Analysis Algorithm Without Lattice Bias. *J. Phys.-Condens. Mat.* **2009,** *21* (8), 084204.
91.Enkovaara, J.; Rostgaard, C.; Mortensen, J. J.; Chen, J.; Dułak, M.; Ferrighi, L.; Gavnholt, J.; Glinsvad, C.; Haikola, V.; Hansen, H. A.; Kristoffersen, H. H.; Kuisma, M.; Larsen, A. H.; Lehtovaara, L.; Ljungberg, M.; Lopez-Acevedo, O.; Moses, P. G.; Ojanen, J.; Olsen, T.; Petzold, V.; Romero, N. A.; Stausholm-Møller, J.; Strange, M.; Tritsaris, G. A.; Vanin, M.; Walter, M.; Hammer, B.; Häkkinen, H.; Madsen, G. K. H.; Nieminen, R. M.; Nørskov, J. K.; Puska, M.; Rantala, T. T.; Schiøtz, J.; Thygesen, K. S.; Jacobsen, K. W., Electronic Structure Calculations with GPAW: a Real-Space Implementation of the Projector Augmented-Wave Method. *J. Phys.-Condens. Mat.* **2010,** *22* (25), 253202.
92.Mortensen, J. J.; Hansen, L. B.; Jacobsen, K. W., Real-Space Grid Implementation of the Projector Augmented Wave Method. *Phys. Rev. B* **2005,** *71* (3).
93.Perdew, J. P.; Wang, Y., Accurate and Simple Analytic Representation of the Electron-Gas Correlation. *Phys. Rev. B* **1992,** *45* (23), 13244-13249.
94.Casida, M. E., Time-Dependent Density-Functional Response Theory for Molecules. *Recent advances in density functional methods* **1995,** *1*, 155.
95.Perdew, J. P.; Burke, K.; Ernzerhof, M., Generalized Gradient Approximation Made Simple. *Phys. Rev. Lett.* **1996,** *77* (18), 3865-3868.
96.Muniz-Miranda, F.; Menziani, M. C.; Pedone, A., Assessment of Exchange-Correlation Functionals in Reproducing the Structure and Optical Gap of Organic-Protected Gold Nanoclusters. *J. Phys. Chem. C* **2014,** *118* (14), 7532-7544.
97.Jiang, D.-e.; Tiago, M. L.; Luo, W.; Dai, S., The "Staple" Motif: A Key to Stability of Thiolate-Protected Gold Nanoclusters. *J. Am. Chem. Soc.* **2008,** *130* (9), 2777-2779.
98.Negishi, Y.; Chaki, N. K.; Shichibu, Y.; Whetten, R. L.; Tsukuda, T., Origin of Magic Stability of Thiolated Gold Clusters: A Case Study on Au25(SC6H13)18. *J. Am. Chem. Soc.* **2007,** *129* (37), 11322-11323.
99.Aikens, C. M., Effects of Core Distances, Solvent, Ligand, and Level of Theory on the TDDFT Optical Absorption Spectrum of the Thiolate-Protected Au25 Nanoparticle. *J. Phys. Chem. A* **2009,** *113* (40), 10811-10817.
100.Yamazoe, S.; Kurashige, W.; Nobusada, K.; Negishi, Y.; Tsukuda, T., Preferential Location of Coinage Metal Dopants (M = Ag or Cu) in [Au25–xMx(SC2H4Ph)18]− (x ∼ 1) As Determined by Extended X-ray Absorption Fine Structure and Density Functional Theory Calculations. *J. Phys. Chem. C* **2014,** *118* (43), 25284-25290.
101.Bauschlicher, C. W.; Langhoff, S. R.; Partridge, H., Theoretical Study of the Structures and Electron Affinities of the Dimers and Trimers of the Group IB Metals (Cu, Ag, and Au). *J. Chem. Phys.* **1989,** *91* (4), 2412-2419.
102.Zhu, M.; Aikens, C. M.; Hollander, F. J.; Schatz, G. C.; Jin, R., Correlating the Crystal Structure of A Thiol-Protected Au25 Cluster and Optical Properties. *J. Am. Chem. Soc.* **2008,** *130* (18), 5883-5885.
103.Jiang, D.-e.; Dai, S., From Superatomic Au25(SR)18− to Superatomic M@Au24(SR)18q Core−Shell Clusters. *Inorganic Chemistry* **2009,** *48* (7), 2720-2722.
104.Negishi, Y.; Munakata, K.; Ohgake, W.; Nobusada, K., Effect of Copper Doping on Electronic Structure, Geometric Structure, and Stability of Thiolate-Protected Au25 Nanoclusters. *The Journal of Physical Chemistry Letters* **2012,** *3* (16), 2209-2214.
105.Spear, W. E.; Le Comber, P. G., Substitutional Doping of Amorphous Silicon. *Solid State Commun.* **1975,** *17* (9), 1193-1196.

106.Schwerdtfeger, P., Relativistic Effects in Properties of Gold. *Heteroatom Chem.* **2002,** *13* (6), 578-584.
107.Hoffmann, R., The Theoretical Design of Novel Stabilized Systems. *Pure Appl. Chem.* **1971,** *28* (2-3), 181-194.
108.Kim, B. G.; Ma, X.; Chen, C.; Ie, Y.; Coir, E. W.; Hashemi, H.; Aso, Y.; Green, P. F.; Kieffer, J.; Kim, J., Energy Level Modulation of HOMO, LUMO, and Band- Gap in Conjugated Polymers for Organic Photovoltaic Applications. *Adv. Funct. Mater.* **2013,** *23* (4), 439-445.
109.Rio, Y.; Rodriguez-Morgade, M. S.; Torres, T., Modulating the Electronic Properties of Porphyrinoids: A Voyage from the Violet to the Infrared Regions of the Electromagnetic Spectrum. *Org. Biomol. Chem.* **2008,** *6* (11), 1877-1894.
110.Rounaghi, G.; Popov, A. I., Complexing Ability of some Mixed Sulfur-Oxygen Crown Ethers in Nonaqueous Solvents. *J. Inorg. Nucl. Chem.* **1981,** *43* (5), 911-915.
111.Ackerson, C. J.; Powell, R. D.; Hainfeld, J. F., Site-Specific Biomolecule Labeling with Gold Clusters. In *Methods Enzymol.*, Elsevier: 2010; Vol. 481, pp 195-230.
112.Ackerson, C. J.; Sykes, M. T.; Kornberg, R. D., Defined DNA/Banoparticle Conjugates. *Proc. Natl Acad. Sci. USA* **2005,** *102* (38), 13383-13385.
113.Sexton, J. Z.; Ackerson, C. J., Determination of Rigidity of Protein Bound Au144 Clusters by Electron Cryomicroscopy. *J. Phys. Chem. C* **2010,** *114* (38), 16037-16042.
114.Pluchery, O., Optical Properties of Gold Nanoparticles. *Gold Nanoparticles for Physics, Chemistry and Biology* **2012**, 43-73.
115.Marjomäki, V.; Lahtinen, T.; Martikainen, M.; Koivisto, J.; Malola, S.; Salorinne, K.; Pettersson, M.; Häkkinen, H., Site-Specific Targeting of Enterovirus Capsid by Functionalized Monodisperse Gold Nanoclusters. *Proc. Natl Acad. Sci. USA* **2014,** *111* (4), 1277-1281.
116.Aikens, C. M., Electronic Structure of Ligand-Passivated Gold and Silver Nanoclusters. *J. Phys. Chem. Lett.* **2010,** *2* (2), 99-104.
117.Häkkinen, H., Atomic and Electronic Structure of Gold Clusters: Understanding Flakes, Cages and Superatoms from Simple Concepts. *Chem. Soc. Rev.* **2008,** *37* (9), 1847-1859.
118.Jin, R., Quantum Sized, Thiolate-Protected Gold Nanoclusters. *Nanoscale* **2010,** *2* (3), 343-362.
119.Negishi, Y., Toward the Creation of Functionalized Metal Nanoclusters and Highly Active Photocatalytic Materials Using Thiolate-Protected Magic Gold Clusters. *Bull. Chem. Soc. Jpn* **2013,** *87* (3), 375-389.
120.Sardar, R.; Funston, A. M.; Mulvaney, P.; Murray, R. W., Gold Nanoparticles: Past, Present, and Future. *Langmuir* **2009,** *25* (24), 13840-13851.
121.Tsukuda, T., Toward an Atomic-Level Understanding of Size-Specific Properties of Protected and Stabilized Gold Clusters. *Bull. Chem. Soc. Jpn* **2012,** *85* (2), 151-168.
122.Barcaro, G.; Sementa, L.; Fortunelli, A.; Stener, M., Comment on "$(Au–Ag)_{144}(SR)_{60}$ Alloy Nanomolecules" by C. Kumara and A. Dass, Nanoscale, 2011, 3, 3064. *Nanoscale* **2015,** *7* (17), 8166-8167.
123.Fields-Zinna, C. A.; Crowe, M. C.; Dass, A.; Weaver, J. E.; Murray, R. W., Mass Spectrometry of Small Bimetal Monolayer-Protected Clusters. *Langmuir* **2009,** *25* (13), 7704-7710.
124.Guidez, E. B.; Mäkinen, V.; Häkkinen, H.; Aikens, C. M., Effects of Silver Doping on the Geometric and Electronic Structure and Optical Absorption Spectra of the $Au_{25-n}Ag_n(SH)_{18}^-$ (n= 1, 2, 4, 6, 8, 10, 12) Bimetallic Nanoclusters. *J. Phys. Chem. C* **2012,** *116* (38), 20617-20624.

125.Koivisto, J.; Malola, S.; Kumara, C.; Dass, A.; Häkkinen, H.; Pettersson, M., Experimental and Theoretical Determination of the Optical Gap of the $Au_{144}(SC_2H_4Ph)_{60}$ Cluster and the $(Au/Ag)_{144}(SC_2H_4Ph)_{60}$ Nanoalloys. *J. Phys. Chem. Lett.* **2012,** *3* (20), 3076-3080.
126.Kothalawala, N.; Kumara, C.; Ferrando, R.; Dass, A., $Au_{144-x}Pd_x(SR)_{60}$ Nanomolecules. *Chem. Commun.* **2013,** *49* (92), 10850-10852.
127.Kumara, C.; Dass, A., $(AuAg)_{144}(SR)_{60}$ Alloy Nanomolecules. *Nanoscale* **2011,** *3* (8), 3064-3067.
128.Malola, S.; Häkkinen, H., Electronic Structure and Bonding of Icosahedral Core–Shell Gold–Silver Nanoalloy Clusters $Au_{144-x}Ag_x(SR)_{60}$. *J. Phys. Chem. Lett.* **2011,** *2* (18), 2316-2321.
129.Malola, S.; Lehtovaara, L.; Häkkinen, H., TDDFT Analysis of Optical Properties of Thiol Monolayer-Protected Gold and Intermetallic Silver–Gold $Au_{144}(SR)_{60}$ and $Au_{84}Ag_{60}(SR)_{60}$ Clusters. *J. Phys. Chem. C* **2014,** *118* (34), 20002-20008.
130.Negishi, Y.; Kurashige, W.; Niihori, Y.; Iwasa, T.; Nobusada, K., Isolation, Structure, and Stability of a Dodecanethiolate-Protected Pd_1Au_{24} Cluster. *Phys. Chem. Chem. Phys.* **2010,** *12* (23), 6219-6225.
131.Qian, H.; Jiang, D.-e.; Li, G.; Gayathri, C.; Das, A.; Gil, R. R.; Jin, R., Monoplatinum Doping oGold Nanoclusters and Catalytic Application. *J. Am. Chem. Soc.* **2012,** *134* (39), 16159-16162.
132.Xie, S.; Tsunoyama, H.; Kurashige, W.; Negishi, Y.; Tsukuda, T., Enhancement in Aerobic Alcohol Oxidation Catalysis of Au_{25} Clusters by Single Pd Atom Doping. *ACS Catal.* **2012,** *2* (7), 1519-1523.
133.Yamazoe, S.; Kurashige, W.; Nobusada, K.; Negishi, Y.; Tsukuda, T., Preferential Location of Coinage Metal Dopants (M= Ag or Cu) in $[Au_{25-x}M_x(SC_2H_4Ph)_{18}]^-$ (x~1) As Determined by Extended X-ray Absorption Fine Structure and Density Functional Theory Calculations. *J. Phys. Chem. C* **2014,** *118* (43), 25284-25290.
134.Yang, H.; Wang, Y.; Lei, J.; Shi, L.; Wu, X.; Mäkinen, V.; Lin, S.; Tang, Z.; He, J.; Häkkinen, H., Ligand-Stabilized $Au_{13}Cu_x$ (x= 2, 4, 8) Bimetallic Nanoclusters: Ligand Engineering to Control the Exposure of Metal Sites. *J. Am. Chem. Soc.* **2013,** *135* (26), 9568-9571.
135.Yang, H.; Wang, Y.; Yan, J.; Chen, X.; Zhang, X.; Häkkinen, H.; Zheng, N., Structural Evolution of Atomically Precise Thiolated Bimetallic $[Au_{12+n}Cu_{32}(SR)_{30+n}]^{4-}$ (n= 0, 2, 4, 6) Nanoclusters. *J. Am. Chem. Soc.* **2014,** *136* (20), 7197-7200.
136.Ferrando, R.; Jellinek, J.; Johnston, R. L., Nanoalloys: From Theory to Applications of Alloy Clusters and Nanoparticles. *Chem. Rev.* **2008,** *108* (3), 845-910.
137.Lopez-Acevedo, O.; Akola, J.; Whetten, R. L.; Grönbeck, H.; Häkkinen, H., Structure and Bonding in the Ubiquitous Icosahedral Metallic Gold Cluster $Au_{144}(SR)_{60}$. *J. Phys. Chem. C* **2009,** *113* (13), 5035-5038.
138.Chaki, N. K.; Negishi, Y.; Tsunoyama, H.; Shichibu, Y.; Tsukuda, T., Ubiquitous 8 and 29 kDa Gold: Alkanethiolate Cluster Compounds: Mass-Spectrometric Determination of Molecular Formulas and Structural Implications. *J. Am. Chem. Soc.* **2008,** *130* (27), 8608-8610.
139.Fields-Zinna, C. A.; Sardar, R.; Beasley, C. A.; Murray, R. W., Electrospray Ionization Mass Spectrometry of Intrinsically Cationized Nanoparticles,$[Au_{144/146}(SC_{11}H_{22}N(CH_2CH_3)_3^+)_x(S(CH_2)_5CH_3)_y]^{x+}$. *J. Am. Chem. Soc.* **2009,** *131* (44), 16266-16271.
140.Hicks, J. F.; Miles, D. T.; Murray, R. W., Quantized Double-Layer Charging of Highly Monodisperse Metal Nanoparticles. *J. Am. Chem. Soc.* **2002,** *124* (44), 13322-13328.

141.Koivisto, J.; Salorinne, K.; Mustalahti, S.; Lahtinen, T.; Malola, S.; Häkkinen, H.; Pettersson, M., Vibrational Perturbations and Ligand–Layer Coupling in a Single Crystal of $Au_{144}(SC_2H_4Ph)_{60}$ Nanocluster. *J. Phys. Chem. Lett.* **2014,** *5* (2), 387-392.
142.Qian, H.; Jin, R., Controlling Nanoparticles with Atomic Precision: The Case of $Au_{144}(SCH_2CH_2Ph)_{60}$. *Nano Lett.* **2009,** *9* (12), 4083-4087.
143.Quinn, B. M.; Liljeroth, P.; Ruiz, V.; Laaksonen, T.; Kontturi, K., Electrochemical Resolution of 15 Oxidation States for Monolayer Protected Gold Nanoparticles. *J. Am. Chem. Soc.* **2003,** *125* (22), 6644-6645.
144.Salorinne, K.; Lahtinen, T.; Koivisto, J.; Kalenius, E.; Nissinen, M.; Pettersson, M.; Häkkinen, H., Nondestructive Size Determination of Thiol-Stabilized Gold Nanoclusters in Solution by Diffusion Ordered NMR Spectroscopy. *Anal. Chem.* **2013,** *85* (7), 3489-3492.
145.Schaaff, T. G.; Shafigullin, M. N.; Khoury, J. T.; Vezmar, I.; Whetten, R. L., Properties of a Ubiquitous 29 kDa Au:SR Cluster Compound. *J. Phys. Chem. B* **2001,** *105* (37), 8785-8796.
146.Häkkinen, H.; Walter, M.; Grönbeck, H., Divide and Protect: Capping Gold Nanoclusters with Molecular Gold−Thiolate Rings. *J. Phys. Chem. B* **2006,** *110* (20), 9927-9931.
147.Weissker, H.-C.; Escobar, H. B.; Thanthirige, V.; Kwak, K.; Lee, D.; Ramakrishna, G.; Whetten, R.; López-Lozano, X., Information on Quantum States Pervades the Visible Spectrum of the Ubiquitous $Au_{144}(SR)_{60}$ Gold Nanocluster. *Nature Commun.* **2014,** *5*, 3785.
148.Enkovaara, J. e.; Rostgaard, C.; Mortensen, J. J.; Chen, J.; Dułak, M.; Ferrighi, L.; Gavnholt, J.; Glinsvad, C.; Haikola, V.; Hansen, H., Electronic Structure Calculations with GPAW: A Real-Space Implementation of the Projector Augmented-Wave Method. *J. Phys.: Condens. Matter* **2010,** *22* (25), 253202.
149.Mortensen, J. J.; Hansen, L. B.; Jacobsen, K. W., Real-Space Grid Implementation of the Projector Augmented Wave Method. *Phys. Rev. B* **2005,** *71* (3), 035109.
150.Henkelman, G.; Arnaldsson, A.; Jónsson, H., A Fast and Robust Algorithm for Bader Decomposition of Charge Density. *Comput. Mater. Sci.* **2006,** *36* (3), 354-360.
151.Walter, M.; Häkkinen, H.; Lehtovaara, L.; Puska, M.; Enkovaara, J.; Rostgaard, C.; Mortensen, J. J., Time-Dependent Density-Functional Theory in the Projector Augmented-Wave Method. *J. Chem. Phys.* **2008,** *128* (24), 244101.
152.Perdew, J. P.; Burke, K.; Ernzerhof, M., Generalized Gradient Approximation Made Simple. *Phys. Rev. Lett.* **1996,** *77* (18), 3865.
153.Pyykko, P., Relativistic Effects in Structural Chemistry. *Chem. Rev.* **1988,** *88* (3), 563-594.
154.Christensen, N. E.; Seraphin, B., Relativistic Band Calculation and the Optical Properties of Gold. *Phys. Rev. B* **1971,** *4* (10), 3321.
155.Courths, R.; Cord, B.; Wern, H.; Hüfner, S., Angle-Resolved Photoemission and Band Structure of Copper. *Phys. Scr.* **1983,** *1983* (T4), 144.
156.Lewis, P.; Lee, P., Band Structure and Electronic Properties of Silver. *Phys. Rev.* **1968,** *175* (3), 795.
157.Negishi, Y.; Munakata, K.; Ohgake, W.; Nobusada, K., Effect of Copper Doping on Electronic Structure, Geometric Structure, and Stability of Thiolate-protected Au_{25} Nanoclusters. *J. Phys. Chem. Lett.* **2012,** *3* (16), 2209-2214.
158.Chappert, C.; Fert, A.; Van Dau, F. N., The emergence of spin electronics in data storage. *Nature materials* **2007,** *6* (11), 813-823.
159.Kelly, K. L.; Coronado, E.; Zhao, L. L.; Schatz, G. C., The Optical Properties of Metal Nanoparticles: the Influence of Size, Shape, and Dielectric Environment. *J. Phys. Chem. B* **2003,** *107*, 668-677.

160.Verma, A.; Stellacci, F., Effect of Surface Properties on Nanoparticle–Cell Interactions. *Small* **2010,** *6*, 12-21.
161.Lee, K.-S.; El-Sayed, M. A., Gold and Silver Nanoparticles in Sensing and Imaging: Sensitivity of Plasmon Response to Size, Shape, and Metal Composition. *J. Phys. Chem. B* **2006,** *110*, 19220-19225.
162.Malola, S.; Lehtovaara, L.; Enkovaara, J.; Häkkinen, H., Birth of the Localized Surface Plasmon Resonance in Monolayer-Protected Gold Nanoclusters. *ACS Nano* **2013,** *7*, 10263-10270.
163.Santillán, J.; Videla, F.; Scaffardi, L.; Schinca, D., Plasmon Spectroscopy for Subnanometric Copper Particles: Dielectric Function and Core–Shell Sizing. *Plasmonics* **2013,** *8*, 341-348.
164.Carroll, G. M.; Schimpf, A. M.; Tsui, E. Y.; Gamelin, D. R., Redox Potentials of Colloidal n-Type ZnO Nanocrystals: Effects of Confinement, Electron Density, and Fermi-Level Pinning by Aldehyde Hydrogenation. *J. Am. Chem. Soc.* **2015,** *137*, 11163-11169.
165.Billas, I. M.; Chatelain, A.; de Heer, W. A., Magnetism from the Atom to the Bulk in Iron, Cobalt, and nickel Clusters. *Science* **1994,** *265* (5179), 1682-1684.
166.Xu, X.; Yin, S.; Moro, R.; de Heer, W. A., Magnetic Moments and Adiabatic Magnetization of Free Cobalt Clusters. *Phys. Rev. Lett.* **2005,** *95*, 237209.
167.Rodríguez-López, J.; Aguilera-Granja, F.; Michaelian, K.; Vega, A., Structure and Magnetism of Cobalt Clusters. *Phys. Rev. B* **2003,** *67*, 174413.
168.Gerion, D.; Hirt, A.; Billas, I.; Châtelain, A.; de Heer, W., Experimental Specific Heat of Iron, Cobalt, and Nickel Clusters Studied in a Molecular Beam. *Phys. Rev. B* **2000,** *62*, 7491-7501.
169.Jadzinsky, P. D.; Calero, G.; Ackerson, C. J.; Bushnell, D. A.; Kornberg, R. D., Structure of a Thiol Monolayer-Protected Gold Nanoparticle at 1.1 Å Resolution. *Science* **2007,** *318*, 430-433.
170.Bhat, R. R.; Genzer, J., Combinatorial Study of Nanoparticle Dispersion in Surface-Grafted Macromolecular Gradients. *Appl. Surf. Sci.* **2006,** *252*, 2549-2554.
171.van Leeuwen, D. A.; Van Ruitenbeek, J.; De Jongh, L.; Ceriotti, A.; Pacchioni, G.; Häberlen, O.; Rösch, N., Quenching of Magnetic Moments by Ligand-Metal Interactions in Nanosized Magnetic Metal Clusters. *Phys. Rev. Lett.* **1994,** *73*, 1432.
172.Respaud, M.; Broto, J.; Rakoto, H.; Fert, A.; Thomas, L.; Barbara, B.; Verelst, M.; Snoeck, E.; Lecante, P.; Mosset, A., Surface Effects on the Magnetic Properties of Ultrafine Cobalt Particles. *Phys. Rev. B* **1998,** *57*, 2925-2935.
173.Knickelbein, M. B., Nickel clusters: The influence of adsorbates on magnetic moments. *The Journal of chemical physics* **2002,** *116* (22), 9703-9711.
174.Kennedy, J.; Leveneur, J.; Williams, G.; Mitchell, D.; Markwitz, A., Fabrication of Surface Magnetic Nanoclusters Using Low Energy Ion Implantation and Electron Beam Annealing. *Nanotechnology* **2011,** *22* (11), 115602.
175.Leveneur, J.; Waterhouse, G. I.; Kennedy, J.; Metson, J. B.; Mitchell, D. R., Nucleation and growth of Fe nanoparticles in SiO2: a TEM, XPS, and Fe L-edge XANES investigation. *The Journal of Physical Chemistry C* **2011,** *115* (43), 20978-20985.
176.Cotton, F.; Meyers, M., Magnetic and Spectral Properties of the Spin-Free 3d6 Systems Iron (II) and Cobalt (III) in Cobalt (III) Hexafluoride Ion: Probable Observation of Dynamic Jahn-Teller Effects. *J. Am. Chem. Soc.* **1960,** *82*, 5023-5026.
177.Cotton, F. A.; Goodgame, D.; Goodgame, M., The Electronic Structures of Tetrahedral Cobalt (II) Complexes. *J. Am. Chem. Soc.* **1961,** *83*, 4690-4699.

178.Aakesson, R.; Pettersson, L. G.; Sandstroem, M.; Wahlgren, U., Ligand Field Effects in the Hydrated Divalent and Trivalent Metal Ions of the First and Second Transition Periods. *J. Am. Chem. Soc.* **1994,** *116*, 8691-8704.
179.Rives, S.; Catherinot, A.; Dumas-Bouchiat, F.; Champeaux, C.; Videcoq, A.; Ferrando, R., Growth of Co Isolated Clusters in the Gas Phase: Experiment and Molecular Dynamics Simulations. *Phys. Rev. B* **2008,** *77* (8), 085407.
180.Tang, W.; Sanville, E.; Henkelman, G., A Grid-Based Bader Analysis Algorithm Without Lattice Bias. *J. Phys-Condens. Mat.* **2009,** *21*, 084204.
181.Enkovaara, J.; Rostgaard, C.; Mortensen, J. J.; Chen, J.; Dułak, M.; Ferrighi, L.; Gavnholt, J.; Glinsvad, C.; Haikola, V.; Hansen, H., Electronic Structure Calculations with GPAW: a Real-Space Implementation of the Projector Augmented-Wave Method. *J. Phys-Condens. Mat.* **2010,** *22*, 253202.
182.Perdew, J. P.; Burke, K.; Ernzerhof, M., Generalized Gradient Approximation Made Simple. *Phys. Rev. Lett.* **1996,** *77*, 3865-3868.
183.Jo, C.; Lee, J. I., Spin Polarization and Charge Transfer of Co Nanoclusters Coated with CO Molecules. *J. Magn. Magn. Mater.* **2009,** *321*, 47-51.
184.Giannozzi, P.; Baroni, S.; Bonini, N.; Calandra, M.; Car, R.; Cavazzoni, C.; Ceresoli, D.; Chiarotti, G. L.; Cococcioni, M.; Dabo, I., QUANTUM ESPRESSO: a modular and open-source software project for quantum simulations of materials. *Journal of Physics: Condensed Matter* **2009,** *21* (39), 395502.
185.Vanderbilt, D., Soft self-consistent pseudopotentials in a generalized eigenvalue formalism. *Physical Review B* **1990,** *41* (11), 7892.
186.Ganguly, S.; Kabir, M.; Datta, S.; Sanyal, B.; Mookerjee, A., Magnetism in small bimetallic Mn-Co clusters. *Physical Review B* **2008,** *78* (1), 014402.
187.Smits, J. M.; Bour, J. J.; Vollenbroek, F. A.; Beurskens, P. T., Preparation and X-ray Structure Determination of [Pentakis {1, 3-bis (Diphenylphosphino) Propane}] Undecagoldtris (Thiocyanate),[Au11 {PPh2C3H6PPh2} 5](SCN) 3. *J. Cryst. Spectrosc.* **1983,** *13*, 355-363.
188.Häkkinen, H.; Walter, M.; Grönbeck, H., Divide and Protect: Capping Gold Nanoclusters with Molecular Gold-Thiolate Rings. *J. Phys. Chem. B* **2006,** *110*, 9927-9931.
189.Jo, C.; Lee, J. I., Spin Polarization and Charge Transfer of Co Nanoclusters Coated with CO Molecules. *J. Magn. Magn. Mater.* **2009,** *321* (2), 47-51.
190.Orpen, A. G.; Connelly, N. G., Structural Systematics: the Role of PA. Sigma.* Orbitals in Metal-Phosphorus. pi.-Bonding in Redox-Related Pairs of M-PA3 Complexes (A= R, Ar, OR; R= alkyl). *Organometallics* **1990,** *9*, 1206-1210.
191.Gambardella, P.; Rusponi, S.; Veronese, M.; Dhesi, S. S.; Grazioli, C.; Dallmeyer, A.; Cabria, I.; Zeller, R.; Dederichs, P. H.; Kern, K.; Carbone, C.; Brune, H., Giant Magnetic Anisotropy of Single Cobalt Atoms and Nanoparticles. *Science* **2003,** *300*, 1130-1133.
192.Marbella, L. E.; Andolina, C. M.; Smith, A. M.; Hartmann, M. J.; Dewar, A. C.; Johnston, K. A.; Daly, O. H.; Millstone, J. E., Gold- Cobalt Nanoparticle Alloys Exhibiting Tunable Compositions, Near- Infrared Emission, and High T2 Relaxivity. *Adv. Funct. Mater.* **2014,** *24*, 6532-6539.
193.Gao, J.; Gu, H.; Xu, B., Multifunctional Magnetic Nanoparticles: Design, Synthesis, and Biomedical Applications. *Accounts of Chemical Research* **2009,** *42* (8), 1097-1107.
194.Li, X.; Wei, J.; Aifantis, K. E.; Fan, Y.; Feng, Q.; Cui, F.-Z.; Watari, F., Current Investigations into Magnetic Nanoparticles for Biomedical Applications. *J. Biomed. Mater. Res. A* **2016,** *104* (5), 1285-1296.

195.Wu, L.; Mendoza-Garcia, A.; Li, Q.; Sun, S., Organic Phase Syntheses of Magnetic Nanoparticles and Their Applications. *Chem. Rev.* **2016,** *116* (18), 10473-10512.
196.Chappert, C.; Fert, A.; Van Dau, F. N., The Emergence of Spin Electronics in Data Storage. *Nat. Mater.* **2007,** *6*, 813-823.
197.Jae-Hyun, L.; Yong-Min, H.; Young-wook, J.; Seo, J.-w.; Jang, J.-t.; Ho-Taek, S.; Sungjun, K.; Eun-Jin, C.; Yoon, H.-G.; Suh, J.-S., Artificially Engineered Magnetic Nanoparticles for Ultra-Sensitive Molecular Imaging. *Nat. Med.* **2007,** *13* (1), 95.
198.Walter, M.; Akola, J.; Lopez-Acevedo, O.; Jadzinsky, P. D.; Calero, G.; Ackerson, C. J.; Whetten, R. L.; Grönbeck, H.; Häkkinen, H., A unified view of ligand-protected gold clusters as superatom complexes. *Proceedings of the National Academy of Sciences* **2008,** *105* (27), 9157-9162.
199.Billas, I. M.; Chatelain, A.; de Heer, W. A., Magnetism from the Atom to the Bulk in Iron, Cobalt, and Nickel Clusters. *Science* **1994,** *265*, 1682-1684.
200.Billas, I. M.; Châtelain, A.; de Heer, W. A., Magnetism of Fe, Co and Ni clusters in molecular beams. *Journal of magnetism and magnetic materials* **1997,** *168* (1-2), 64-84.
201.Zhan, L.; Chen, J. Z.; Liu, W.-K.; Lai, S., Asynchronous Multicanonical Basin Hopping Method and its Application to Cobalt Nanoclusters. *J. Chem. Phys.* **2005,** *122* (24), 244707.
202.Pople, J. A.; Gill, P. M.; Handy, N. C., Spin-Unrestricted Character of Kohn-Sham Orbitals for 0 pen-S he 11 Systems. **1995**.
203.Hoffmann, R., How Chemistry and Physics Meet in the Solid State. *Angew. Chem. Int. Edit.* **1987,** *26* (9), 846-878.
204.Frederick, M. T.; Weiss, E. A., Relaxation of Exciton Confinement in CdSe Quantum Dots by Modification with a Conjugated Dithiocarbamate Ligand. *ACS Nano* **2010,** *4* (6), 3195-3200.
205.Boles, M. A.; Ling, D.; Hyeon, T.; Talapin, D. V., The Surface Science of Nanocrystals. *Nat. Mater.* **2016,** *15* (2), 141.
206.McKenzie, L. C.; Zaikova, T. O.; Hutchison, J. E., Structurally Similar Triphenylphosphine-Stabilized Undecagolds, Au11(PPh3)7Cl3 and [Au11(PPh3)8Cl2]Cl, Exhibit Distinct Ligand Exchange Pathways with Glutathione. *J. Am. Chem. Soc.* **2014,** *136* (38), 13426-13435.
207.Erickson, J. D.; Mednikov, E. G.; Ivanov, S. A.; Dahl, L. F., Isolation and Structural Characterization of a Mackay 55-Metal-Atom Two-Shell Icosahedron of Pseudo-I h Symmetry, Pd55L12(μ3-CO)20 (L= PR3, R= Isopropyl): Comparative Analysis with Interior Two-Shell Icosahedral Geometries in Capped Three-Shell Pd145, Pt-Centered Four-Shell Pd–Pt M165, and Four-Shell Au133 Nanoclusters. *J. Am. Chem. Soc.* **2016,** *138* (5), 1502-1505.
208.Teo, B. K.; Yang, H.; Yan, J.; Zheng, N., Supercubes, Supersquares, and Superrods of Face-Centered Cubes (FCC): Atomic and Electronic Requirements of [Mm(SR)l(PR′3)8]q Nanoclusters (M = Coinage Metals) and Their Implications with Respect to Nucleation and Growth of FCC Metals. *Inorg. Chem.* **2017**.
209.Foresman, J. B.; Head-Gordon, M.; Pople, J. A.; Frisch, M. J., Toward a Systematic Molecular Orbital Theory for Excited States. *J. Phys. Chem.* **1992,** *96* (1), 135-149.
210.Morrison, A. F.; You, Z.-Q.; Herbert, J. M., Ab Initio Implementation of the Frenkel–Davydov Exciton model: A Naturally Parallelizable Approach to Computing Collective Excitations in Crystals and Aggregates. *J. Chem. Theory Comput.* **2014,** *10* (12), 5366-5376.
211.Jacobson, L. D.; Herbert, J. M., An Efficient, Fragment-Based Electronic Structure Method for Molecular Systems: Self-Consistent Polarization with Perturbative Two-Body Exchange and Dispersion. *J. Chem. Phys.* **2011,** *134* (9), 094118.

212.Dreuw, A.; Weisman, J. L.; Head-Gordon, M., Long-Range Charge-Transfer Excited States in Time-Dependent Density Functional Theory Require Non-Local Exchange. *J. Chem. Phys.* **2003,** *119* (6), 2943-2946.
213.Subotnik, J. E., Communication: Configuration Interaction Singles has a Large Systematic Bias Against Charge-Transfer States. AIP: 2011; Vol. 135, p 071104.
214.Jacquemin, D.; Perpète, E. A.; Assfeld, X.; Scalmani, G.; Frisch, M. J.; Adamo, C., The Geometries, Absorption and Fluorescence Wavelengths of Solvated Fluorescent Coumarins: A CIS and TD-DFT Comparative Study. *Chem. Phys. Lett.* **2007,** *438* (4-6), 208-212.
215.Stanton, J. F.; Gauss, J.; Ishikawa, N.; Head- Gordon, M., A Comparison of Single Reference Methods for Characterizing Stationary Points of Excited State Potential Energy Surfaces. *J. Chem. Phys.* **1995,** *103* (10), 4160-4174.
216.Hirata, S.; Head-Gordon, M.; Bartlett, R. J., Configuration Interaction Singles, Time-Dependent Hartree–Fock, and Time-Dependent Density Functional Theory for the Electronic Excited States of Extended Systems. *J. Chem. Phys.* **1999,** *111* (24), 10774-10786.
217.Dreuw, A.; Head-Gordon, M., Single-Reference ab initio Methods for the Calculation of Excited States of Large Molecules. *Chem. Rev.* **2005,** *105* (11), 4009-4037.
218.Shea, J. A.; Neuscamman, E., A Mean Field Platform for Excited State Quantum Chemistry. *arXiv preprint arXiv:1806.00853* **2018**.
219.Liu, X.; Fatehi, S.; Shao, Y.; Veldkamp, B. S.; Subotnik, J. E., Adjusting Charge Transfer State Energies for Configuration Interaction Singles: Without Any Parameterization and with Minimal Cost. AIP: 2012; Vol. 136, p 161101.
220.Rabuck, A. D.; Scuseria, G. E., Improving Self-Consistent Field Convergence by Varying Occupation Numbers. *J. Chem. Phys.* **1999,** *110* (2), 695-700.
221.Pela, R. R.; Werner, U.; Nabok, D.; Draxl, C., Probing the LDA-1/2 Method as a Starting Point for G_0W_0 Calculations. *Phys. Rev. B* **2016,** *94* (23), 235141.
222.Ferreira, L. G.; Marques, M.; Teles, L. K., Approximation to Density Functional Theory for the Calculation of Band Gaps of Semiconductors. *Phys. Rev. B* **2008,** *78* (12), 125116.
223.Chai, J.-D., Density Functional Theory with Fractional Orbital Occupations. *J. Chem. Phys.* **2012,** *136* (15), 154104.
224.Chai, J.-D., Thermally-Assisted-Occupation Density Functional Theory with Generalized-Gradient Approximations. *J. Chem. Phys.* **2014,** *140* (18), 18A521.
225.Slavíček, P.; Martínez, T. J., Ab Initio Floating Occupation Molecular Orbital-Complete Active Space Configuration Interaction: An Efficient Approximation to CASSCF. *J. Chem. Phys.* **2010,** *132* (23), 234102.
226.Shu, Y.; Hohenstein, E. G.; Levine, B. G., Configuration Interaction Singles Natural Orbitals: An Orbital Basis for an Efficient and Size Intensive Multireference Description of Electronic Excited States. *J. Chem. Phys.* **2015,** *142* (2), 024102.
227.Shao, Y.; Gan, Z.; Epifanovsky, E.; Gilbert, A. T.; Wormit, M.; Kussmann, J.; Lange, A. W.; Behn, A.; Deng, J.; Feng, X., Advances in Molecular Quantum Chemistry Contained in the Q-Chem 4 Program Package. *Mol. Phys.* **2015,** *113* (2), 184-215.
228.Dunning Jr, T. H., Gaussian Basis Sets for Use in Correlated Molecular Calculations. I. The Atoms Boron Through Neon and Hydrogen. *J. Chem. Phys.* **1989,** *90* (2), 1007-1023.
229.Dimitrova, Y.; Peyerimhoff, S. D., Theoretical Study of Hydrogen-Bonded Formaldehyde-Water Complexes. *J. Phys. Chem.* **1993,** *97* (49), 12731-12736.

230.Iwata, S.; Morokuma, K., Molecular Orbital Studies of Hydrogen Bonds. V. Analysis of the Hydrogen-Bond Energy Between Lower Excited States of Formaldehyde and Water. *J. Am. Chem. Soc.* **1973,** *95* (23), 7563-7575.
231.Del Bene, J. E., Molecular Orbital Theory of the Hydrogen Bond. XI. The Effect of Hydrogen Bonding on the n→ π* Transition in Dimers HOH· · · OCHR. *J. Chem. Phys.* **1975,** *62* (2), 666-669.